University of Alberta

Geometric Models to Model Acoustic Barriers Including Atmospheric
Conditions

by

Amirmohamed Muradali   ©

A thesis submitted to the Faculty of Graduate Studies and Research in partial
fulfillment of the requirements for the degree of Master of Science.

Department of Mechanical Engineering

Edmonton, Alberta
Fall 1997

Canada

To my mother and sister for their continued encouragement and support, and in loving memory of my father, Abbasali Muradali.

ABSTRACT

Wave based solutions of noise barrier geometries accurately model the complex direct, reflected and diffracted sound field interactions. However, these solutions are very computer intensive and thus are not practical as a design tool. Improved diffraction based methods, that include phase, now yield wave-like accuracy with trivial calculation times. Extensions of these methods are made to consider two dimensional geometries, parallel barrier geometries, the effect of finite ground impedance and the consideration of three-dimensional coherent and incoherent line sources. Good agreements were observed with both finite element and boundary element models. These results, however accurate, typically over-predict the actual performance of noise barriers, because atmospheric effects such as wind, temperature gradients and turbulence have not been considered.

To overcome this limitation, a new acoustic modeling tool is proposed that combines an improved diffraction-based sound barrier performance model with a heuristic atmospheric model. Comparisons with the Parabolic Equation (PE), a wave based technique, show good agreements and preliminary applications of this model yield the expected sound barrier performance degradation due to the acoustic medium non-homogeneity.

Acknowledgements

First and foremost I would like to thank my supervisor, Dr. Ken Fyfe, for his support and guidance throughout the preparation of this thesis. I am especially grateful to him for maintaining a casual and friendly atmosphere which made research work both an enjoyable, as well as an educational experience.

I would also like to thank Dr. Gilles Daigle at the National Research Council for Canada in Ottawa for valuable discussions that aided in the research and writing of this thesis. My sincere thanks to him and his research team for their hospitality during my stay in Ottawa.

I am grateful for financial support of the Natural Sciences and Engineering Research Council of Canada and the Government of the Province of Alberta whilst preparing this thesis.

My sincere thanks go out to James B., Dallas C., Ian F. and Mike M. for their help and friendship throughout my time here as a graduate student. To my good friend Arief, thanks for helping me take myself less seriously.

Above all, I am indebted to my mother, Noorjehan, and my sister, Farah, whose support and encouragement has made the completion of this thesis possible.

CONTENTS

LIST OF FIGURES

LIST OF TABLES

Chapter 1

Introduction

Traffic noise is a major concern to the general public, especially to those who live in close proximity to major highways or thoroughfares. To attenuate the noise generated by large traffic volumes, roadside barriers and berms are constructed. However, these noise attenuation structures cost in the order of one million dollars per kilometer [1.1]. In designing and implementing these barriers, it is therefore critical to understand the parameters which dominate their effectiveness.

This chapter presents a brief discussion on the road noise problem, different barrier types and current techniques that are used to predict barrier performances. Limitations of the current methods are discussed and motivation is given to extend a promising method for road noise modeling.

It has often been noted though that the actual performance of barriers is usually overpredicted by such techniques. This is because a homogeneous atmosphere is assumed in their formulations, thus ignoring atmospheric effects. Several initiatives have been undertaken to study the effects of atmospheric inhomogeneities on sound propagation, and as a result, various models have been developed for modeling outdoor sound propagation. However, a major limitation with these models is that they require excessive computational times. This motivated the development of a heuristic atmospheric model, based on geometrical ray theory, to model outdoor sound propagation with small computational times. A discussion on the limitations of this model

1

and its promising aspects are presented.

To model atmospheric effects on barrier performance, a novel combined approach is outlined. In this approach, current diffraction based techniques for modeling barriers is combined with the heuristic atmospheric model.

1.1 Background

1.1.1 The Road Noise Problem

The study of road noise problem and its attenuation is a multi-faceted problem. The subject can be broken down into three areas: (i) noise generation, (ii) propagation or transmission, and (iii) perception.

- Noise generation depends highly on the type of vehicle, speed of vehicle and the traffic volume. The primary sources of noise are the engine, for low-speed traffic, and the tire-road contact, for high speed traffic. This area has been studied experimentally and several empirical relationships have been derived which are used to model the source [1.2] and its frequency content [1.3].

- The propagation or transmission of the generated noise is affected by many factors including: geometric spreading, ground impedance or absorption and atmospheric effects which include wind, temperature gradients, turbulence and atmospheric absorption. The other major influencing factor in noise propagation is that due to the scattering and diffraction of the sound waves over objects and noise control measures such as barriers and berms.

- The perception of the received noise is the final factor in determining its annoyance. This is primarily a psycho-acoustic problem and factors that are considered include the noise levels, their frequency content and the time of day that they occur.

2

This thesis focuses on the second area, namely the propagation of sound. In particular, the focus will be on noise barrier analysis and the effects of atmosphere on noise barriers.

1.1.2 Noise Barriers

Noise barriers are used to shield the direct *line-of-sight* between the noise source and the listener as shown in Figure 1.1. Several configurations of noise barriers have been implemented, some of which are shown in Figure 1.2. These include:

- single barriers - thin walls placed on one side of a highway that is next to a residential area.

- parallel barriers - thin walls placed on either side of a highway passing through a residential area.

- variable geometry barriers - examples are T-shaped barriers and angled barriers.

- absorptive barriers - barriers with sound absorbing panels (on the traffic side) absorb the sound energy from the incident wave.

- depressed roadways - may be used in combinations with conventional barriers.

- earth berms - mounds of earth covered usually with grass and sometimes has a conventional barrier at the top.

- vegetative barriers - barriers that are in part, or totally, made up of natural vegetation such as trees and bushes.

The bulk of barrier modeling techniques assume rigid thin walls for single/parallel barrier geometries. As such, this thesis will focus on barriers modelled as rigid thin walls.

3

1.2 Techniques for Analysing Noise Barriers

1.2.1 Diffraction Based Methods

Traditional methods for analysing noise barriers are based on geometrical ray theory which treats sound as a series of rays emitted from a source. These rays are reflected off the ground and diffracted off the top and sides of the barrier, as they make their way from the source to the receiver. This is depicted in Figure 1.3.

Current literature contains a wide variety of these methods [1.4, 1.5, 1.6, 1.7, 1.8, 1.9]. These methods are diffraction based, which extend the optical geometric theory of diffraction to that of acoustic waves. One of the simplest and most widely used in the engineering community, is that of Maekawa [1.4]. He introduced an empirically based diffraction model that provides the insertion loss due to a thin-walled barrier in terms of the Fresnel number. Maekawa then suggested that the insertion loss for a finite-length barrier could be determined by multiple application of this curve to the diffraction paths around the barrier and then summing the energy contributions of these paths. By doing this, the phase information between the diffraction paths was lost, and thus lead to poor approximations of the sound field behind the barrier.

1.2.2 Wave Based Methods

More exact approaches for estimating barrier insertion loss are performed with wave based methods such as the Boundary Element Method (BEM), and the Finite Element Method and in particular the Infinite Wave Envelope Method (IFEM). These methods solve the governing Helmholtz wave equation and exactly model the reflection, diffraction and the phase interferences in the sound field around the barrier.

1.2.2.1 Boundary Element Methods (BEM)

The boundary element method in acoustics is formulated by applying Green's theorem to the Helmholtz integral equation. This has the effect of converting a three

4

dimensional volume integral of the acoustic domain to a two dimensional surface integral. This means that only a description of the radiating or scattering body is required rather than a complete, and often inadequate, description of the surrounding domain. The boundary element method is well suited for infinite domains, and thus for exterior problems as the radiation condition is inherently satisfied through the Green function kernels.

When applying this method, the surface of the body is subdivided, or discretized, into nodes and elements. The Helmholtz integral equation, which relates the acoustic pressure and velocity on the body, is applied to each node. This has the effect of linking it to all other elements (and nodes) on the body. This technique thus generates a fully populated, complex, non-symmetric matrix for each analysis frequency.

For two dimensional and axisymmetric geometries, boundary element methods yield excellent results in very reasonable calculation times. However, when considering a real-life geometry of a finite length barrier (i.e. an exterior three-dimensional problem with large geometry (barrier lengths greater than 500 m) and analysis frequencies up to 2000 Hz), BEM methods quickly become impractical to run. Typical barrier geometries at road noise frequencies prove to be computationally intensive and take in the order of hours, and for some cases days, to solve for one frequency on an engineering workstation. Another limitation of the boundary element method, is that the Green function kernels, which are basically the solution of a point source in the acoustic medium, assume a homogeneous propagation medium.

1.2.2.2   Finite Element Methods (FEM) using Infinite Wave Envelope Elements (IFEM)

Acoustic finite element solutions typically make use of a variational or Galerkin residual formulation for solving the Helmholtz equation. An enclosed volume (for three dimensional problems) is divided into a series of smaller subregions or finite elements connected at discrete nodes. The variation of the acoustic variables within an element is described by shape functions (usually simple polynomials). Governing equations

5

are written for each element and these are assembled into a global matrix. Boundary conditions are applied and the unknowns are determined.

Due to the formulation of this method, the resulting matrices are banded because each node is only related to its surrounding neighbors. This is in contrast to the boundary element method where each node is related to all other nodes. Of course the penalty with the finite element method is that a much larger number of nodes are required because of the volume discretization. Another problem is that for modeling unbounded domains a large, but finite size of mesh is required to approximate this infinite domain. The trick is to come up with appropriate boundary conditions to simulate this case.

One method to deal with unbounded domains using finite element methodology is with the use of infinite elements, and in particular, infinite wave envelope methods [1.12, 1.13]. Recent work has shown that is it possible to very efficiently model both radiation and scattering phenomena with these elements. When applying these elements to a body, it is often necessary to surround the body with several layers of conventional elements to permit the near field to be accounted for, while the far field is modeled with the infinite elements. With the use of higher order infinite elements, it is possible to reduce and even eliminate this conventional element layer [1.13].

This type of modeling is very attractive because it has many of the advantages of the finite element methodology (banded matrices and quick frequency sweeps), while still being able to accurately model unbounded problems. The major limitation of this method is that only low frequency/small size geometries can be studied. Once the problem approaches $ka = 20$ (where k is the wave number $(2\pi/\lambda)$, and a is a typical body dimension), the results begin to deteriorate [1.13]. This limits the use of this method for many practical geometries.

6

1.2.2.3 Infinite Boundary Element Methods (IBEM)

To overcome the above mentioned limitations of the boundary element method (namely the large matrix size and slow solution times) and the infinite finite element method (limited to low frequency solutions), hybrid infinite boundary element schemes have been devised [1.14, 1.15]. This approach makes use of boundary element methodology but, relies on sub-domaining to divide the infinite radiation region into small sub-regions. This has the effect of adding bandedness to the boundary element method, which is good to keep memory storage problems to a minimum. Accurate modeling is thus insured with good implementation characteristics.

The sub-domaining of the acoustic fluid is not without its difficulties however. The effect of sub-domaining with the boundary element method is to localize the application of the radiation condition. This affects the radiation of higher order multipoles which are fundamental to more complicated radiation and scattering problems [1.15]. In addition, testing has shown that it is necessary to include acoustic windows to permit proper modeling of the acoustic near field [1.15].

1.2.3 Improved Diffraction Based Methods

The multitude of problems associated with BEM, FEM/IFEM and IBEM methods are further underlined when considering typical barrier geometries at typical road noise frequencies. This motivated the search for a quicker, more practical means for modeling the acoustic performance of roadside barriers.

Recently, Lam [1.9] improved on Maekawa's method by summing complex pressures, instead of energies, of each diffraction path around the barrier. This was done to incorporate the phase interaction and interference between the paths, the absence of which, Lam suggested, was the cause of poor agreement between Maekawa's method and experimental results. By incorporating phase interaction, excellent agreement was observed with experimental and wave-based BEM results.

This model was seen as an important contribution in modeling noise barriers as

7

it was then possible to obtain results with wave-based accuracy in diffraction based calculation times. As such, Lam's method was implemented and extended to model real-life barrier geometries, such as single and parallel barrier geometries, and also take the effects of ground impedance into account.

1.3   Atmospheric Effects

Barrier insertion losses predicted by current methods have often been noted to be different from the actual performance of barriers. This is thought to be because the atmosphere is assumed to be perfectly homogeneous in these methods. In actuality, the atmosphere consists of several inhomogeneities such as wind and temperature gradients, and turbulence. These inhomogeneities greatly affect the way in which sound energy is transmitted.

The variation of wind and air temperature with height, and the presence of turbulence, results in an effective sound speed that varies not only with location, but also with time. As sound waves travel in a medium with a sound speed that varies with height, parts of the wave front travel at different speeds. As a result, the sound rays, which are normals to wave fronts, are curved as shown in Figure 1.4.

During typical daytime or upwind conditions, the speed of sound decreases with height. This is known as an *upward refracting* atmosphere because sound rays curve upwards as depicted in Figure 1.5. This condition results in a *shadow region* some distance away from the source where the sound pressures are minimal.

Also shown in Figure 1.5 are sound rays in typical nighttime or downwind conditions. During these conditions, the sound speed increases with height, and the atmosphere is referred to as *downward refracting*. It is during these conditions that the effectiveness of noise barriers is degraded. This is because the direct ray, which was previously along the *line-of-sight* and was shielded by the barrier in homogeneous conditions, now curves over top the barriers, as shown in Figure 1.6, thereby increasing the sound pressures within the shielded, or shadow regions.

1.4 Sound Propagation in the Presence of Atmospheric Effects

1.4.1 Wave Solutions

The area of outdoor sound propagation has been reviewed by many researchers in the past [1.16, 1.17, 1.18, 1.19]. Some state-of-the-art prediction schemes have been developed to model long range sound propagation in a medium with an arbitrary sound speed profile. These techniques include the Fast Field Program (FFP) [1.20, 1.21] and the Parabolic Equation (PE) [1.22, 1.23] techniques. A summary of these and other computational techniques can be found in a review by Attenborough *et al.* [1.24].

Although these techniques can account for various types of sound speed profiles and atmospheric turbulence [1.25, 1.26], they are generally restricted to flat ground propagation and can only model axisymmetric geometries. Moreover, these models require excessive computational times.

1.4.2 Heuristic Atmospheric Model

To counter the problems of excessive computational times associated with the wave methods, L'Espérance *et al.* recently developed a model based on geometrical ray theory to predict outdoor sound propagation [1.28]. This heuristic model assumes a linearly varying sound speed profile for the atmosphere which permits a closed-form solution of all the rays, and the associated parameters.

The cases for upward and downward refracting profiles are handled separately in this model. For upward refracting profiles, the sound pressures within the shadow region are determined using a diffraction theory based on residual series solution. For downward refracting profiles, the roots of a fourth order polynomial aids in determining the multitude of rays, each having multiple ground reflections, that can appear between a source and receiver above ground [1.29].

This model provides a good first approximation for predicting outdoor sound

propagation in light of the complexities associated with the FFP and the PE. However, it was developed for flat ground propagation and cannot readily predict effects of a scattering body such as a barrier.

1.5 Investigations into Atmospheric Effects on Barrier Performance

Experimental studies have been conducted to study the effects of wind on the acoustic performance of barriers [1.30, 1.31]. Both studies concluded that wind does affect the barrier performance and that it is during downwind conditions that barrier performance is degraded. In a separate study, Daigle investigated the effects of turbulence over the top of barriers [1.32]. The overall effect was to scatter some of the sound energy down to the shadow regions close to the barriers thereby reducing the shielding effect of the barrier in these regions. Comparisons with experimental results showed that this was the case especially at higher frequencies.

Salomons recently developed a model, based on geometrical ray theory, to include atmospheric refraction in barrier performance calculations [1.33]. Comparisons were made with a PE technique incorporating a thin screen [1.27], and good agreements, in general, were observed. This work only included downwind conditions and was considered for long range sound propagation. It excludes the rays that undergo multiple reflections off the ground under the notion that these rays are absorbed in the presence of an absorbing ground. The only rays considered are the rays that travel from the source to the barrier top and from the barrier top to the receiver. In the presence of absorbing ground, the effects of the curved rays due to the refractive profile are considered in barrier insertion loss calculations, however, in the presence of a perfectly reflecting ground, these rays are assumed to be straight. Another weakness in this formulation is that, in the presence of a downward refracting atmosphere and at large distances away from the barrier, it is possible to have some sound rays passing over the barrier unattenuated [1.34], the effects of which were not discussed by Salomons.

10

This motivated the developement of a ray based model which, not only takes into account the multiple rays that can appear between a source, shielded by a barrier, and a receiver, but also accounts for the rays that can pass over the barrier. In this manner, a more accurate representation of the effects of atmosphere on noise barriers can be provided.

1.6   Thesis Outline

The first part of this thesis studies the current techniques for predicting barrier insertion loss. These techniques assume a homogeneous atmosphere, and as a result, the acoustic performance of barriers is usually overpredicted. The later part of this thesis investigates the effects of atmosphere on barrier performances, and a model is proposed that includes this *missing link* in an effort to accurately predict barrier insertion losses.

In particular, Chapter 2 focuses on extensions of Lam's principles to a wider range of source and barrier geometries, and comparisons were made to the wave-based BEM and FEM. The preliminary work of Lam was extended to include the modeling of two dimensional geometries, the comparison of two and three dimensional modeling, the consideration of parallel barriers, modeling the effect of finite ground impedance and the consideration of three-dimensional coherent and incoherent line sources. The work was also extended to include the diffraction models of Kurze and Anderson [1.5], and Pierce [1.10].

In Chapter 3, the heuristic atmospheric model is combined with Pierce's diffraction equations for a thin screen [1.10] to provide a more accurate means of barrier insertion loss predictions with the benefit of the trivial calculation times associated with geometrical and diffraction based techniques. The model, referred to as the *combined model*, includes the contributions of the many possible rays with multiple reflections on the ground and also the possible rays that pass over the barrier unattenuated. Also included are the effects of ground, atmospheric absorption and turbulence. In this

work, only the case for the positive sound speed gradients (downwind or nighttime conditions) are considered. The results from the combined model are compared to the PE formulation incorporating a thin screen [1.27].

Finally, a summary and the major conclusions of this thesis are outlined in Chapter 4. Also provided are some recommendations for future research work.

Chapters 2 and 3 are written as separate stand-alone papers. Chapter 2 has been accepted for publication in Applied Acoustics, while Chapter 3 has been submitted for review. At the end of the thesis, more detail is presented on certain topics. Appendix A summarises the principles behind geometrical theory of diffraction. Appendix B describes the modeling of atmospheric absorption. Appendix C outlines the formulation for the spherical reflection coefficient used for modeling the effects of ground impedance. Appendix D provides brief descriptions on the Fast Field Program (FFP) and the Parabolic Equation (PE).
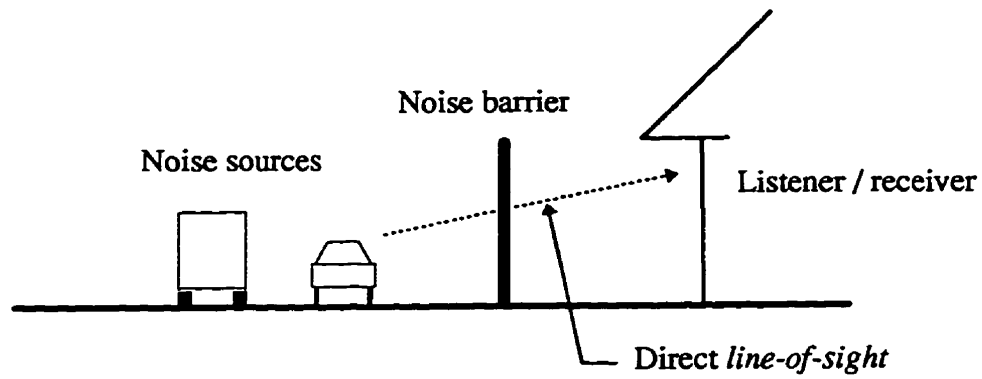
Figure 1.1: The direct *line-of-sight* between noise sources and receiver is shielded by the barrier.

Single barrier

Parallel barriers

Variable geometry barriers - e.g. T-shaped and angled barriers.

Absorptive panels

Absorptive barriers

Conventional barrier

Depressed roadways

Earth berms

Vegetative barriers
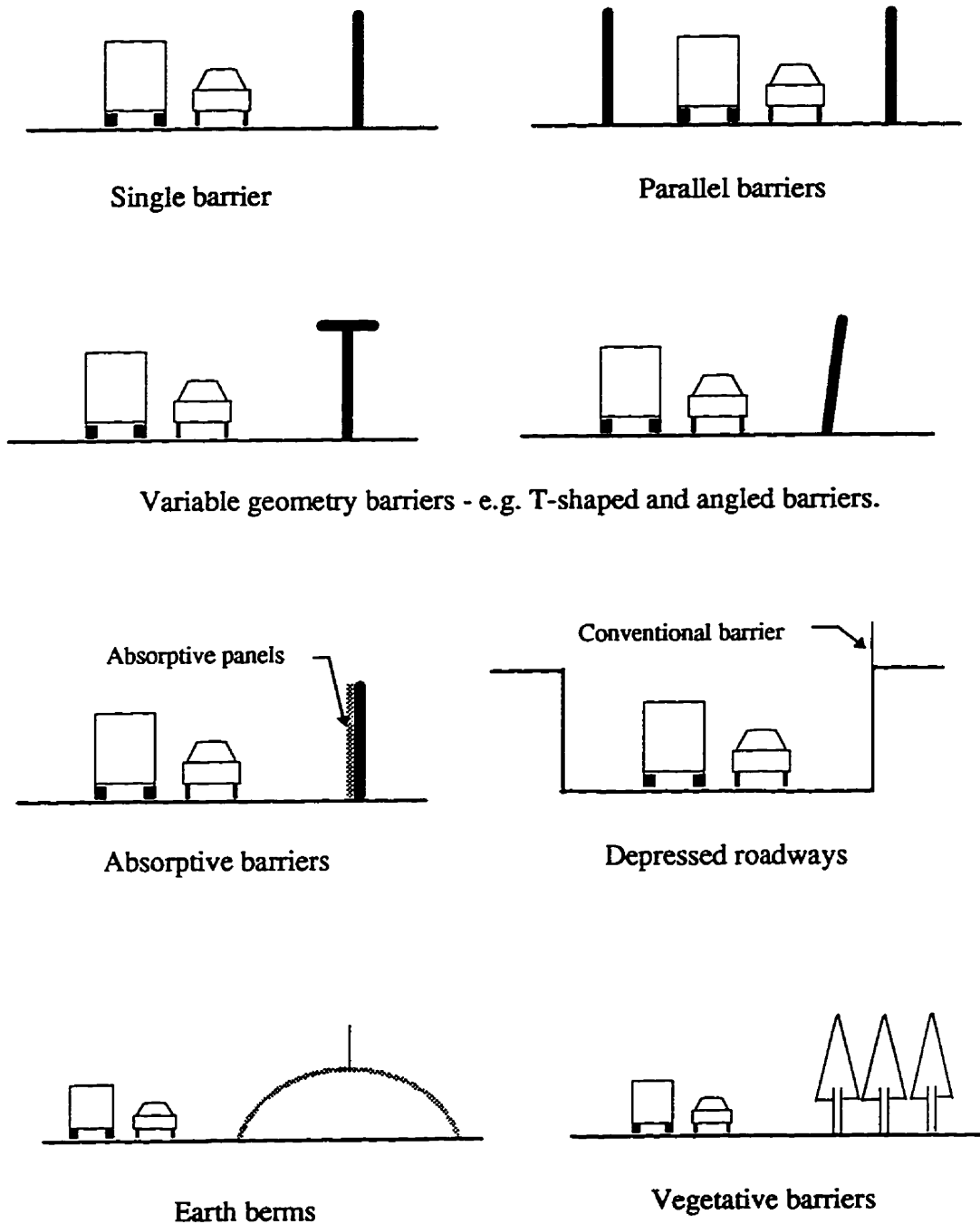
Figure 1.2: Various noise barrier configurations.

14
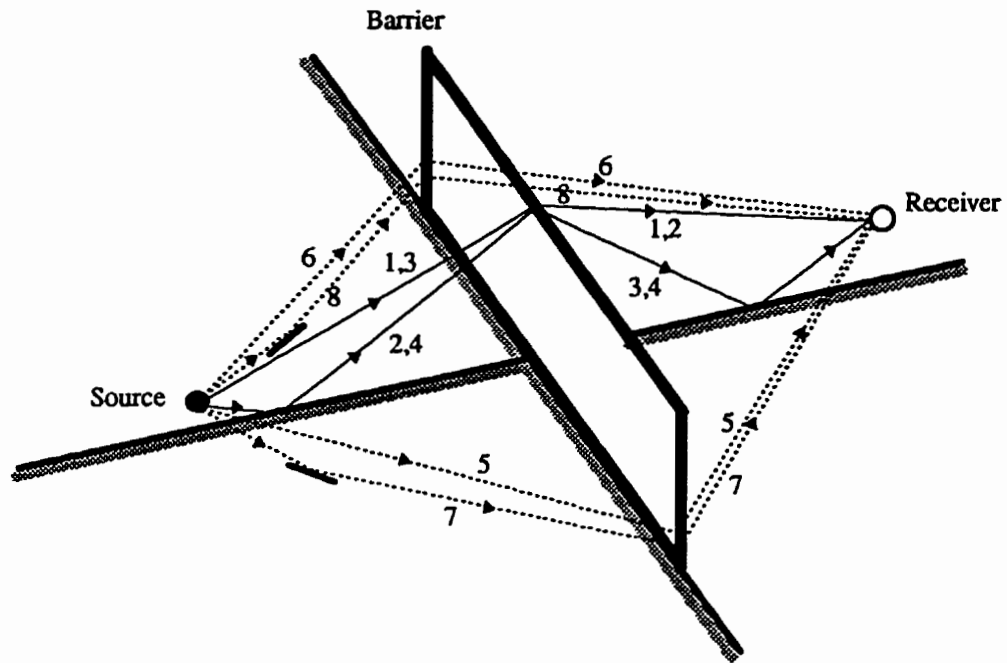
Figure 1.3: Sound rays emitted from source reflect and diffract on the way to receiver.
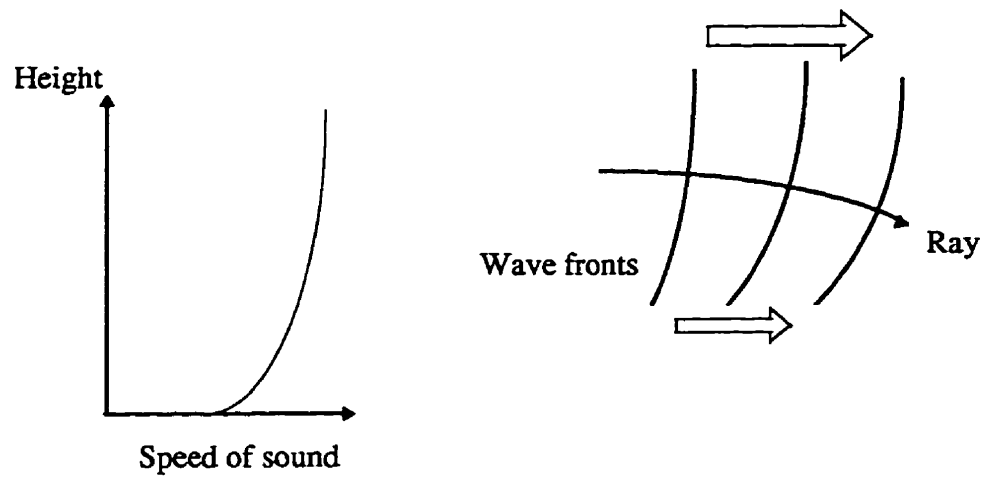
Figure 1.4: Sound rays are curved as parts of wave fronts move at different speeds.
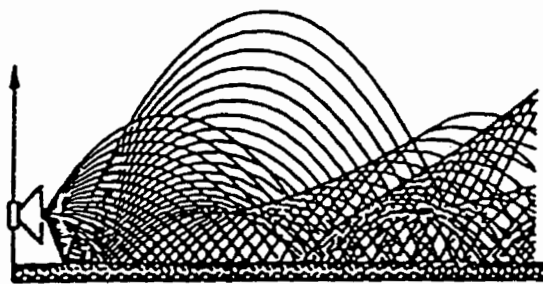
Downwind
or Nighttime
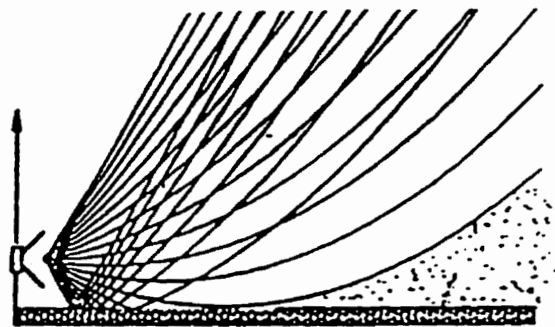
Upwind
or Daytime

Figure 1.5: Sound rays present in typical atmospheric conditions [1.34].
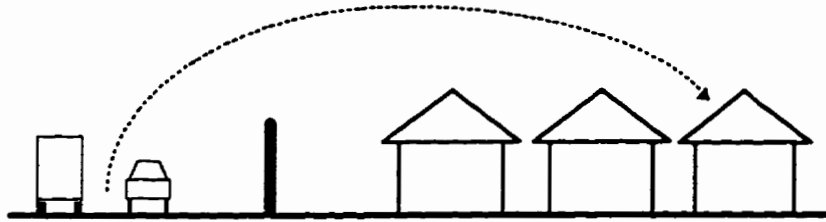
Figure 1.6: The direct ray curves over the top of the barrier due to atmospheric refraction.

References

1.1 U.S. Department of Transportation, Federal Highway Administration, Highway traffic noise barrier construction trends, *The Wall Journal*, **14** (1994) 8-16.

1.2 Northwood, T. D., Quirt, J. D. and Halliwell, R. E., Residential planning with respect to road and rail noise, *Noise Control Engineering*, **13** (1979) 63-75.

1.3 Lewis, P. T., The noise generated by single vehicles in freely flowing traffic, *J. Sound and Vibration*, **30** (1973) 207-220.

1.4 Maekawa, Z., Noise reduction by screens, *Applied Acoustics.*, 1 (1968) 157-173.

1.5 Kurze, U. J. & Anderson, G. S., Sound attenuation by barriers, *Applied Acoustics*, **4** (1971) 35-53.

1.6 L'Esperance, A., The insertion loss of finite length barriers on the ground. *J. Acoust. Soc. Am.*, **86** (1989) 179-183.

1.7 Kawai, Y. & Terai, T., The application of integral equation methods to the calculation of sound attenuation by barriers. *Applied Acoustics*, **31** (1990) 101-117.

1.8 Pirinchieva. R., Model study of the sound propagation behind barriers of finite length, *J. Acoust. Soc. Am.*, **87** (1990) 2109-2013.

1.9 Lam, Y. W., Using Maekawa's chart to calculate finite length barrier insertion loss, *Applied Acoustics*, **42** (1994) 29-40.

1.10 Pierce, A. D., Diffraction of sound around corners and over wide barriers. *J. Acoust. Soc. Am.*, **55** (1974) 941-955.

1.11 Hayek, S., Mathematical modeling of absorbent highway noise barriers. *Applied Acoustics*, **31** (1990) 77-100.

1.12 Astley, R. J., Wave envelope and infinite element elements for acoustical radiation, *Int. J. Numerical Methods Fluids.*, **3** (1983) 507-526.

1.13 Cremers, L. & Fyfe, K.R., On the use of variable order infinite wave envelope elements for acoustic radiation and scattering, *J. Acoust. Soc. Am.*, **97** (4) (1995) 2028-2040.

1.14 Zeng, X., Kallivokas, L. F., & Bielak, J., Stable localized symmetric integral equation method for acoustic scattering problems, *J. Acoust. Soc. Am.*, **91** (1992) 2510-2518.

1.15 Cremers, L. & Fyfe, K.R., A variable order infinite element for multi-domain boundary element modelling of acoustic radiation and scattering, Submitted for publication in *J. Sound and Vibration.*

1.16 Piercy, J. E., Embleton, T. F. W. & Sutherland, L. C., Review of nois propagation in the atmosphere, *J. Acoust. Soc. Am.*, **61**(6) (1977) 1403-1418.

1.17 Delany, M. E., Sound propagation in the atmosphere: A historical review, *Acustica*, **38** (1977) 201-223.

1.18 Embleton, T. F. W., Sound propagation outdoors-Improved prediction schemes for the 80's, *Noise Control Engng*, **18**(1) (1982) 30-39.

1.19 Hallberg, B., Larsson, C. & Israelsson, S., Some aspects on sound propagation outdoors, *Acustica*, **66** (1988) 109-112.

1.20 Lee, S. W., Bong, N., Richards, W. F. & Raspet, R., Impedance formulation of the fast-field program for acoustic wave propagation in the atmosphere, *J. Acoust. Soc. Am.*, **79** (1986) 628-634.

1.21 Raspet, R., Lee, S. W., Kuester, E., Chang, D. C., Richards, W. F., Gilbert, R., and Bong, N., A fast-field program for sound propagation in a layered atmosphere above an impedance ground, *J. Acoust. Soc. Am.*, **77** (1985) 345-352.

1.22 White, M. J. & Gilbert, K. E., Application of the parabolic equation to the outdoor propagation of sound, *Applied Acoustics*, **27** (1989) 227-238.

1.23 Gilbert, K. E. & Di, X., A fast Green's function method for one-way sound propagation in the atmosphere, *J. Acoust. Soc. Am.*, **94** (1993) 2343-2352.

1.24 Attenborough, K. et al., Benchmark cases for outdoor sound propagation models, *J. Acoust. Soc. Am.*, **97** (1995) 173-191.

1.25 Gilbert, K. E., Raspet, R., and Di, X., Calculation of turbulence effects in an upward-refracting atmosphere, *J. Acoust. Soc. Am.*, **87** (1990) 2428-2437.

1.26 L'Esperance, A., Gabillet, Y. & Daigle, G. A., Outdoor sound propagation in the presence of atmospheric turbulence: Experiments and theoretical analysis with the fast field program algorithm, *J. Acoust. Soc. Am.*, **98** (1995) 570-579.

1.27 Salomons, Erik M., Diffraction by a screen in down wind sound propagation: A parabolic-equation approach, *J. Acoust. Soc. Am.* **95** (1994) 3109-3117.

1.28 L'Espérance, A., Herzog, P., Daigle, G. A. & Nicolas, J. R., Heuristic model for outdoor sound propagation based on an extension of the geometrical ray theory in the case of a linear sound speed profile, *Applied Acoustics*, **37** (1992) 111-139.

1.29 Embleton, T. F. W., Thiessen, G. J., & Piercy, J. E., Propagation in an inversion and reflections at the ground, *J. Acoust. Soc. Am.*, **59** (1976) 278-282.

1.30 Scholes, W. E., Salvidge, A. C. & Sargent, J. W., Field performance of a noise barrier, *J. Sound and Vibration*, **16** (1971) 627-642.

1.31 DeJong, R. & Stusnick, E., Scale model studies of the effects of wind on acoustic barrier performance, *Noise Control Engng*, May-June (1976) 101-109.

1.32 Daigle, G. A., Diffraction of sound by a noise barrier in the presence of atmospheric turbulence, *J. Acoust. Soc. Am.*, **71** (1982) 847-854.

1.33 Salomons, Erik M., Noise barriers in a refracting atmosphere, *Applied Acoustics*, **47** (1996) 217-238.

1.34 Daigle, G. A., Acoustics of noise control outdoors, *15th International Congress on Acoustics, Trondheim, Norway*, 26-30 June 1995, 49-56.

1.35 Keller, J. B., Geometrical theory of diffraction, *J. Opt. Soc. Am.*, **52** (1962) 116-130.

1.36 Born, M. and Wolf, E., *Principles of Optics*, 4th ed., Pergamon, Oxford, 1970, pp. 370-381.

Chapter 2

A Study of 2D and 3D Barrier Insertion Loss using Improved Diffraction Based Methods[1]

2.1 Introduction

Current literature contains a wide variety of methods for evaluating the attenuation due to a barrier of finite length [2.1, 2.2, 2.3, 2.4, 2.5, 2.6]. These methods are all diffraction based, which extend the optical geometric theory of diffraction to that of acoustic waves. One of the simplest and most widely used in the engineering community, is that of Maekawa [2.1]. He introduced an empirically based diffraction model that provides the insertion loss due to a thin-walled barrier in terms of the Fresnel number. Maekawa then suggested that the insertion loss for a finite-length barrier could be determined by multiple application of this curve to the diffraction paths around the barrier and then summing the energy contributions of these paths.

There exist more sophisticated mathematical models for determining barrier diffraction coefficients. One model is Pierce's work for diffraction due to a semi-infinite wedge of arbitrary angle with ideal (rigid) boundary conditions [2.7]. This model can determine the diffraction field for both 2D and 3D geometries, and involves the evaluation of Airy functions and Fresnel integral functions. Another model is that of Kurze and Anderson's for sound attenuation by semi-infinite barriers [2.2]. This

---

[1]A version of this chapter has been accepted for publication in *Applied Acoustics*.

model also addresses both 2D and 3D geometries. In a paper by Hayek [2.8], other diffraction models are discussed. These include the diffraction due to a half plane and a wedge, with either ideal boundary conditions or impedance boundary conditions on either face of the plane/wedge.

The more exact approach to estimating the insertion loss of a barrier is with wave-based methods such as the Boundary Element Method (BEM) [2.9, 2.10] and Finite Element Methods (FEM) [2.11]. These methods solve the wave equation and thus model the phase interaction and the diffraction field around the barrier. Since the problem of the barrier is an exterior three-dimensional (3D) problem with large geometry, the BEM/FEM methods necessitate unreasonable calculation times. Typical barrier geometries at road noise frequencies prove to be computational intensive and take in the order of hours, and for some cases days, to solve for one frequency on a workstation. This makes it impossible to conduct typical barrier design tests such as frequency sweeps to high frequencies, broad band tests, and parametric studies on barrier geometries with the BEM/FEM methods.

More recently, Lam [2.6] improved on Maekawa's method by summing complex pressures, instead of energies, of each diffraction path around the barrier. This was done to incorporate the phase interaction and interference between the paths, the absence of which, Lam suggested, was the cause of the poor agreement between Maekawa's method and experimental results. By incorporating this phase interaction, excellent agreement was observed with experimental and wave-based BEM results. With this method then, it was possible to obtain wave-based accuracy with diffraction-based calculation time.

Due to the initial success of Lam, it was decided to extend the principles of Lam to a wider range of source and barrier geometries and compare the results to the wave-based BEM and FEM. The work described in this paper implements and compares the diffraction models of Maekawa, Kurze and Anderson and Pierce. This work also considers and compares both 2D and 3D geometrical modelling, single and parallel

barrier configurations, finite impedance plane considerations and a study of coherent and incoherent line sources.

2.2 Theory

2.2.1 Background

For diffraction based models, the pressure at the receiver is determined by summing the contribution from each diffracted path as it propagates from the source. Figures 2.1 and 2.2 illustrate the different diffraction paths around a barrier present in both two dimensional and three dimensional cases. The pressure due to the diffracted path i is

$$p_i = A_i e^{j\zeta_i} G(kd_i) \tag{2.1}$$

where A_i, ζ_i and d_i are the amplitude change at diffraction, phase shift at diffraction and the path length of the diffracted wave, respectively. The function, G, is the geometric spreading for the source being considered. The total pressure at the receiver is the sum of the individual paths,

$$p_r = \sum_{i=1}^{n} p_i = \sum_{i=1}^{n} A_i e^{j\zeta_i} G(kd_i) \tag{2.2}$$

where n is the total number of paths being considered.

For 2D geometries, $n = 4$ and $G = H_0^{(1)}(kd_i)$, which is a Hankel function of the first kind of order zero (Figure 2.1). It is used to determine the scattering due to a cylindrical source. For the 3D case, $n = 8$ and $G = e^{-jkd_i}/d_i$ (Figure 2.2). Note that there are ten possible paths for the 3D geometry, however only eight of which are applicable for any source-receiver configuration. When the receiver is closer to the ground, paths 7 and 8 are replaced with paths 9 and 10 which consider ground reflections on the receiver side.

In this Chapter, Lam's principles incorporating various diffraction models will be compared. For 2D geometries the diffraction models considered are Kurze and

25

Anderson's equation, and Pierce's equations, while for 3D geometries the diffraction models considered are Maekawa's curve, Kurze and Anderson's equation, and Pierce's equations.

2.2.2 Lam's method using Maekawa's curve

In Lam's paper, the equation for the finite barrier insertion loss is given by

$$IL(dB) = M_1 + 10\log \frac{1 + 2\frac{d_a}{d_r}\cos(\pi N_r) + \left(\frac{d_a}{d_r}\right)^2}{\sum_{i=1}^{8}\sum_{m=1}^{8}\frac{10^{-M_i/20}}{10^{-M_1/20}}\frac{10^{-M_m/20}}{10^{-M_1/20}}\cos\left[\pi\left(N_i - N_m\right)\right]} \tag{2.3}$$

where N_i is the Fresnel number for the ith path, and M is the insertion loss value from Maekawa's curve. The subscript o refers to the direct path (from the source to receiver) and the subscript r refers to the ground reflected path (from the source image to receiver). Maekawa's curve can be represented by the following two equations

$$M = 20\log\frac{2\pi\sqrt{\frac{N}{2}}}{\tanh(\pi\sqrt{\frac{N}{2}})} \qquad (N < 1)$$

$$\tag{2.4}$$

$$M = 10\log(20N) \qquad (N \geq 1)$$

The Fresnel number is given by

$$N = \frac{2}{\lambda}(A + B - d)$$

where $(A + B - d)$ is the path length difference as shown in Figure 2.3, and λ is the wavelength.

Lam's equation for finite barrier insertion loss can be broken down to determine the pressure due to each of the diffracted path in the form of Equation 2.1

$$p_i = A_i e^{j\frac{\pi}{4}}\frac{e^{-jkd_i}}{d_i} \tag{2.5}$$

where A_i is an amplitude term and can be determined by

$$A = \frac{d_i}{d_o}\left(\frac{\tanh(\pi\sqrt{\frac{N}{2}})}{2\pi\sqrt{\frac{N}{2}}}\right) \qquad (N < 1)$$

$$\tag{2.6}$$

$$A = \frac{d_i}{d_o}\left(\frac{1}{\sqrt{20N}}\right) \qquad (N \geq 1)$$

26

using Maekawa's diffraction equations. In this equation, d_o is the direct path length from the source (image) to receiver (image) depending on what path is being considered.

Note that Lam's method incorporating Maekawa's curve only accounts for the amplitude change at the diffraction edge (A_i in Equation 2.5). The phase shift ($\pi/4$) is included in Equation 2.5 based on Lam's suggestion that the phase shift at diffraction (for 3D geometries) reaches an asymptotic limit of $\pi/4$ at high frequencies, in the far field and the shadow zone [2.6]. Note that Equation 2.5 appears to predict a phase shift, however, this phase shift is not unique in that it is applied to all the paths. The unique diffraction effects for each path reside in the amplitude term of Equation 2.5.

2.2.3 Lam's method using Kurze and Anderson's equations

2.2.3.1 3D - Point source

Kurze and Anderson formulated an equation that determines the reduction of sound pressure level due to the insertion of a semi-infinite barrier between a point source and receiver [2.2]. A slightly modified version of their equation is

$$IL(dB) = -20\log\left(\frac{d(1 - \cot\frac{1}{2}(\theta - \alpha))}{2\pi(A + B)\sqrt{\frac{\delta}{\lambda}(1 + \frac{d}{A+B})}}\right) \tag{2.7}$$

See Figure 2.4 for an explanation of the symbols. Note the δ/λ term in the denominator. The symbol, δ, is the path length difference between the diffracted and the direct path (($A+B-d$) from Figure 2.4). For receivers close to the *line-of-sight* of the source, δ is small, and the equation diverges. Same can be said for large wavelengths λ, or low frequencies. Thus it would be reasonable to assume that this equation is more applicable for high frequencies and for receivers in the deep shadow region.

The pressure for each diffraction path in the form of Equation 2.1 for the 3D geometry implementing Kurze and Anderson's formulation can then be determined by

$$p_i = \frac{d_i}{d_o}\left(\frac{d(1 - \cot\frac{1}{2}(\theta - \alpha))}{2\pi(A + B)\sqrt{\frac{\delta}{\lambda}(1 + \frac{d}{A+B})}}\right)e^{j\frac{\pi}{4}}\frac{e^{-jkd_i}}{d_i} \tag{2.8}$$

27

This equation has the same properties as Lam's method implementing Maekawa's curve in that it only accounts for the amplitude change at the diffraction edge. Also note that the phase shift at diffraction edge is assumed to be the asymptotic limit of $\pi/4$ following Lam's suggestion for diffraction for 3D geometries. Using Kurze and Anderson's diffraction model, it is once again seen that the diffraction for each path is really only an amplitude adjustment, as all paths receive the same phase adjustment.

2.2.3.2 2D - Line source

Kurze and Anderson's equation for the 2D line source and semi-infinite barrier is similar to the one for the point source, except for a few variable changes.

$$IL(dB) = -20\log\left(\frac{d(1 - \cot\frac{1}{2}(\theta - \alpha))}{2\pi(A' + B')\sqrt{\frac{\delta_{max}}{\lambda}}(1 + \frac{d'}{A'+B'})}\right) \tag{2.9}$$

See Figure 2.4 for an explanation of the symbols. Noting the similarity between this equation and the one for the point source, it can also be said that this equation is valid for high frequencies and for receivers deep in the shadow region.

The idea of an amplitude change at diffraction for the 3D case is extended for the 2D line source case. The pressure for the ith diffraction path in the form of Equation 2.1 for the 2D geometry is determined by

$$p_i = \left(\frac{d(1 - \cot\frac{1}{2}(\theta - \alpha))}{2\pi(A' + B')\sqrt{\frac{\delta_{max}}{\lambda}}(1 + \frac{d'}{A'+B'})}\right)(-jH_0^{(1)}(kd_i)) \tag{2.10}$$

Note that a phase shift of $\pi/4$ was not introduced in this equation, as it was in Equation 2.8, since there was no justification to do so. Lam's suggestion was in the context of 3D goemetries, whereas Equation 2.10 is for 2D geometries. However, tests were conducted with the phase shift of $\pi/4$ introduced in Equation 2.10 and were compared to the case for without this phase shift and there was little difference between the two cases.

2.2.4 Lam's method using Pierce's equation for diffraction

Pierce formulated an approximate solution to the wave equation for the single-edge diffraction by a semi-infinite wedge [2.7]. His solution considers cases where the source and receiver are at large distances from the barrier in terms of wavelength. Figure 2.5 shows the geometry considered. Diffraction due to a semi-infinite thin screen is a special case where the angle β is equal to 2π.

2.2.4.1 3D - Point source

Pierce's equation reduces to the following for a 3D point source

$$p_i = [A_D(X_+) + A_D(X_-)]\left(\frac{e^{j\frac{\pi}{4}}}{\sqrt{2}}\right)\left(\frac{e^{-jkd_i}}{d_i}\right) \qquad (2.11)$$

where

$$A_D(X) = sign(X)[f(|X|) - jg(|X|)]$$

$$X_+ = X(\theta + \theta_o)$$

$$X_- = X(\theta - \theta_o)$$

$$X(\theta) = \left[\frac{2r_o r}{\lambda d_i}\right]^{\frac{1}{2}}[-2\cos\left(\frac{\theta}{2}\right)]$$

$$d_i = r_o + r$$

The functions f and g are series representation of Fresnel integrals and A_D is the Airy function. Since the Airy functions are complex functions, the diffraction effect for each path is a complex numerical value. Hence, Pierce's diffraction model determines a phase shift at the diffraction edge in addition to the amplitude change.

2.2.4.2 2D - Line source

In modifying Pierce's equation for a cylindrical source, the only change introduced is the term for cylindrical spreading.

$$p_i = [A_D(X_+) + A_D(X_-)]\left(\frac{e^{j\frac{\pi}{4}}}{\sqrt{2}}\right)(-jH_0^{(1)}(kd_i)) \qquad (2.12)$$

29

2.2.5 2D Impedance Plane

Chandler-Wilde and Hothersall studied 2D acoustic propagation above a homogenous impedance plane [2.12]. In addition to the direct and the ground reflected pressures, a p_β term is introduced. This is a correction term to adjust the pressure at the receiver due to the presence of the impedance plane. The pressure at the receiver in Figure 2.6 is thus given by

$$p = -jH_o^{(1)}(kr_o) - jH_o^{(1)}(kr') + 4p_\beta(k, r', \phi, \beta) \tag{2.13}$$

Note that the factor of 4 in front of the p_β term is due to the form of the kernel functions used for cylindrical spreading. The correction term p_β depends on the wave number k, the path length of the ground reflected wave r', the angle of incidence ϕ, and the relative impedance of the ground β. Further details on the correction term p_β can be obtained from [2.12].

The manner of the impedance plane application to barrier calculations is best described by illustration. Take, for example, path number 2 from Figure 2.1. This path is shown on an impedance plane in Figure 2.7. For hard ground, the pressure at the receiver would be

$$p_2 = A_2 e^{j\zeta_2}(-jH_o^{(1)}(kd_2))$$

where A_2 and ζ_2 are the amplitude and phase change at diffraction. With the introduction of the impedance plane, the pressure at the receiver is

$$p_2 = A_2 e^{j\zeta_2}(-jH_o^{(1)}(kd_2) + 4p_\beta(k, d_2, \phi_2, \beta))$$

where d_2 is the path length of path 2. However, for path 4 from Figure 2.1, there are two ground reflections present. For this path, the pressure at the receiver is determined by (as shown in Figure 2.8):

$$p_4 = A_4 e^{j\zeta_4}(-jH_o^{(1)}(kd_4) + 4p_\beta(k, d_4, \phi_{4,1}, \beta) + 4p_\beta(k, d_4, \phi_{4,2}, \beta))$$

2.2.6 Parallel Barrier Modelling

A source placed between two parallel barriers was modelled using the multiple image method with the diffraction based methods. Figure 2.9(a) shows parallel barriers of separation of d. A source is placed a distance x_1 from barrier number 1, x_2 from barrier number 2, and a height of h_s above ground. A receiver is placed on the far side of barrier number 2. This scenario would involve several reflections between the barriers. This can be modelled by replacing barrier number 1 with an infinite series of sources, in theory, as shown in Figure 2.9(b) [2.13]. The total pressure at the receiver is then determined by summing the pressure contributions from a large, but finite number of source images. In testing, it was found that anywhere from 50 to 200 images were required to achieve convergence. Note that such large number of images needed for convergence was verified by using the multiple image method with BEM to model parallel barriers.

2.3 Applications

2.3.1 Preliminaries

The results for the diffraction methods are compared to their wave-based counterparts, which will serve as the benchmark cases. The commercial software SYSNOISE [2.14], which uses both the boundary element and finite element methods to model acoustic problems, was used to provide wave-based results for comparison [2.15]. Convergence tests for each of the models was conducted to ensure sufficient number of nodes/elements were used in modelling of the barriers.

The diffraction results were calculated for both the shadow region, where the receiver is hidden from the source, and the illumination region, or the bright zone. The paths involved when the receiver is in the illumination region is shown in Figure 2.10 for the single barrier case. The coherent sum of the pressures from each path then provides the total pressure at the receiver location. For the parallel barrier case, the

sum of the pressure contributions from all of the source images from both barriers provides the total pressure when the receiver is in between the barriers (illumination zone).

The following results are provided as insertion loss. This is the difference in sound pressure levels with and without the barrier(s).

2.3.2   Two-Dimensional Studies

2.3.2.1   Single Barrier

The first test is that of a two-dimensional line source placed in front of a single infinite barrier. The barrier is 3 m high and the source is placed 0.5 m from the ground (rigid) and 7.5 m from the barrier. Figure 2.11 shows a comparison of the insertion loss at 250 Hz along a line that runs 1.5 m off the ground and 50 m on either side of the source. This comparison shows the 2D boundary element method modeling and the 2D Lam/Pierce and Lam/Kurze and Anderson (K&A) formulations. A remarkably good agreement is seen throughout the range, even though we might expect otherwise for receivers that are close to the barrier based on the assumptions for both Pierce's and K&A's models.

Figure 2.12 compares the same three methods for a directivity plot of the acoustic pressures at a radius of 10 m from the base of the barrier at a frequency of 250 Hz. Good agreement is observed over most of the angular range except in the line-of-sight region where the Lam/K&A method breaks down as expected. It should be noted that we could have made use of a special equation that Pierce developed for receivers close to this the line-of-sight region. However, it was not pursued owing to the good agreement in Figure 2.12 in this region with his original formulation.

The final test case for the single barrier is a frequency response. The same source and barrier positions are used, but now a receiver is placed 30 m from the source and 3 m from the ground. Figure 2.13 shows the comparison of the frequency response functions over a range of 2000 Hz. The three methods are nearly indistinguishable

except in the lower frequency range, where the Lam/K&A method begins to deviate slightly. This is expected as based on the frequency conditions of K&A's model and the fact that the receiver is not in the deep shadow region, leaving δ to be small.

2.3.2.2 Parallel Barrier

A line source is placed in between a set of 2D parallel barriers. The source is 0.5 m from the ground and the barriers are 3 m tall. Two different spacings of the barriers are considered: 15 m and 30 m. Figures 2.14 and 2.15 show a comparison of the insertion losses for barrier separations of 15 m and 30 m respectively. The source frequency is 1000 Hz and a line of receivers is placed 1.5 m from the ground running 50 m on either side of the source. This modeling scenario proves to be more of a challenge for the Lam/Pierce and Lam/K&A methods due to the multiple reflections between the barriers that take place. Both of the diffraction methods generally agree within 5 dB for the 15 m case and within 3 dB for the 30 m case. The 30 m separation exhibits better agreement due to the less enclosed setting and thus fewer reflections.

The multiple image method was also implemented with BEM. This yielded results that were close to the diffraction method results but different from the parallel barrier BEM model. This is thought to be because wave based methods, in addition to modeling multiple sound reflections between barriers, also model other, more complex, wave behaviours that may be occuring for a source in between parallel barriers.

Figures 2.16 and 2.17 compare the pressures at a 30 m radius from a 1000 Hz source with the barriers separated by 15 m and 30 m respectively. In both cases, the Lam/Pierce method shows much improved performance over the Lam/K&A model. This is especially true in the shadow regions of the barriers, where the diffraction of the multiple image sources is occurring. With the inability of K&A's model to account for phase shift at diffraction, the compounded error is large.

Figure 2.18 compares the frequency response for a point located 30 m from the source at a height of 3 m from the ground for the 30 m separation case. It is observed

that the Lam/K&A method exhibits large shortcomings over much of the frequency range, while the Lam/Pierce method is quite close. In these multiple reflection cases, we see the advantage in using the Pierce diffraction model due to its ability to be able to model both the amplitude and phase change at the barrier edge.

2.3.2.3   Finite Impedance Ground

The 2D impedance plane results are compared with a 2D acoustic finite element model [2.14] so that the effects of finite ground impedance could be considered. Figure 2.19 shows the sound pressure levels for hard ground and for relative ground admittances of $\beta = 0.1$ and $\beta = 0.5$. The Lam/Pierce diffraction results agree well with the finite element models over the tested range.

Figure 2.20 shows a frequency response over the range of 10,000 Hz for the impedance plane without taking a barrier into consideration. The heights of source and receiver are 0.5 m and 1.5 m, respectively, and d is the distance between the source and receiver. The familiar insertion dips due to the impedance plane are observed at approximately 300 Hz for $\beta = 0.5$ for all source-receiver distances shown.

2.3.3   Three-Dimensional Studies

In the first part of this paper, we explained three ways for calculating 3D acoustic pressures/insertion losses from diffraction methods: Lam/Maekawa, Lam/Pierce and Lam/K&A. These will now be compared against the 3D boundary element method. Figure 2.21 shows the insertion loss along a receiver line running perpendicular to a 30 m wide barrier. The source is placed 0.5 m from the ground (rigid) and 7.5 m from the barrier. Figure 2.21 compares the insertion loss of the four methods a source frequency of 250 Hz. All the diffraction models provide results that are close to the BEM results. There does not appear an advantage of one diffraction method over another in this case.

A polar plot of sound pressure at a distance of 30 m and a frequency of 250 Hz is

shown in Figure 2.22. In this figure it is seen that all methods yield good results at low angles and approximate results in the illumination areas above the source. Figure 2.23 shows a frequency response comparison for the three Lam methods. This figure shows the response from 0 to 2000 Hz for a point that is 30 m away from the barrier and 1.5 m from the ground. The three methods agree well over most of the frequency range, however the Lam/K&A method does deviate over the central frequency region. BEM results were not included in this test as large mesh sizes were required to satisfy the convergence criterion of 6 nodes per wavelength in the frequency range considered. As such, the computational requirements exceeded currently available computational abilities.

2.3.3.1   *Two and Three Dimensional Comparisons*

Having developed and verified efficient 2D and 3D barrier insertion loss calculational schemes, it is now possible to examine an issue of paramount importance; that being, how well do 2D prediction methods work for truly 3D geometries? Daumas [2.16] and subsequent authors compared insertion losses between 2D and 3D geometries and found close agreements between the two. The results can now be verified using BEM and the diffraction techniques discussed in this paper. However, for all of the preceding tests, the diffraction technique of Lam/Pierce was used. Figure 2.24 depicts the frequency response function of (i) a 2D line source and infinite barrier, (ii) a 3D point source and infinite barrier and finally (iii) a 3D point source and a 400 m finite length barrier. In all cases, the source is 0.5 m from the ground and 7.5 m from the barrier. The receiver point 30 m away from the source and 3 m off the ground. For this test, very little difference is observed between the three curves. The close comparison of the 3D point source in front of an infinite barrier and a finite length barrier is not surprising owing to the fact that the contribution of the side diffraction paths is small for the long barrier considered. The other aspect of this comparison is the indifference in the results between the point and line sources for the infinite

barrier model.

Figure 2.25 tackles this question from a slightly different point of view. Here a receiver location is selected 50 m from the barrier and the barrier width is changed from 10 to 2,000 m. This figure compares the insertion loss of a 2D geometry (i.e. line source, infinite barrier geometry) to that of a point source in front of a finite width barrier. For both the 250 Hz and 1000 Hz curve it is observed that after the barrier becomes about 300 m long that there is very little difference between the finite (3D) and infinite (2D) modelling. Figure 2.26 is more representative of when a finite barrier can effectively be considered infinite. For 6 different combinations of 3D source and receiver geometries, the octave average insertion losses for 250, 500 and 1000 Hz center frequencies were calculated (with Lam/Pierce model for 3D geometries) and normalized (source locations - 7.5, 15, and 30 m away from the barrier, at a height of 0.5 m; receiver locations - 50 and 100 m away from the barrier, at a height of 1.5 m). It is observed that, from all the cases, barrier widths in excess of 300 m can effectively be assumed to be infinite.

2.3.3.2   Point and Line Sources

A series of 3D point sources were used to model a 3D line source. Various test cases were considered for the source spacings and the line source lengths. It was initially determined that there must be at least four sources per smallest wavelength considered. Additionally, the length of the approximated line source was increased until convergence was achieved. As an example, Figure 2.27 compares the 2D boundary element method frequency response (from Figure 2.12) to that approximated by a 400 m line source with a source spacing of 0.05 m. The receiver is 30 m from the source and 3 m above the ground. A good agreement is seen thus indicating that the length and spacing of the line source closely approximates an ideal line source for the frequency range considered.

Figure 2.27 considered a coherent line source, whereas, an incoherent line source

36

is of more interest from a traffic noise point of view [2.17]. With the possibility of approximating a line source as a series of point sources, this test is possible by assigning, at random, a phase shift to each point source. Figure 2.28 compares the one-third octave averages for a 2D coherent line source and a 3D incoherent line source for the same source, receiver and barrier geometries as in Figure 2.27. There is a significant difference between the two cases. However, the differences depend on the relative positions of source and receiver, and, as Figure 2.28 indicates, on the frequency content of the source. It should be noted that for a 3D incoherent line source, source spacings between 0.05 m and 20 m were tested to find little difference between them for the geometry considered in Figure 2.28.

Current limitations are that only coherent line sources can be taken into account in 2D techniques and the only way to model an incoherent line source is with a series of point sources. A worthwhile test would be to develop correction factors that could be factored into 2D coherent source results to transform the results to those for an incoherent line source (for traffic flow purposes).

2.4 Conclusions

To overcome the limitations of traditional wave-based modeling, the diffraction based modeling principles of Lam were extended to include the diffraction models of Pierce and Kurze and Anderson, modeling of 2D geometries, the consideration of parallel barriers, modeling the effect of finite ground impedance, and the consideration of 3D coherent and incoherent line sources. In general, comparisons with the BEM showed that the diffraction models agreed well for both the single and parallel barrier geometries. However it was noted that the Lam/K&A method fell short when the receivers were in the proximity of the line-of-sight, and when parallel geometries in 2D were considered. This is due to the fact that this method does not predict a unique phase shift at the diffraction edge for each path.

A finite impedance ground plane was incorporated into the 2D modeling scheme

using the work of Chandler–Wilde et al. Single barrier tests on an impedance plane compared well with the FEM. 2D and 3D modeling strategies where also compared. It was found that barriers longer than 300 m could be well approximated by a simple 2D model with a line source. Finally, 3D coherent and incoherent line sources were compared to the 2D model. Our testing showed large differences in the 2D line model compared to the 3D incoherent line source case.

The major conclusion of this work is that improved diffraction based models, like those presented in this paper, compare well with and can indeed be used in place of the computational intensive wave based modeling methods like the BEM. As an example, consider the frequency response curve in Figure 2.13. BEM calculations on an IBM RS 6000 machine took several hours, whereas the diffraction based models produced the same results in a few seconds on the same machine. The wave based accuracy and diffraction based calculation times of these modeling enhancements now permit fast, accurate predictions of large-scale environmental noise problems.

2.5 Future work

The insertion losses reported in this paper are rarely equaled in full-scale experimental tests. This is due to the fact that the modeling assumes a stationary, uniform acoustic fluid. This is in contrast to real life, where temperature gradients and wind greatly affect the transmission of sound energy. The focus of the current research is to model these non-uniform atmospheric effects. This research is being undertaken in much the same fashion as it developed for this paper: first to work with and understand the exact solutions to simple problems of this type using methods like the Fast Field Program and Parabolic equation solution and to then later adapt a ray-based approach to give similar results for a fraction of the calculation time.

2.6 Acknowledgments

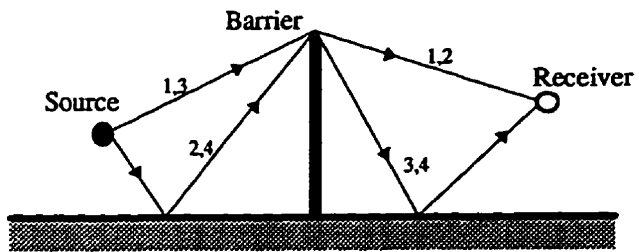**Figure 2.1:** Diffraction paths for a 2D barrier geometry.
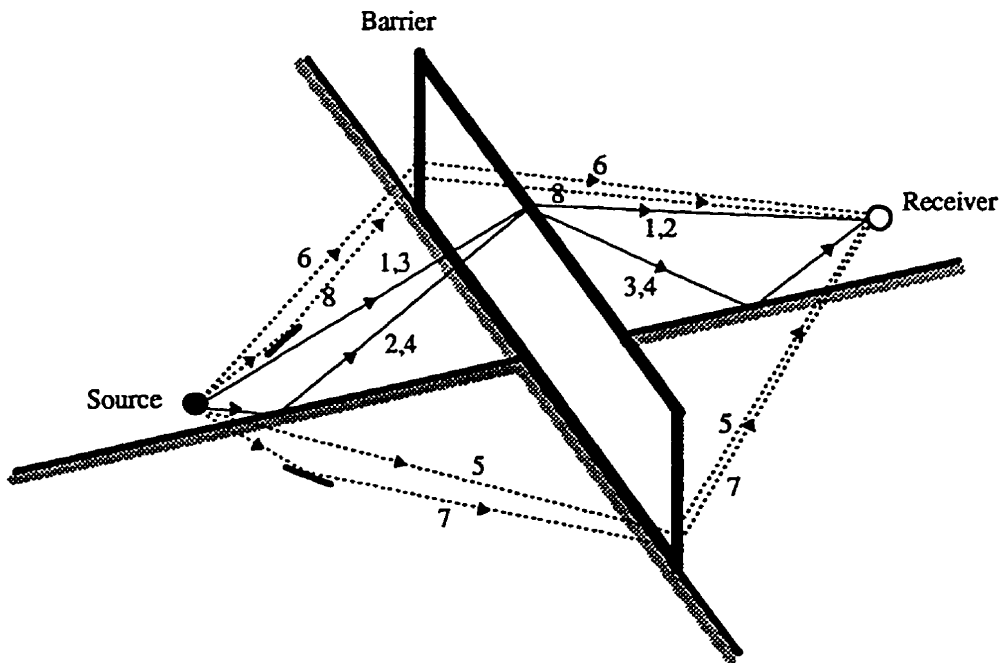
Figure 2.2: Diffraction paths for a 3D finite length barrier geometry.
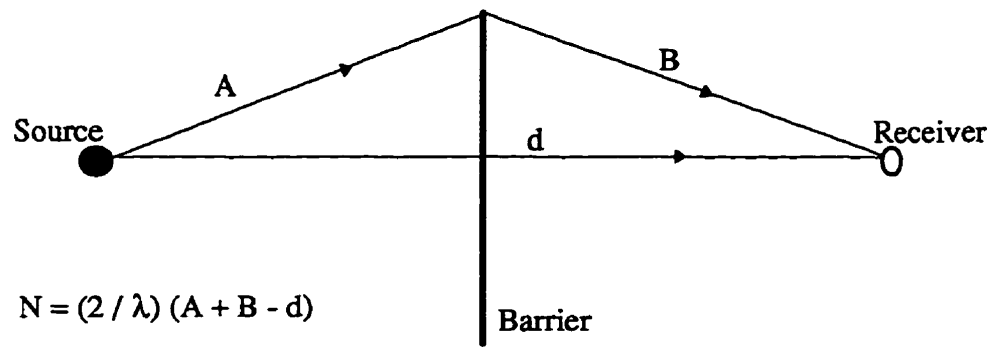
40

$$N = (2 / \lambda) (A + B - d)$$

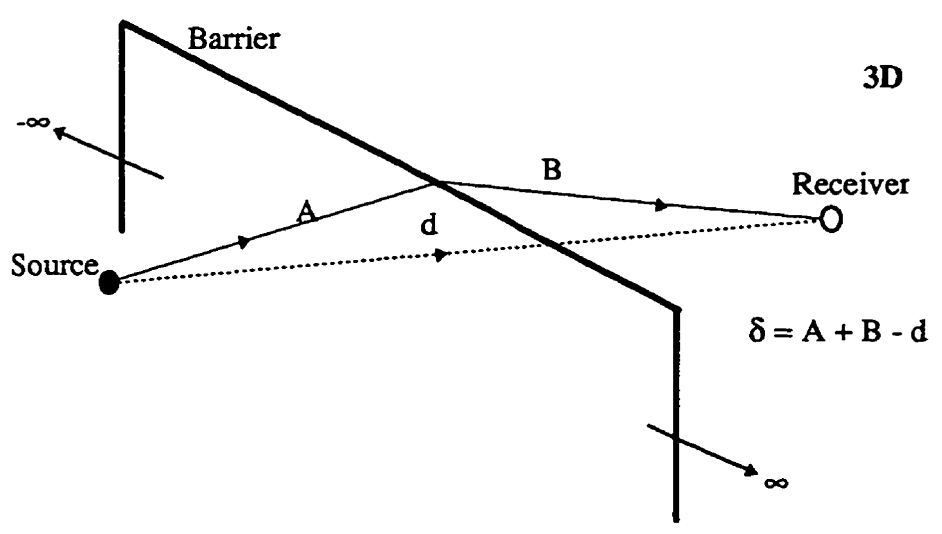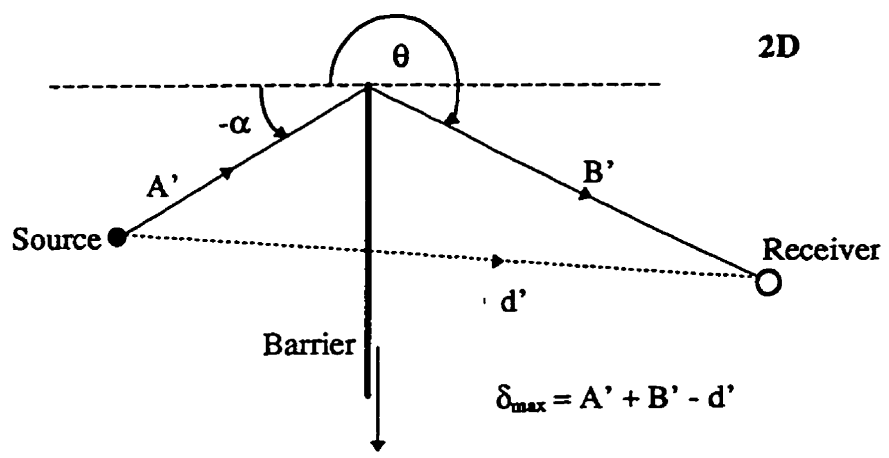**Figure 2.3:** Definition of symbols used to determine the Fresnel number, N.

Figure 2.4: Definition of symbols used in Kurze and Anderson's 2D and 3D diffraction models.
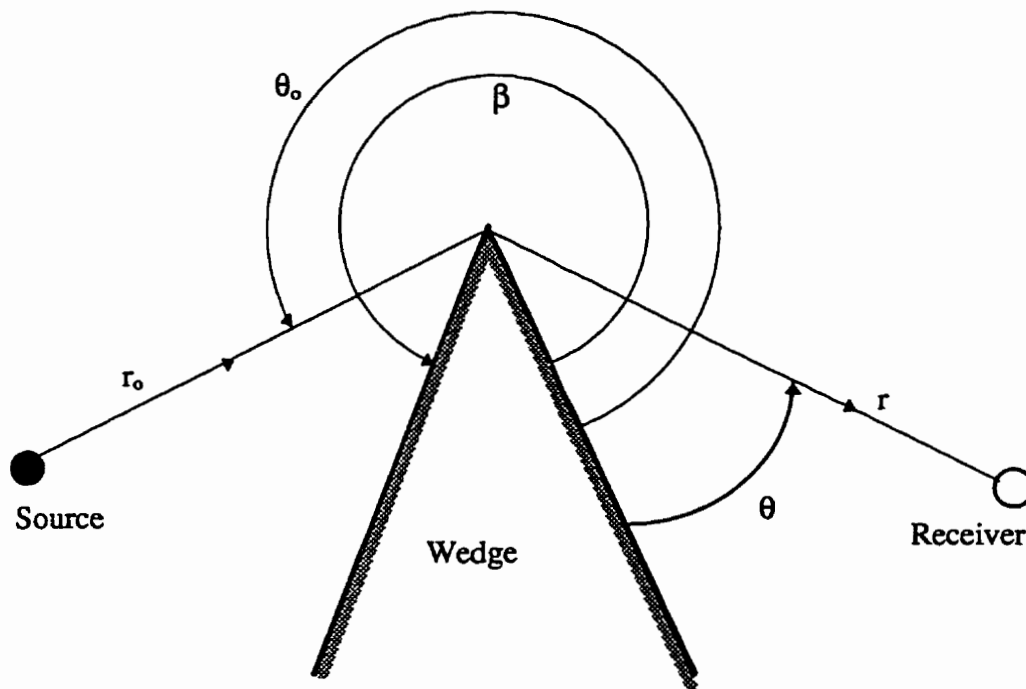
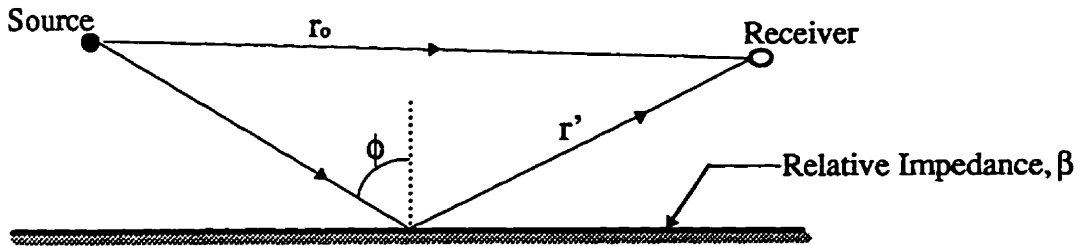**Figure 2.5:** Definition of symbols used in Pierce's diffraction model.

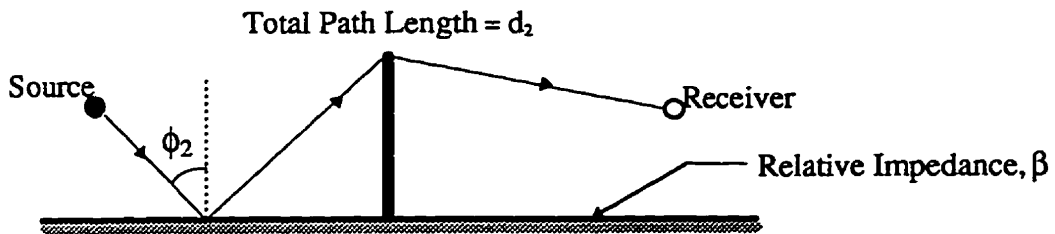**Figure 2.6:** Source and receiver above ground with finite impedance.

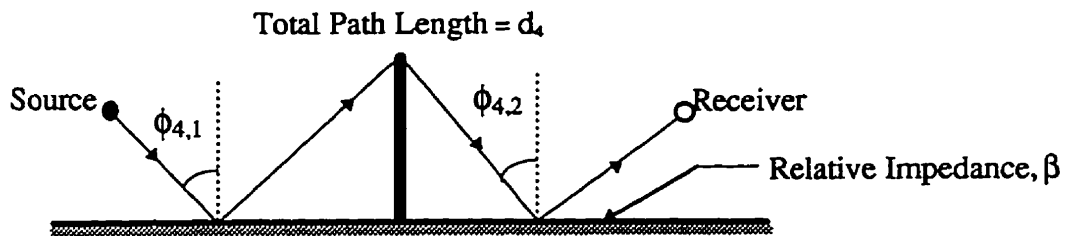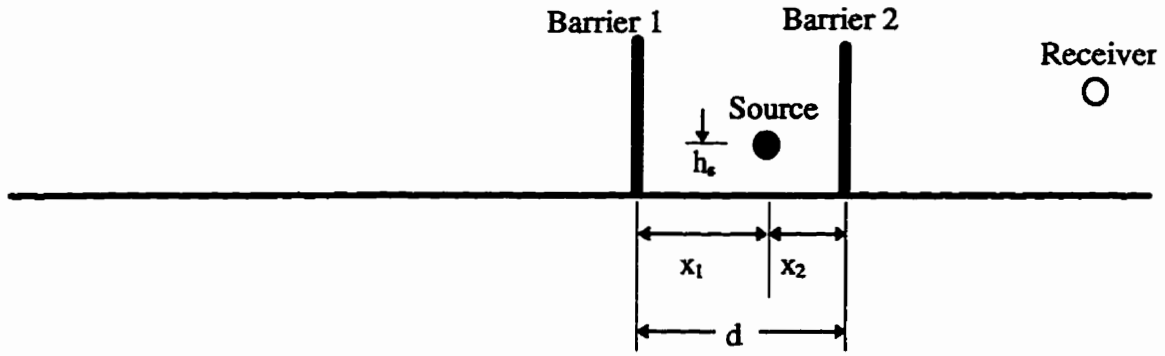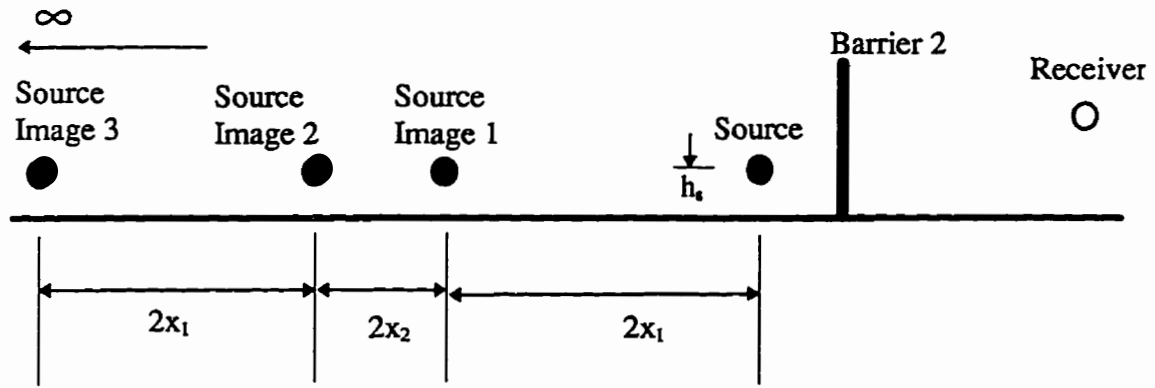**Figure 2.7:** Path 2 for the 2D barrier geometry with impedance plane.

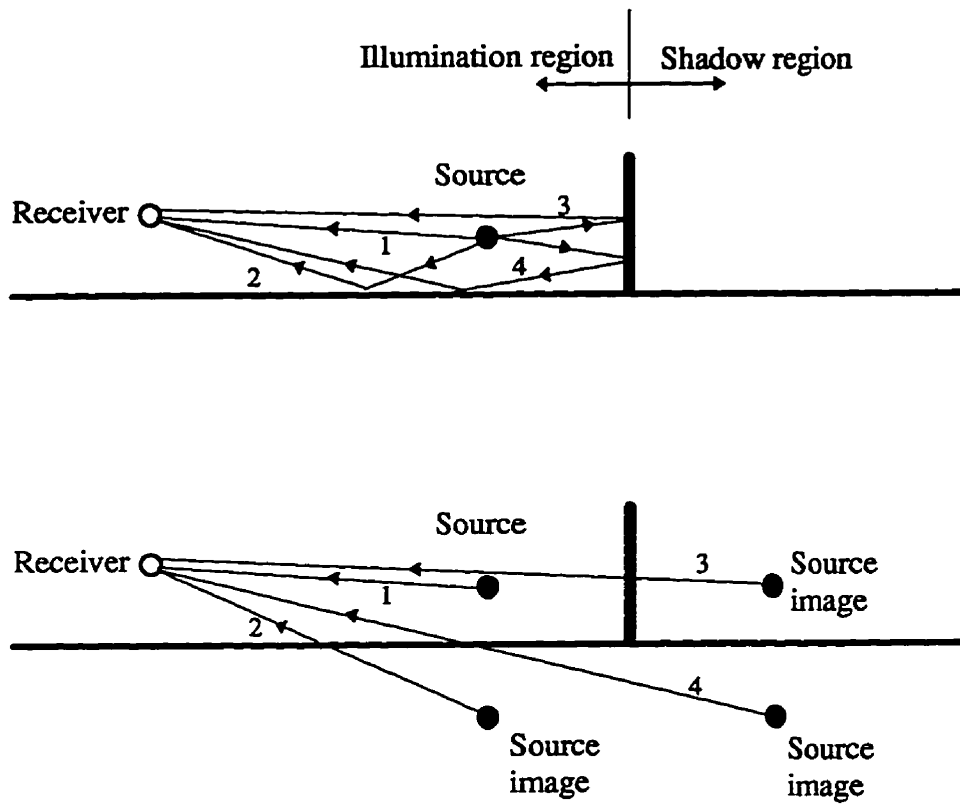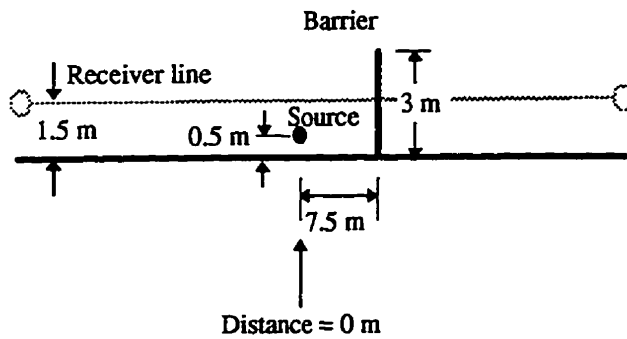**Figure 2.8:** Path number 4 for the 2D barrier geometry with impedance plane.

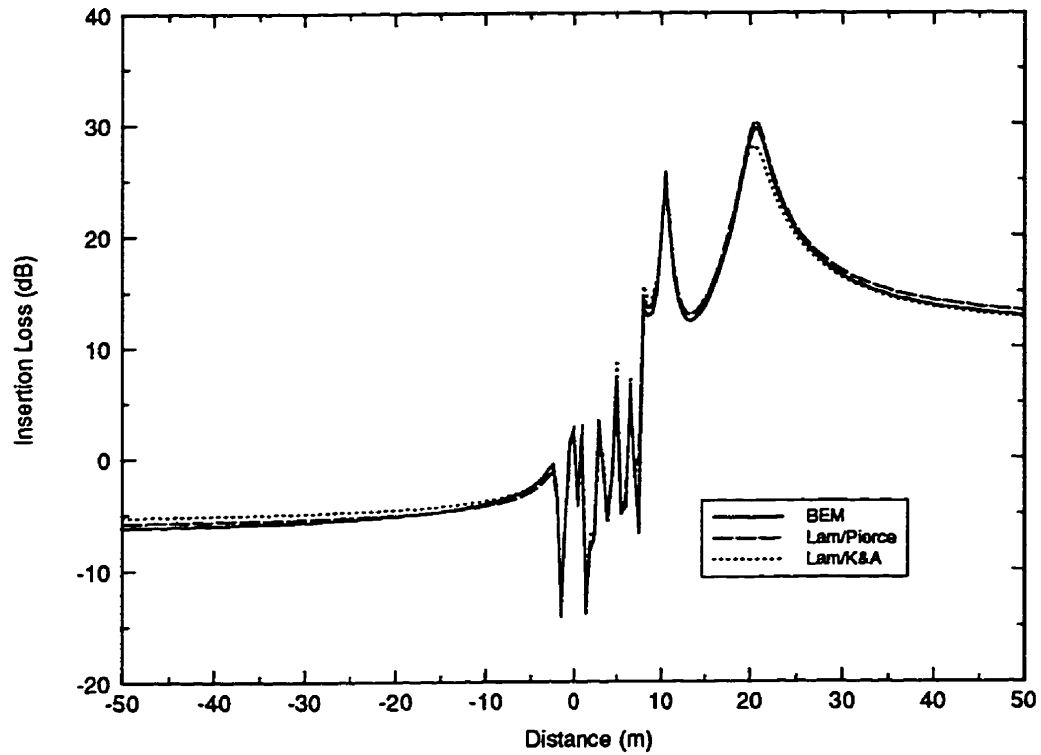**Figure 2.9:** The multiple image method used to model 2D parallel barrier geometry.

Figure 2.10: Paths considered when the receiver is in the illumination zone for single barrier geometry.

Figure 2.11: Single barrier insertion loss along a line at 250 Hz.
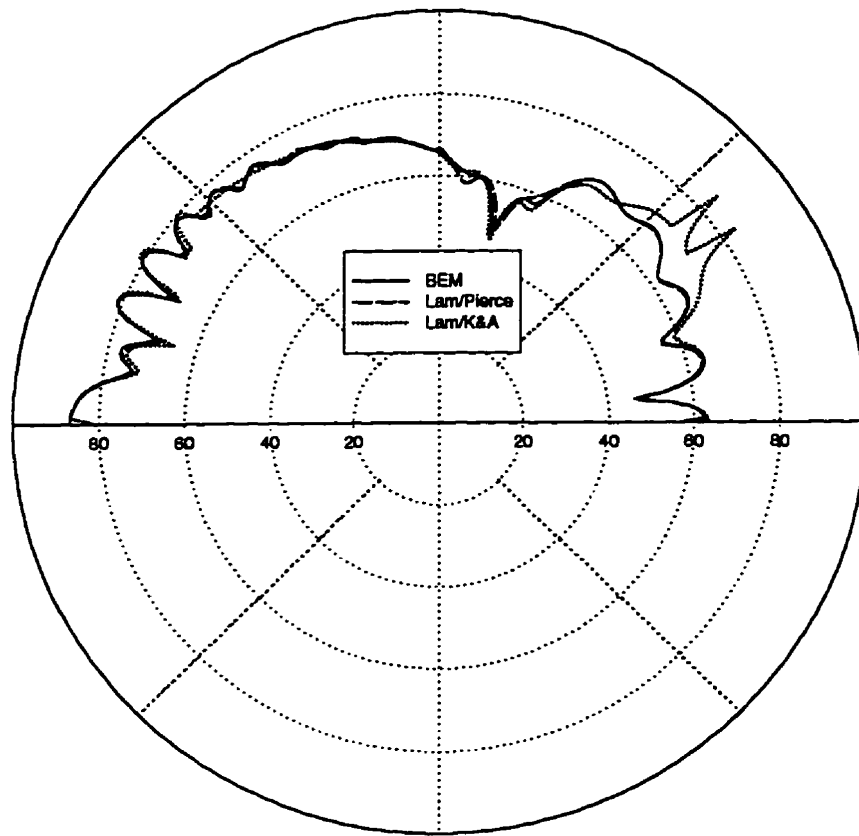
Receiver Radius = 10 m

Figure 2.12: Polar plot of sound pressures for single barrier at 250 Hz.
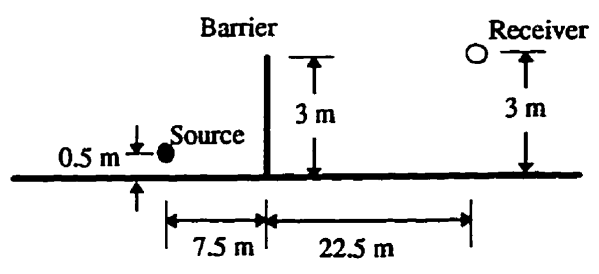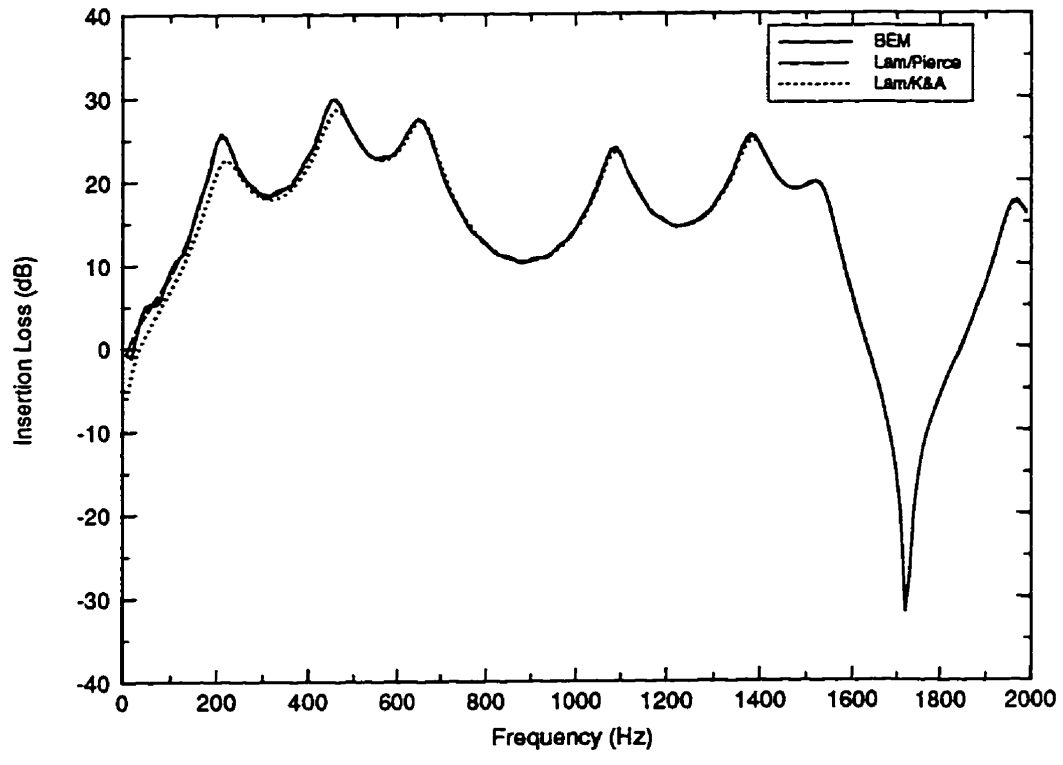
Figure 2.13: Single barrier frequency response.
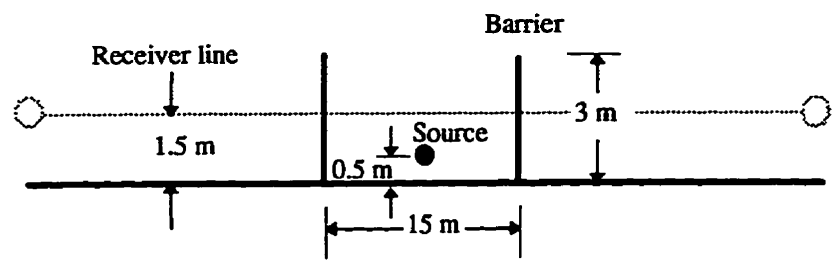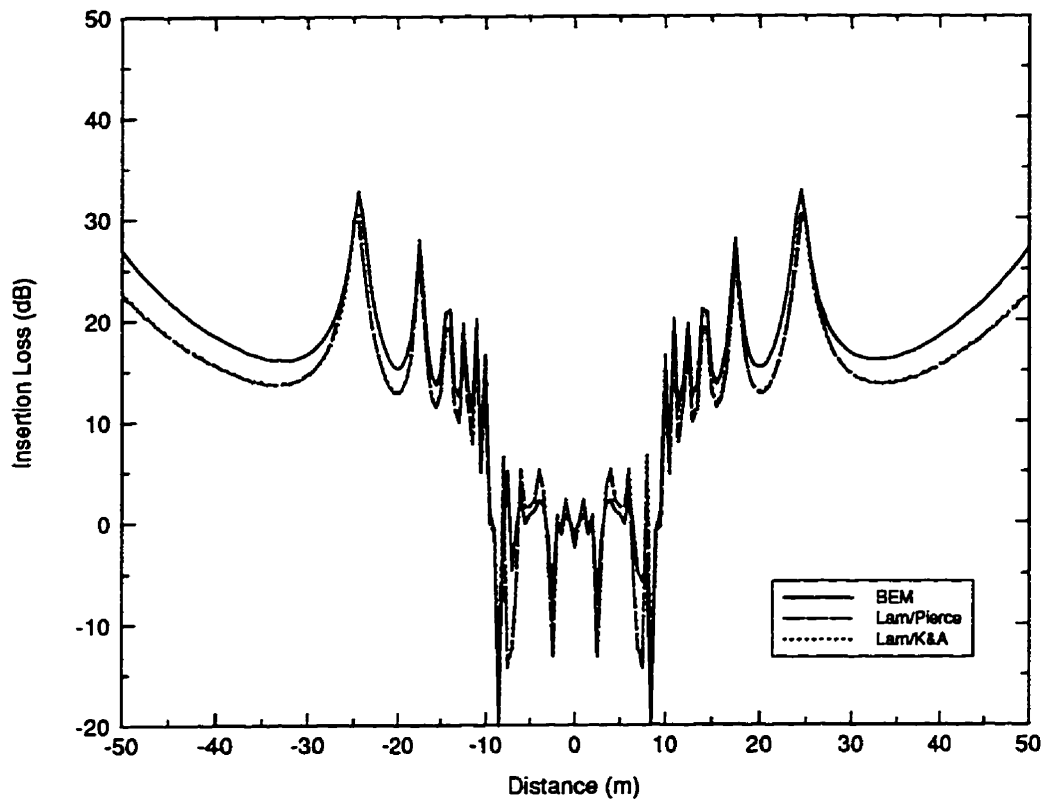
Figure 2.14: 15 m separated parallel barrier insertion loss along a line at 1000 Hz.
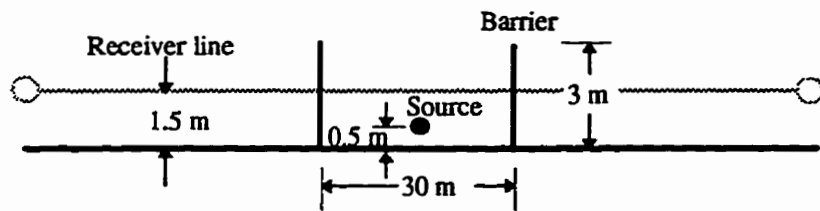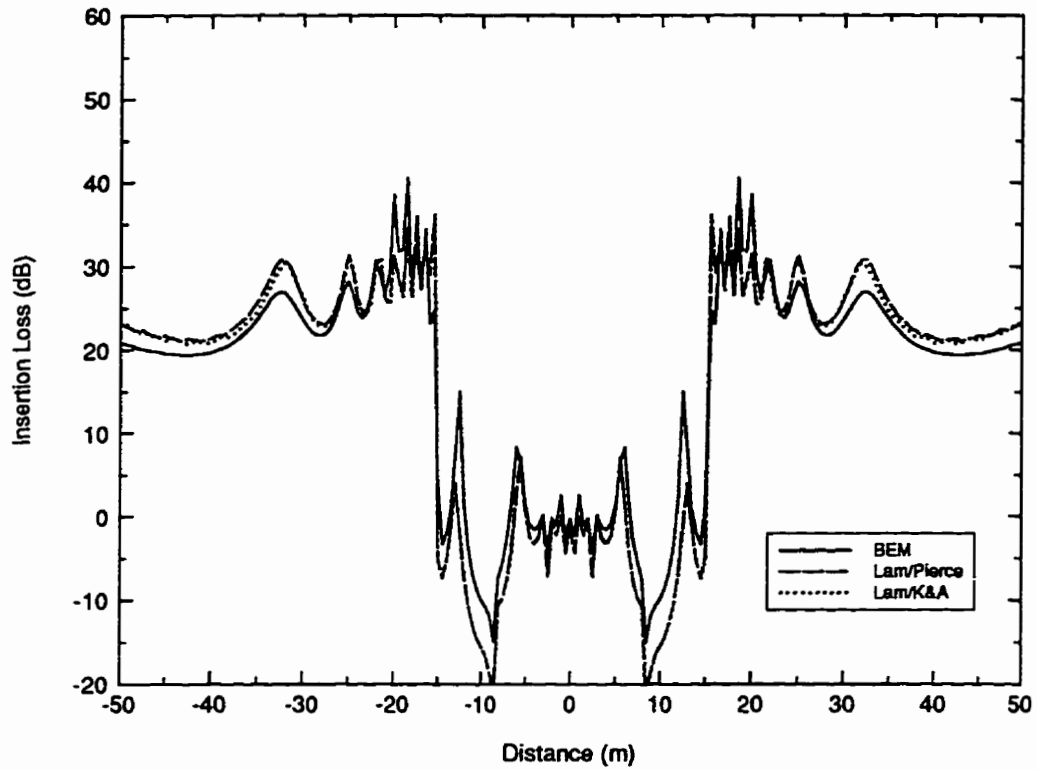
Figure 2.15: 30 m separated parallel barrier insertion loss along a line at 1000 Hz.
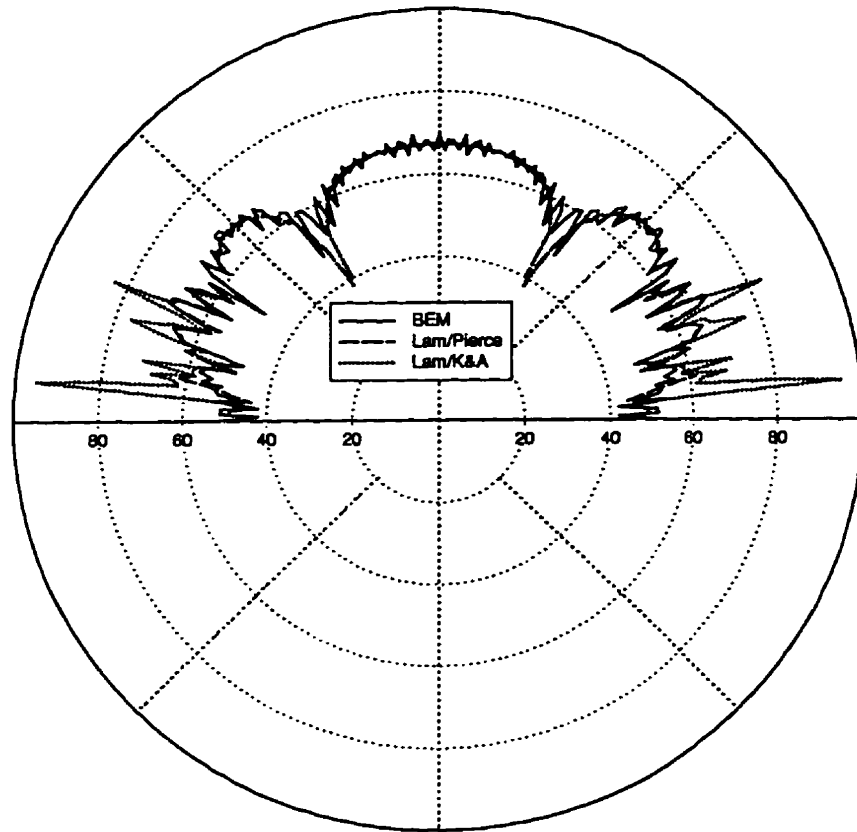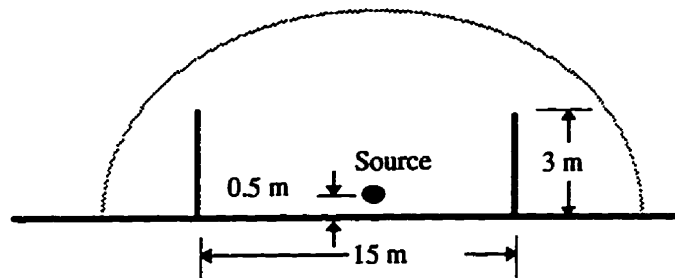
Figure 2.16: Polar plot of sound pressures for 15 m apart parallel barriers at 1000 Hz.
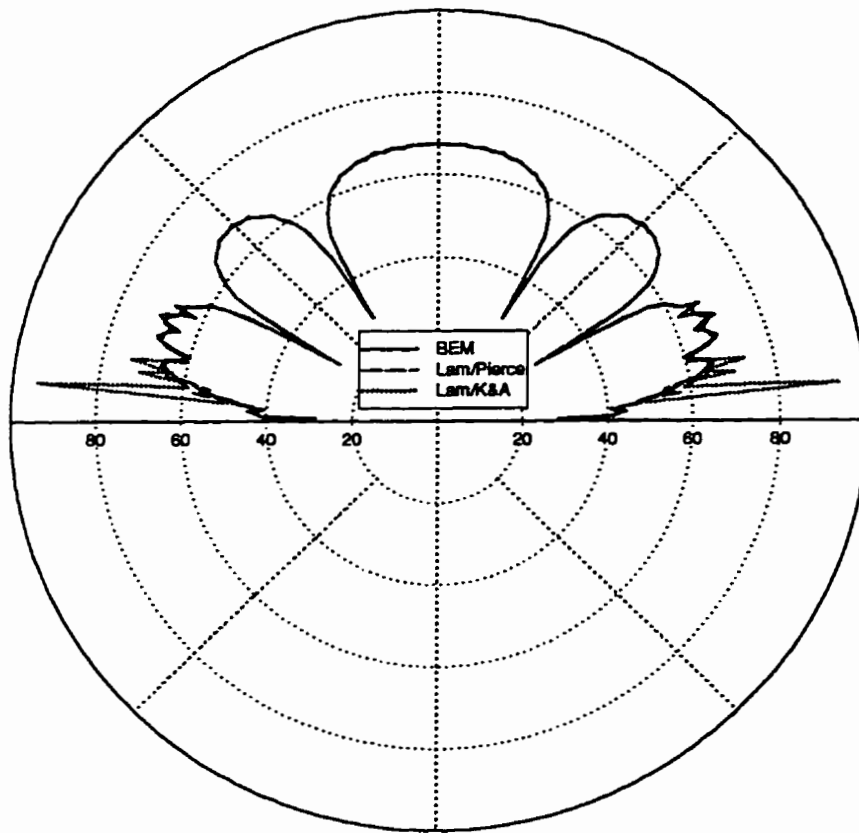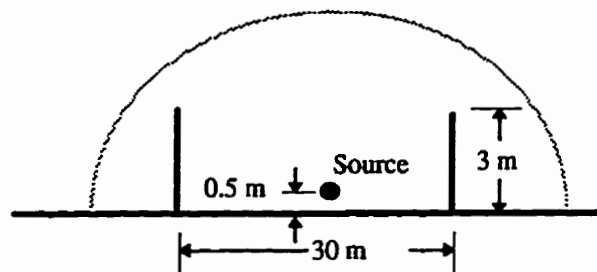
Figure 2.17: Polar plot of sound pressures for 30 m apart parallel barriers at 1000 Hz.
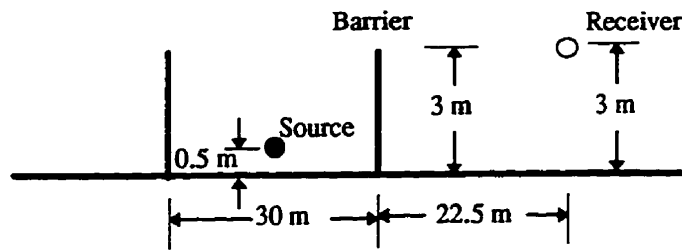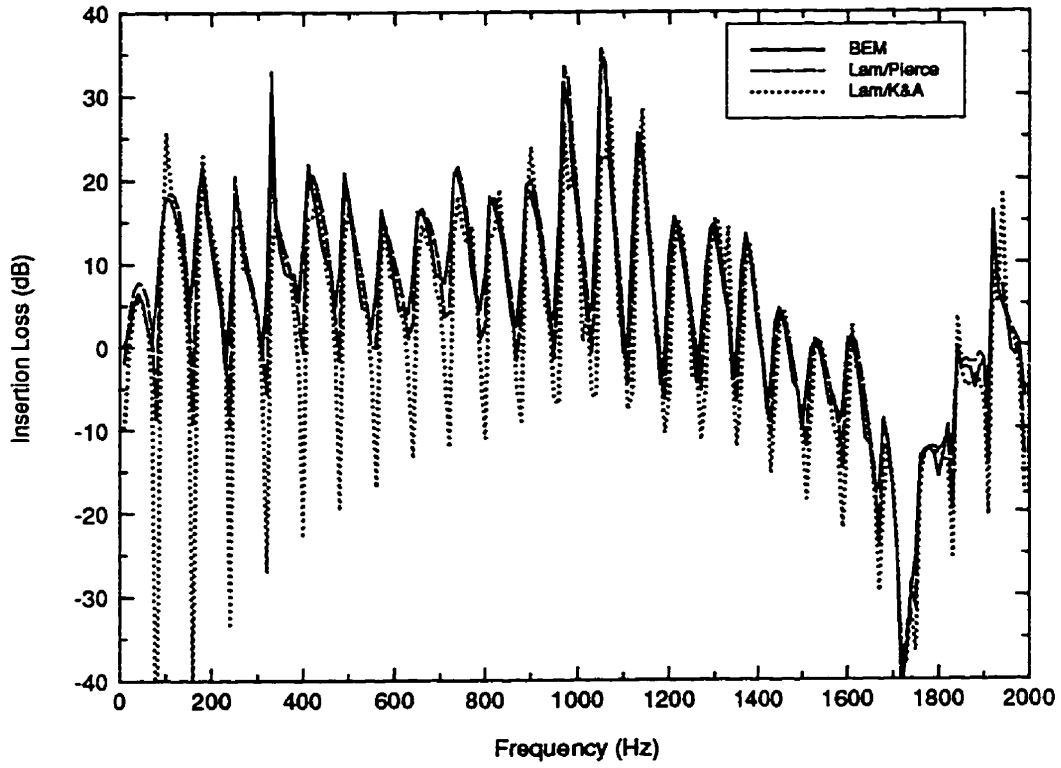
Figure 2.18: 30 m parallel barrier frequency response.
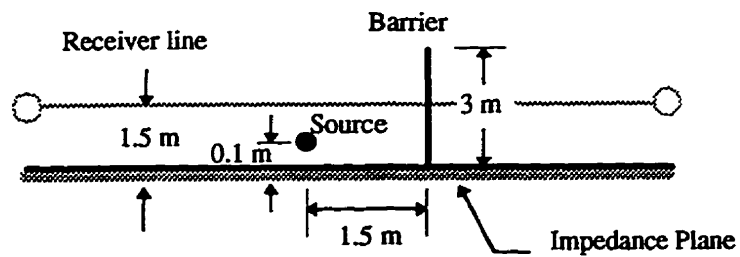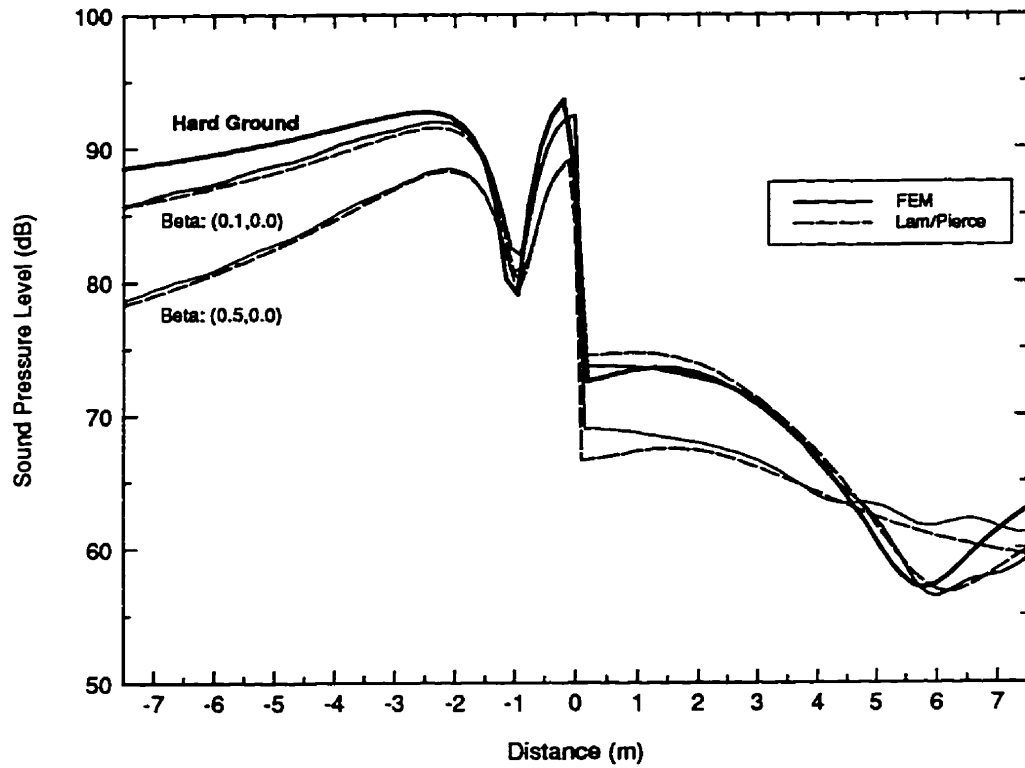
Figure 2.19: 2D Single barrier with impedance plane at 125 Hz. The relative ground admittance - Beta.
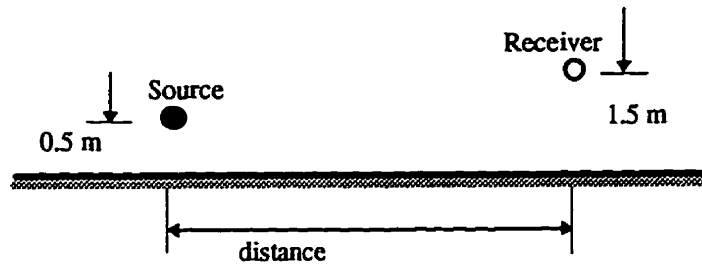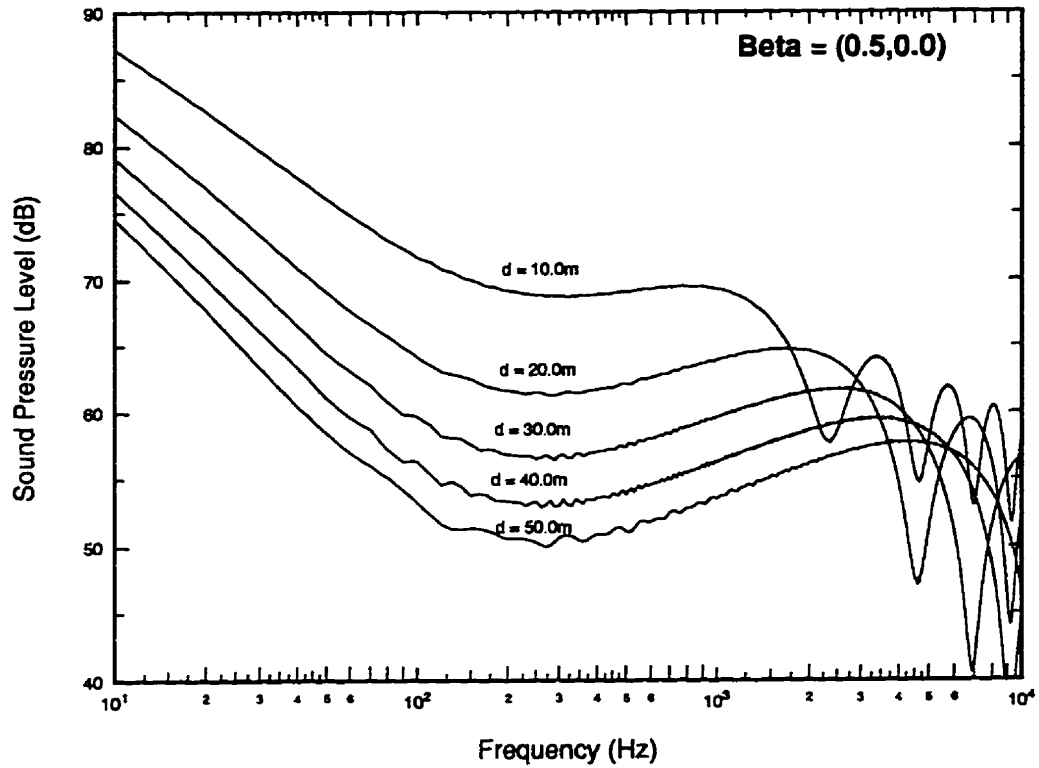
Figure 2.20: The occurrence of the impedance dip as a function of source-receiver separation.
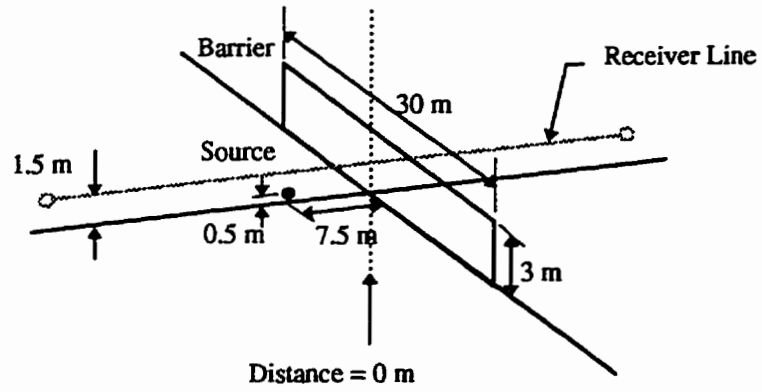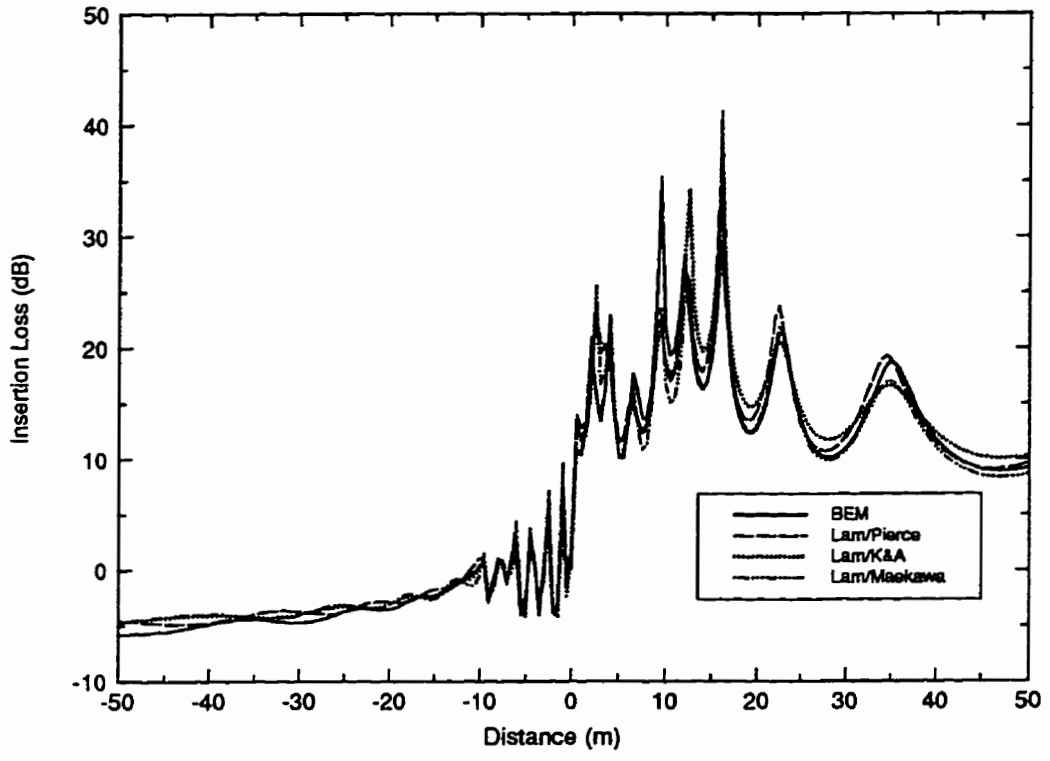
Figure 2.21: 3D Single barrier insertion loss at 250 Hz.
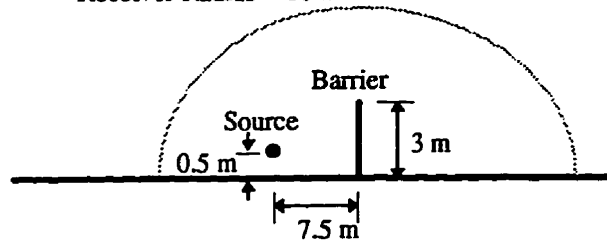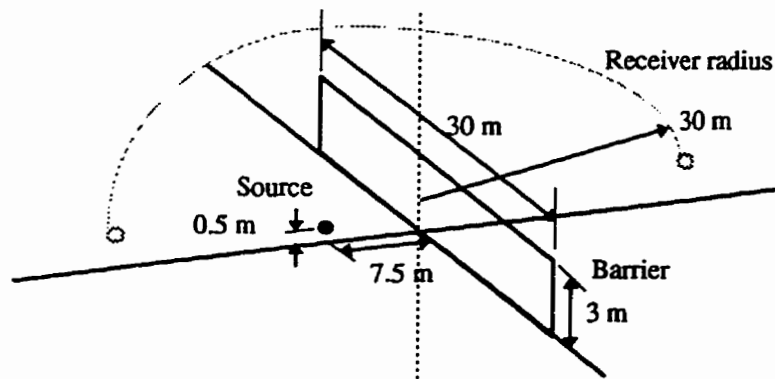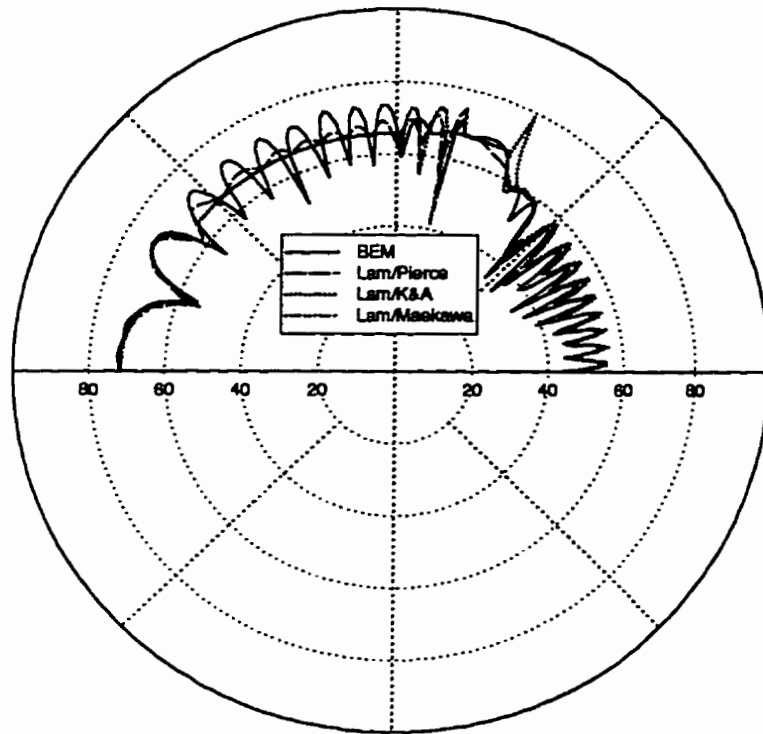
**Figure 2.22:** Polar plot of sound pressures for single barrier in 3D at 250 Hz.
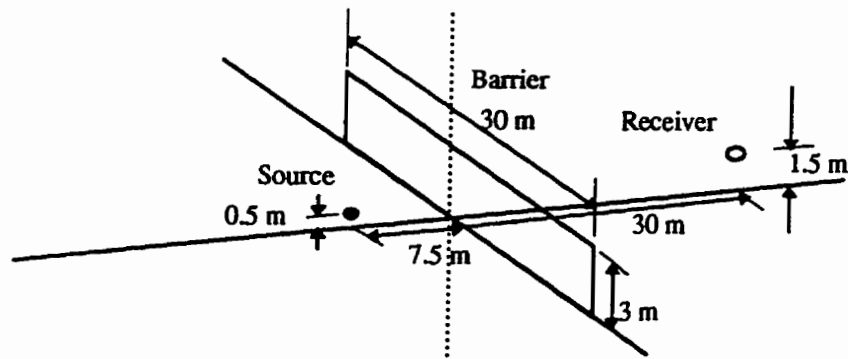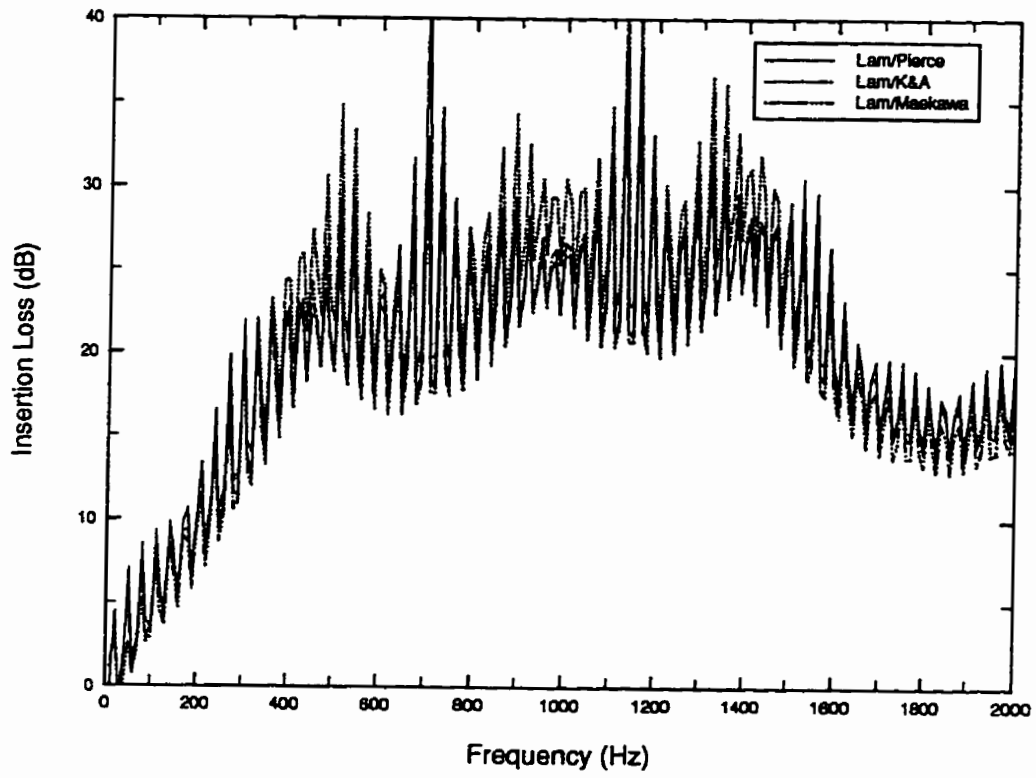
Figure 2.23: 3D Single barrier frequency response.
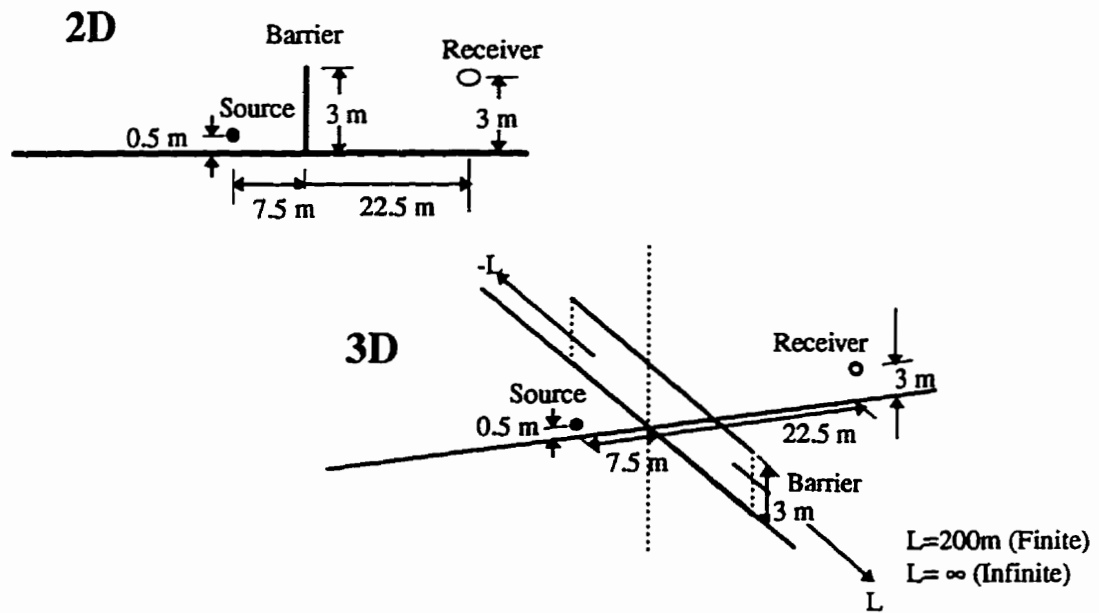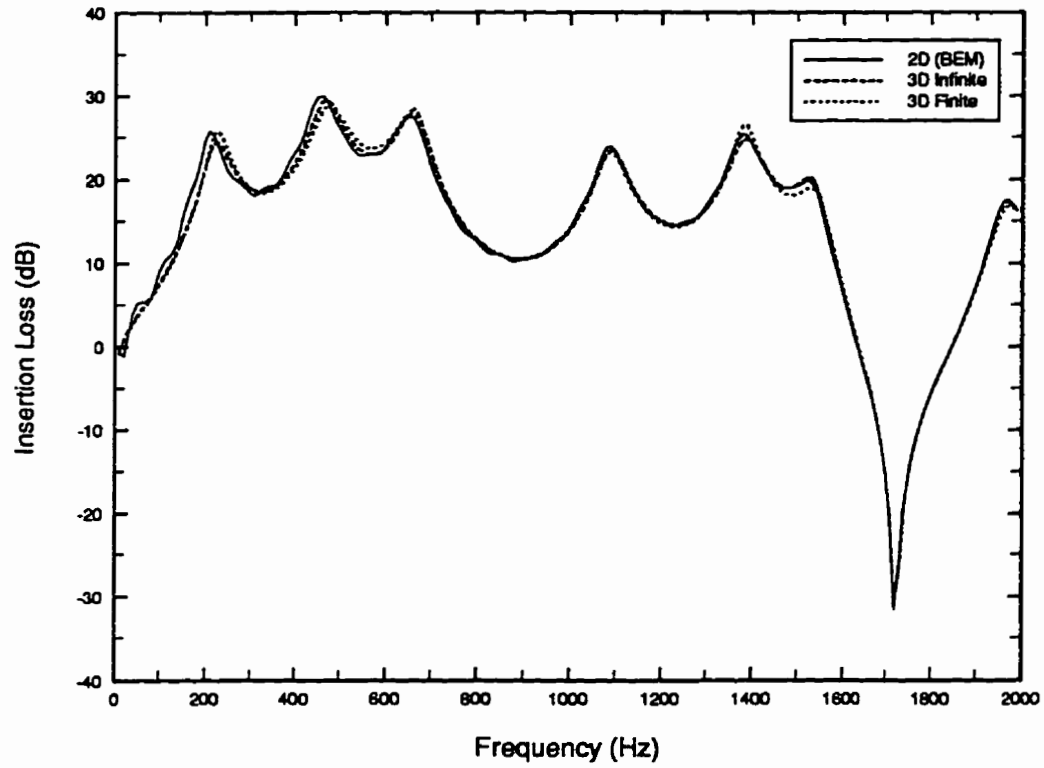
Figure 2.24: Comparisons between 2D, 3D infinite and 3D finite barrier width cases.
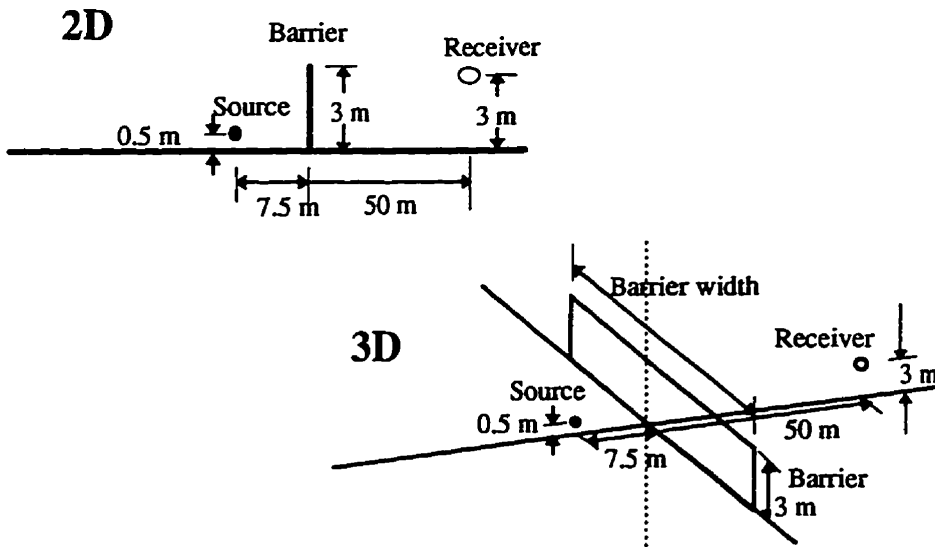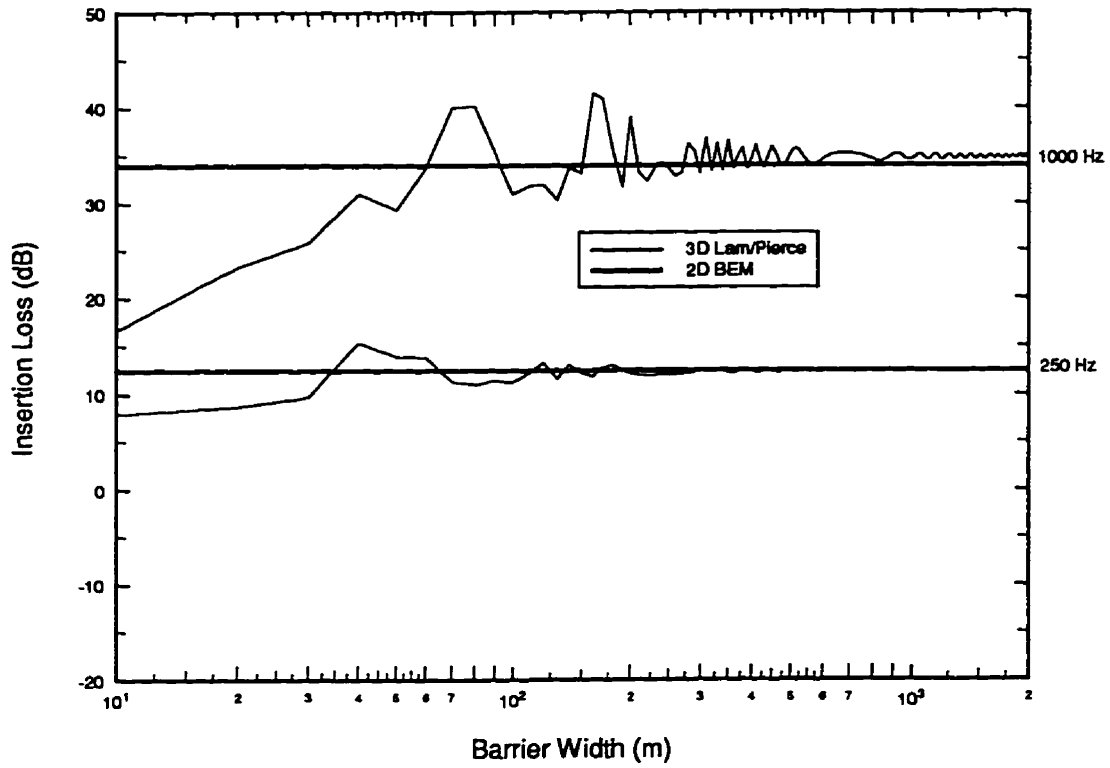
Figure 2.25: Comparisons between 2D and 3D barrier geometry by varying 3D barrier width.

61
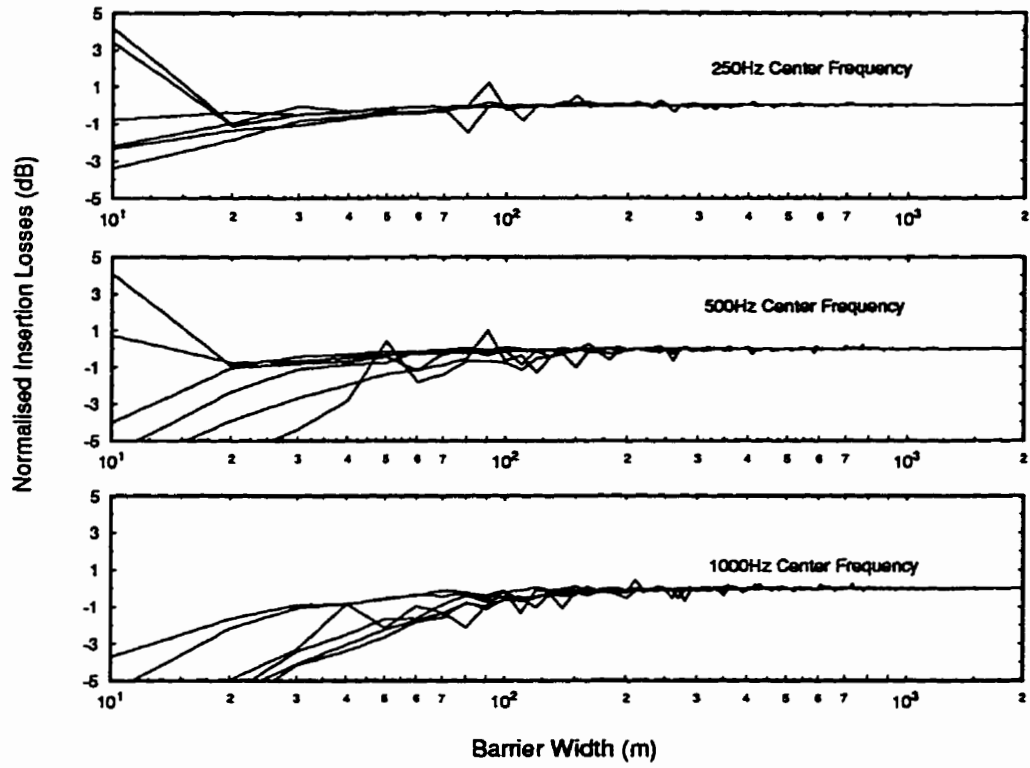
Figure 2.26: Normalized octave average insertion losses at various source-receiver locations for varying 3D barrier width.

62
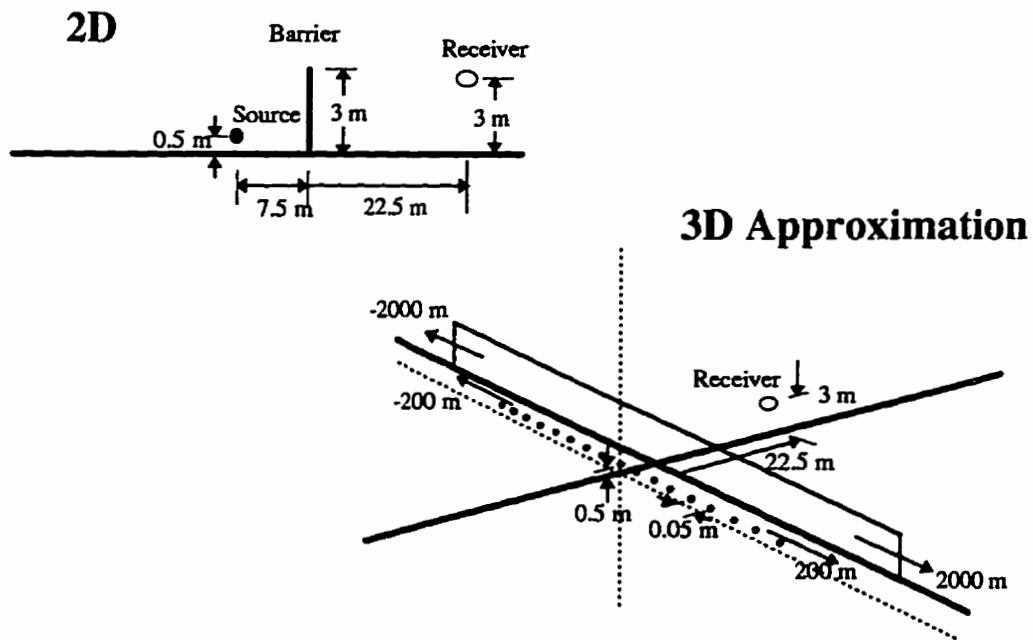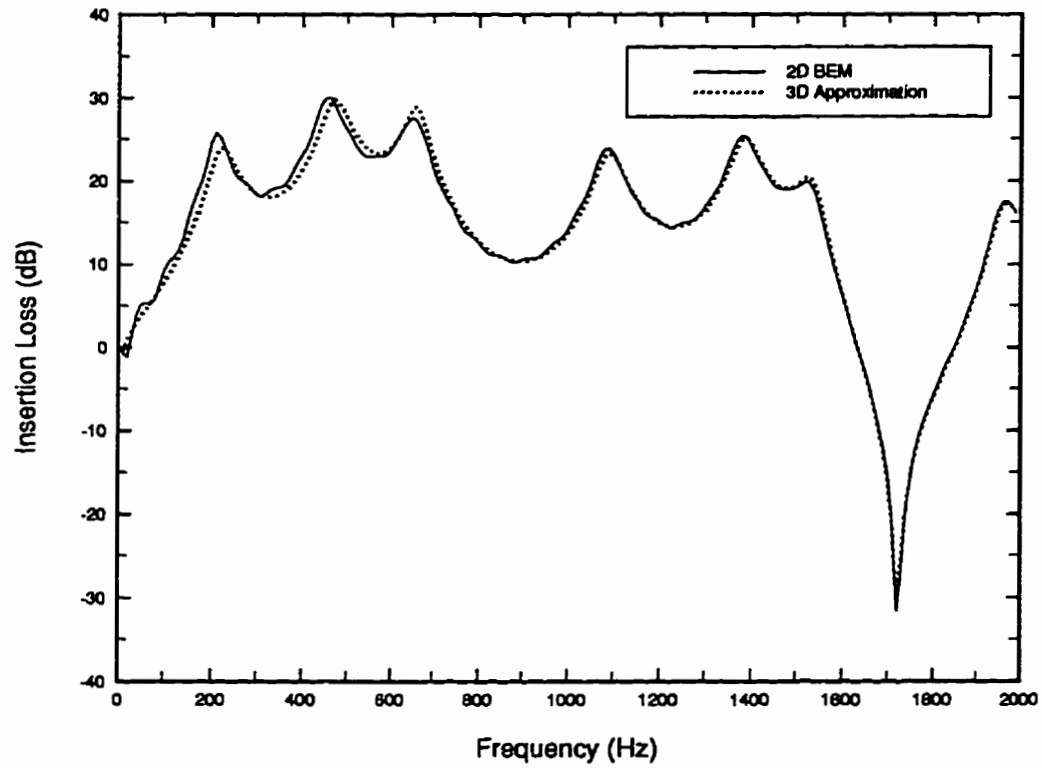
Figure 2.27: Line source approximation in 3D with a series of point sources.
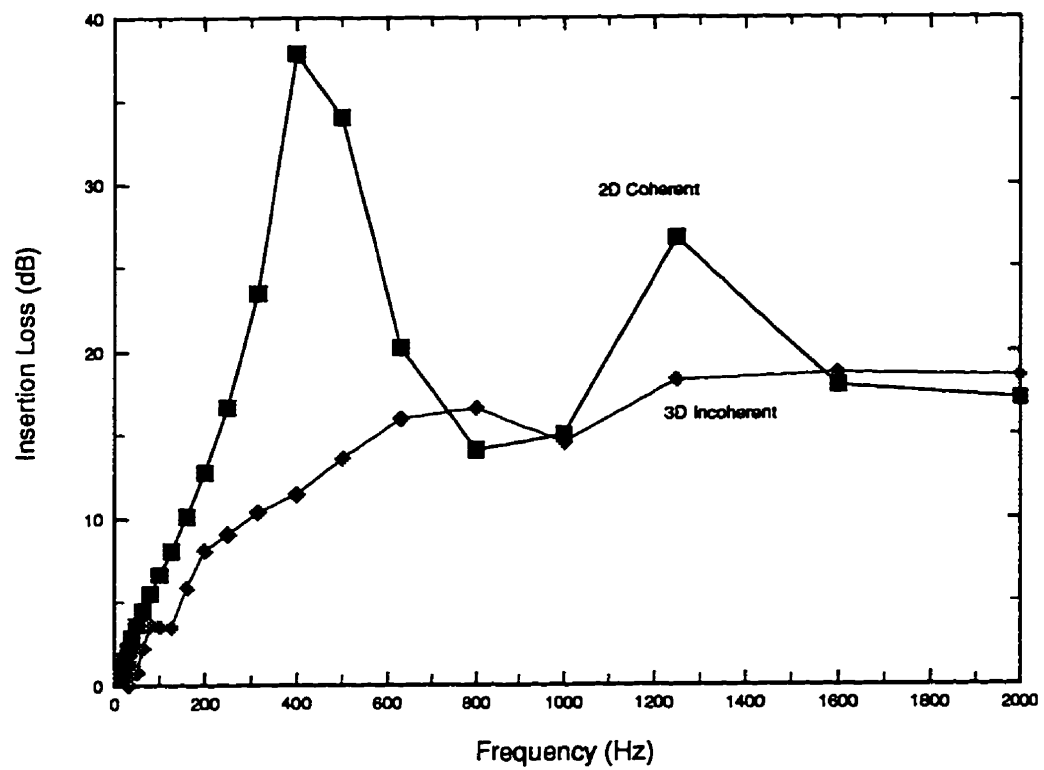
Figure 2.28: Third octave results for 2D coherent and 3D incoherent line sources.

References

2.1 Maekawa, Z., Noise reduction by screens, *Appl. Acoust.*, **1** (1968) 157-173.

2.2 Kurze, U. J. & Anderson, G. S., Sound attenuation by barriers, *Appl. Acoust.*, **4** (1971) 35-53.

2.3 L'Esperance, A., The insertion loss of finite length barriers on the ground. *J. Acoust. Soc. Am.*, **86** (1989) 179-183.

2.4 Kawai, Y. & Terai, T., The application of integral equation methods to the calculation of sound attenuation by barriers. *Appl. Acoust.*, **31** (1990) 101-117.

2.5 Pirinchieva. R., Model study of the sound propagation behind barriers of finite length, *J. Acoust. Soc. Am.*, **87** (1990) 2109-2013.

2.6 Lam, Y. W., Using Maekawa's chart to calculate finite length barrier insertion loss, *Appl. Acoust.*, **42** (1994) 29-40.

2.7 Pierce, A. D., Diffraction of sound around corners and over wide barriers. *J. Acoust. Soc. Am.*, **55** (1974) 941-955.

2.8 Hayek, S., Mathematical modeling of absorbent highway noise barriers. *Appl. Acoust.*, **31** (1990) 77-100.

2.9 Hothersall, D.C. Chandler-Wilde, S.N. & Hajmirzae, M.N., Efficiency of single noise barriers. *J. Sound Vib.*, **146** (2) (1991) 303-322.

2.10 Fyfe, K.R. & Harrison, C.C., Modeling of road noise and optimal barrier design, *CMHC report #6585/F039* (1995).

2.11 Cremers, L. & Fyfe, K.R., On the use of variable order infinite wave envelope elements for acoustic radiation and scattering, J. Acoust. Soc. Am., 97 (4) (1995) 2028-2040.

2.12 Chandler-Wilde, S. N. & Hothersall, D. C., On the green function for two-dimensional acoustic propagation above a homogeneous impedance plane. Research project, Department of Civil Engineering, University of Bradford. UK. (1991).

2.13 Raymond Panneton, Andre L'Esperance, Jean Nicolas, & Gilles A. Daigle, Development and validation of a model predicting the performance of hard or absorbent parallel noise barriers. *J. Acoust. Soc. Jpn.* (E) **14**, 4 (1993) 251-258

2.14 SYSNOISE acoustic modeling software, LMS/NIT Belgium, ver 5.3 (1996).

2.15 R. Seznec, Diffraction of sound around barriers: use of boundary element techniques. *J. Sound and Vib.* **73**(2), 1980, 195-209

2.16 A. Daumas, 1978 *Acustica* **40**, 213-222. Etude de la diffraction par un ecran mince dispose sur le sol.

2.17 D. Duhamel, Efficient calculation of the three-dimensional sound pressure field around a noise barrier. *Journal of Sound and Vibration* (1996) **197**(5), 547-571.

CHAPTER 3

ACCURATE BARRIER MODELING IN THE PRESENCE OF ATMOSPHERIC EFFECTS[1]

3.1 Introduction

There are numerous techniques for determining the performance of noise barriers. The more commonly used techniques in practice are diffraction based because of their calculational efficiency [3.1, 3.2, 3.3, 3.4, 3.5]. These techniques are based on geometrical ray theory and extend the theory of optical diffraction to that of acoustic waves. These techniques are primarily energy based and thus ignore phase. The more exact approach to estimating barrier insertion loss is with wave based methods such as the Boundary Element Method, BEM [3.7, 3.8], and the Finite Element Method, FEM, and in particular the infinite wave envelope method (IFEM) [3.9, 3.10]. Wave based methods solve the governing wave equation and thus model exactly the reflection, diffraction and the phase interferences in the sound field around the barrier. However, wave based methods require excessive computational times with increased geometry dimensions and analysis frequency.

Lam recently introduced an improved diffraction based method that included phase interference [3.6]. Muradali and Fyfe extended this work to include the modeling of two dimensional geometries, the comparison of two and three dimensional mod-

---

[1]A version of this chapter has been submitted to *Applied Acoustics*.

eling, the consideration of parallel barriers and modeling the effect of finite ground impedance [3.11]. Comparisons with the wave based methods demonstrated good agreements, with the diffraction based methods taking only a fraction of the calculation times. The quick calculation times allowed for a series of barrier tests such as frequency sweeps, octave averaging and varying barrier width tests.

Although these techniques for evaluating barrier performance have received wide acceptance, it has been commonly noted that the actual acoustic performance of barriers is different from what is predicted by these modeling tools. This is because all the above mentioned techniques assume a homogeneous, stationary atmosphere. In actuality, the atmosphere consists of wind and temperature gradients, and turbulence, all which affect the sound speed profile. These inhomogeneities greatly affect the way in which the sound energy is transmitted.

Several techniques have been developed to model sound propagation in non-homogeneous medium conditions. These include the Fast Field Program (FFP) [3.12, 3.13] and the Parabolic Equation (PE) [3.14, 3.15, 3.16], to name a few. These techniques can take into account various types of sound speed profiles, and the PE formulations can also model the effects of turbulence [3.17]. However, these techniques are generally restricted to flat ground propagation and only model axisymmetric geometries. Moreover, these models require excessive computational times and a detailed understanding of the controlling parameters to provide results that are representative of the atmospheric conditions being considered.

To counter the problems associated with excessive computational times for modeling atmospheric inhomogeneities, L'Espérance et al. recently developed a model based on geometrical ray theory to predict outdoor sound propagation [3.18]. This model, hereby referred to as the *heuristic model*, assumes a linearly varying sound speed profile which allows an analytical determination of all the possible rays between a source and receiver, and the associated ray parameters. The curvature of the rays is based on Snell's law which states that the direction of the sound ray changes in the

presence of a sound speed gradient [3.18]. For a linear sound speed profile, the resulting sound rays are circular. As the sound speed increases with height (downwind or nighttime conditions), the rays curve back towards the ground. For upwind or daytime conditions, where the sound speed decreases with height, the sound rays curve towards the sky. These rays are depicted in Figure 3.1. The heuristic model handles the two sound speed gradient cases separately. For the downwind conditions (positive sound speed gradient), many rays can appear between a source and a receiver with multiple reflections on the ground [3.19]. For the upwind conditions (negative sound speed gradient), a shadow zone emerges past which the sound pressures are determined using a diffraction theory based on a residue series solution. The heuristic model also includes the effects of ground, atmospheric absorption and turbulence.

Experimental studies have been conducted to study the effects of wind on acoustic barrier performance [3.20, 3.21]. Both studies concluded that the wind does affect the barrier performance and that it is the case for downwind conditions (positive sound speed gradient) that the performance of the barrier is degraded. In a separate study, Daigle investigated the effects of turbulence over top the barriers [3.22]. The overall effect was to scatter some of the sound energy down to the shadow regions close to the barriers thereby reducing the shielding effect of the barrier in these regions. Comparisons with experimental results showed that this was the case especially at higher frequencies.

Salomons recently developed a model, based on geometrical ray theory, to include atmospheric refraction in barrier performance calculations [3.23]. Comparisons with the PE technique, with a thin screen incorporated, showed good agreements [3.24]. This work only included downwind conditions and was considered for long range sound propagation. Moreover, it excludes the rays that undergo multiple reflections off the ground under the notion that these rays are absorbed in the presence of absorbing ground. The only rays considered are the rays that travel from the source to the barrier top and from the barrier top to the receiver. In the presence of absorbing

ground, the curvature due to the refractive profile are included in barrier insertion loss calculations, however, in the presence of a perfectly reflecting ground, these rays are assumed to be straight. Another weakness in this formulation is that, in the presence of a downward refracting atmosphere and at large distances away from the barrier, it is possible to have some sound rays passing over the barrier unattenuated [3.25], the effects of which were not discussed by Salomons.

For this present study, the heuristic atmospheric model is combined with Pierce's diffraction equations for a thin screen [3.26] to provide a more accurate means of barrier insertion loss predictions with the benefit of the trivial calculation times associated with geometrical and diffraction based techniques. The model, hereby referred to as the *combined model*, includes the contributions of the many possible rays with multiple reflections on the ground and also the possible rays that pass over the barrier unattenuated. Also included are the effects of ground absorption, atmospheric absorption and turbulence. In this work, only the case for the positive sound speed gradients (downwind or nighttime conditions) are considered. The results from the combined model are compared to the PE formulation incorporating a thin screen [3.24]. Some preliminary applications of the combined model are also presented.

3.2 Model Descriptions

First, classical barrier modeling in homogeneous atmospheric conditions using the method of Lam [3.6] with Pierce's diffraction model [3.26] will be described. Then a short description of the heuristic model developed by L'Espérance *et al.* [3.18] will be presented for sound propagation in the presence of atmospheric conditions. The combination of the heuristic model with Pierce's diffraction equations for modeling barrier insertion loss in the presence of atmospheric conditions (a linear sound speed profile) will then be described.

70

3.2.1 Classical Barrier Modeling (Homogeneous Atmosphere)

3.2.1.1 The Method of Lam Incorporating Pierce's Equations for Diffraction

For diffraction based methods, the pressure at the receiver is determined by summing the contribution from each diffracted path as it propagates from the source to the receiver. Figures 3.2 and 3.3 illustrate the different diffraction paths around a barrier present in both two dimensional and three dimensional geometries. The pressure due to the diffracted path i is

$$p_i = A_i e^{j\zeta_i} G(kd_i) \tag{3.1}$$

where A_i, ζ_i and d_i are the amplitude change at diffraction, phase shift at diffraction and the path length of the diffracted wave, respectively. The function, G, is the geometric spreading for the source being considered. The total pressure at the receiver is the sum of the individual paths,

$$p_r = \sum_{i=1}^{n} p_i = \sum_{i=1}^{n} A_i e^{j\zeta_i} G(kd_i) \tag{3.2}$$

where n is the total number of paths being considered.

For 2D geometries (Figure 3.2), $n = 4$ and $G = H_0^{(1)}(kd_i)$, which is a Hankel function of the first kind of order zero. It is used to determine the scattering due to a cylindrical source. For the 3D case with a barrier of finite width (Figure 3.3), $n = 8$ and $G = e^{-jkd_i}/d_i$. Note that there are ten possible paths for the 3D geometry, however only eight of which are applicable for any source-receiver configuration. When the receiver is closer to the ground, paths 7 and 8 are replaced with paths 9 and 10 which consider ground reflections on the receiver side.

For the diffraction effects at the barrier edge, Pierce's formulation, which is an approximate solution to the wave equation for the single-edge diffraction by a semi-infinite wedge [3.26], is used. His solution considers cases where the source and receiver are at large distances from the barrier in terms of wavelength. Figure 3.4 shows the geometry considered. Diffraction due to a semi-infinite thin screen is a special case where the angle β is equal to 2π.

Pierce's equations for barrier edge effects reduce down to the following for both 2D and 3D geometries:

$$A_i e^{j\zeta_i} = [A_D(X_+) + A_D(X_-)]\left(\frac{e^{j\frac{\pi}{4}}}{\sqrt{2}}\right)$$ (3.3)

where

$$A_D(X) = sign(X)[f(|X|) - jg(|X|)]$$

$$X_+ = X(\theta + \theta_o)$$

$$X_- = X(\theta - \theta_o)$$

$$X(\theta) = \left[\frac{2r_o r}{\lambda d_i}\right]^{\frac{1}{2}}[-2\cos\left(\frac{\theta}{2}\right)]$$

$$d_i = r_o + r$$

In the above equations, f and g are series representations for the Fresnel integral functions, and A_D is the Airy function. From this point forward $A_i e^{j\zeta_i}$ will be denoted as the coefficient for diffraction, C_d.

3.2.2 Barrier Modeling Including Atmospheric Effects

3.2.2.1 The Heuristic Model

The heuristic model described below assumes a linear sound speed profile which permits an analytical determination of all the rays (and the associated parameters) between source and receiver location on a flat, infinite half-space [3.18]. The discussion below is intended to supplement the heuristic model description offered in L'Espérance et al.'s respective publication.

Sound Speed Profile   Under typical conditions, the air temperature and wind vary with height, and thus so does the effective sound speed. The heuristic model assumes a linear relationship between the speed of sound, c, and height, y, in the form

$$c(y) = c_g(1 + ay)$$ (3.4)

72

where c_g is the speed of sound on the ground in m/s, and a is referred to as the sound speed gradient, which has the units of m^{-1}. For barrier performance predictions, the sound rays curving towards the ground are of particular interest, as earlier discussed. This occurs when $a > 0$.

The following table associates common atmospheric conditions with some values of a. Positive values of a refer to nighttime conditions, whereas negative values refer to daytime conditions.

a (m^{-1})	Common atmospheric conditions
0.00001	Cloudy conditions, no wind.
0.0001	Calm, semi-cloudy, light breeze conditions.
0.001	Strong inversion, clear skies, breezy conditions.
0.01	Strong winds.

Table 3.1: Common atmospheric conditions associated with sound speed gradients.

Sound Rays in the Presence of a Positive Gradient   Under a positive gradient, more than 2 rays may appear between a source and a receiver as shown in Figure 3.5. The following 4th order equation has been shown to determine all of these rays,

$$n(n+1)x^4-(2n+1)Dx^3+[b_r^2+(2n^2-1)b_s^2+D^2]x^2-(2n-1)b_s^2Dx+n(n-1)b_s^4 = 0 \quad (3.5)$$

where $b_i^2 = (2 + ay_i)(y_i/a)$ for $i = s$ (source) and r (receiver), and $n = 1, 2, 3, ...$ is the number of reflections on the ground [3.19].

This equation determines the locations, x, of the first reflection for rays that undergo n reflections on the ground. Since this is a fourth order equation, it is possible to get up to 4 rays for each $n \geq 2$. For $n = 0$ (i.e. no reflections on the ground) there is only one ray that appears, that is from the source to the receiver, and is always present. For each additional n, all of the real roots pertain to the valid rays

73

between the source and receiver. This equation must be solved for all n until there are no real roots (or until the appearance of complex conjugate roots). Figure 3.6 shows these x locations for rays with 1 and 2 ground reflections. Figure 3.6(a) is for $n = 1$ (i.e. each ray having single ground reflection). The x locations for the first reflections, as determined by Equation 3.5, are x_1 and x_2 for both of the rays shown. Note that only 2 rays are shown for $n = 1$, however it is possible to obtain up to 3 rays for the case of single ground reflection. Figure 3.6(b) shows two rays undergoing 2 ground reflections ($n = 2$), with x_1 and x_2 being the locations of first reflections. However, for this and higher values of n, it is possible to obtain up to 4 rays.

To demonstrate the stages for determining the ray parameters, consider the case shown in Figure 3.7. This is the case for $n = 1$ (each ray having one reflection on the ground). For this case the 4th order equation contained two real roots for the source-receiver geometry and the gradient being considered. Thus there are two rays that appear for $n = 1$, with the locations of the first reflection being D_{s_1} and D_{s_2}.

The ray parameters needed for further calculations are the length of the ray, R_{ray}, the angle of incidence to the ground, ψ_g, and the time of travel from the source to the receiver, τ_{ray}. These parameters are determined with the help of the following equations,

$$R(y_r) = \frac{1}{a\cos(\psi_g)}\left[\sin^{-1}\{(1 + ay_r)\cos(\psi_g)\} - \frac{\pi}{2} + \psi_g\right] \tag{3.6}$$

$$\tau(y_r) = \frac{1}{2ac_g}\ln\left[\frac{f(0)}{f(y_r)}\right] \tag{3.7}$$

where

$$f(y) = \frac{1 + \sqrt{1 - (1 + ay)^2\cos^2(\psi_g)}}{1 - \sqrt{1 - (1 + ay)^2\cos^2(\psi_g)}} \tag{3.8}$$

and

$$\tan(\psi_g) = \frac{aD}{2} + \frac{y_r(2 + ay_r)}{2D} \tag{3.9}$$

These equations pertain to Figure 3.8 where the source is on the ground and the receiver is at a height of y_r. Note that the ray is curved, however it has not passed

74

the point of maximum height. When the receiver happens to be at the location of maximum height for the ray, y_m, the following equations apply,

$$R(y_m) = \frac{\psi_g}{a\cos(\psi_g)} \qquad (3.10)$$

$$\tau(y_m) = \frac{1}{2ac_g}\ln\left[\frac{1+\sin(\psi_g)}{1-\sin(\psi_g)}\right] \qquad (3.11)$$

$$y_m = \frac{1}{a}\left(\frac{1}{\cos(\psi_g)} - 1\right) \qquad (3.12)$$

$$D_m = \frac{\tan(\psi_g)}{a} \qquad (3.13)$$

The length and travel time of the rays with multitude of reflections on the ground can be determined by simple additions and deductions using the above equations. Consider again the case shown in Figure 3.7. The ray lengths and travel times for both of the rays are determined using the results from Equations 3.6-3.13 in the following form:

$$R_{ray1} = R(y_s) + 2R(y_{m1}) - R(y_r) \qquad (3.14)$$

$$\tau_{ray1} = \tau(y_s) + 2\tau(y_{m1}) - \tau(y_r) \qquad (3.15)$$

$$R_{ray2} = 2R(y_{m2}) - R(y_s) + R(y_r) \qquad (3.16)$$

$$\tau_{ray2} = 2\tau(y_{m2}) - \tau(y_s) + \tau(y_r) \qquad (3.17)$$

Note that the component of ray #1 going from the ground to the receiver passes its maximum point. Thus, the latter part of Equations 3.14 and 3.15 is a correction for this length. The same can be said for ray #2, except now for the component going from the source to the ground.

In general, the parameters for a ray undergoing n reflections can be determined using the following expressions:

$$R_{ray} = 2(n-1)R(y_m) + R(y_s) + R(y_r) \qquad (3.18)$$

$$\tau_{ray} = 2(n-1)\tau(y_m) + \tau(y_s) + \tau(y_r) \qquad (3.19)$$

75

Note that $R(y_s)$, $R(y_r)$, $\tau(y_s)$, and $\tau(y_r)$ should be corrected if the maximum height has been passed $(D > D_m)$.

Once the parameters for all rays between the source and the receiver have been determined, the pressure at the receiver can be determined by the following expression:

$$p_r^2 = \sum_{i=1}^{N} \frac{A(R_{ray_i})^2|Q_i|^2}{R_{ray_i}^2} +$$
$$2\sum_{i=2}^{N}\sum_{j=1}^{i-1} \frac{A(R_{ray_i})A(R_{ray_j})|Q_i||Q_j|}{R_{ray_i}R_{ray_j}} \cos\left[2\pi f(\tau_j - \tau_i) + Arg\left(\frac{Q_j}{Q_i}\right)\right] (3.20)$$

where $A(R_{ray})$ is the atmospheric absorption coefficient and Q is the spherical wave reflection coefficient determined as shown in the Appendices. It is important to note that the phase interference between the rays is determined using the frequency and the travel times instead of the wave number and the length of the rays, because the wave number changes with height in the presence of a varying sound speed profile.

3.2.2.2 Applications of Pierce's Equations in Non-Homogeneous Medium

Pierce's formulations described earlier are for homogeneous medium conditions. In the presence of a varying sound speed profile, the wavelength changes with height. This affects the equation for $X(\theta)$ in Equation 3.3, and is thus modified to,

$$X(\theta) = \left[\frac{2\tau_o\tau f}{\Upsilon}\right]^{\frac{1}{2}} \left[-2\cos\left(\frac{\theta}{2}\right)\right] \tag{3.21}$$
$$\Upsilon = \tau_o + \tau$$

where τ_o is the travel time from the source to the barrier top, τ is the travel time from the barrier top to the receiver, and f is the frequency of the spherical source.

To demonstrate the applications of Pierce's equations for non-homogeneous medium conditions, consider a single ray going from the source to the receiver, via a barrier edge as shown in Figure 3.9. The ray parameters are determined by considering the barrier top both as a source and a receiver. With the heuristic model, the length

76

of the rays on either side of the barrier, as well as the associated travel-times are determined, and the parameters for the single ray going from the source to receiver are given by

$$R_{ray} = R_{ray_1} + R_{ray_2} \tag{3.22}$$

$$\Upsilon_{ray} = \tau_{ray_1} + \tau_{ray_2} \tag{3.23}$$

$$Q = Q_1 Q_2 \tag{3.24}$$

However, to determine the coefficient for diffraction, C_d, from Pierce's equations, the angles incident on the barrier top are required. Expressions for these angles are not given in the heuristic model, but with some geometrical manipulations, the following expression can be shown to determine these angles relative to the horizon,

$$\cos(\psi_d) = \cos(\psi_g)(1 + ay_r) \tag{3.25}$$

Figure 3.10 shows this angle. Note that a minor correction to the angle would be necessary in the event the ray passes its maximum height ($D > D_m$). In addition, ψ_d, for any ray incident upon the barrier top must be adjusted to the angles θ and θ_o for input into Pierce's equations depending on what side of the barrier the ray exists.

The coefficient for diffraction for the single ray in Figure 3.8 is then determined by

$$C_d = Pierce(R_{ray}, \Upsilon_{ray}, \tau_{ray_1}, \tau_{ray_2}, f, \theta, \theta_o) \tag{3.26}$$

where the parameters in the brackets are used in Pierce's equations.

3.2.2.3   The Combined Model

When considering all of the rays between a source and receiver separated by a barrier, numerous rays can appear and disappear depending on geometry and the sound speed gradient. The case shown in Figure 3.11, a point source in front of an infinitely wide barrier, is that for $a = 0.1$, from the sound speed - height relationship given in Equation 3.4. The heuristic model determined 2 rays between the source and the

barrier top, and 4 rays between the barrier top and the receiver. Thus the total number of rays that diffract off the barrier is 8. The parameters associated with these 8 rays are determined as shown in the previous section.

In addition, all the rays between the source and the receiver that pass over the barrier must also be considered. For the case shown in Figure 3.11, there are 5 such rays. Since these rays are not attenuated by diffracting off the barrier top, the diffraction coefficient for these rays are assigned the value of 1 ($C_d = 1 + j0$). However, it should be noted that this may not be the case for some of these rays as they may pass close to the barrier edge and, as a result, be diffracted down to the shadow region. This effect has not been included in the current combined model.

Once the parameters for all the rays are determined, the pressure at the receiver point can be determined by the following equation:

$$
\begin{aligned}
p_r^2 &= \sum_{i=1}^{N} \left(\frac{A(R_{ray_i})|Q_i||C_{d_i}|}{R_{ray_i}} \right)^2 + \\
&\quad 2 \sum_{i=2}^{N} \sum_{j=1}^{i-1} \frac{A(R_{ray_i}) A(R_{ray_j})|Q_i||Q_j||C_{d_i}||C_{d_j}|}{R_{ray_i} R_{ray_j}} * \\
&\quad \cos \left[2\pi f(\tau_j - \tau_i) + Arg\left(\frac{Q_j}{Q_i}\right) + Arg\left(\frac{C_{d_j}}{C_{d_i}}\right) \right]
\end{aligned}
\tag{3.27}
$$

where $N = 13$ for the case shown in Figure 3.11.

3.2.2.4   Modeling the effects of turbulence

The atmosphere is neither homogeneous nor is it associated with a single sound speed gradient throughout the entire travel of any particular ray. Several inhomogeneities occur in the atmosphere within any time period. As air moves past vegetation, or as small pockets of air rise and descend, atmospheric turbules are generated which cause fluctuations in the wind velocity gradients. Fluctuations in the temperature gradients can be caused, for example, by the intermittent heating of the ground by the sun in the presence of a band of moving clouds. Such conditions result in a sound speed gradient that fluctuates with time.

In a recent study by L'Espérance *et al.*, the effects of atmospheric turbulence were modelled using the Fast Field Program by conducting a weighted average of the sound pressures due to the instantaneous sound speed profiles measured within a specified time period [3.27]. The results compared well with field measurements made under the same atmospheric conditions.

For this study, the effects of turbulence were modelled along the same lines as L'Espérance *et al.* The sound pressures due to single linear profiles within a specified range, as shown in Figure 3.12, were averaged as shown by the following expression

$$p_{ave}^2 = \frac{\sum_{i=1}^{m} p_i^2}{m} \tag{3.28}$$

where p_i^2 is the pressure-squared due to the *i*th profile, of a total of m profiles considered.

3.3 Results

3.3.1 Preliminaries

The proposed model is first compared with the Parabolic Equation (PE) formulation incorporating a thin screen [3.24]. The controlling parameters used for this study are the same as those used by Salomons for the 100 and 1000 Hz cases. It should be noted that the results in the illumination region are not accurate as both the PE and the combined model do not account for reflections off the barrier. However, it is the results in the shadow region that are of most interest.

The results for the model verification are shown as relative sound pressure levels. This is the sound pressure relative to free field geometrical spreading. All other results are shown as insertion losses (IL).

For computations, the speed of sound at the ground, c_g, was assigned the value of 343 m/s. For ground properties, hard ground was assigned an effective flow resistivity value of 10,000 cgs Rayls, and soft ground was assigned a value of 300 cgs Rayls [3.28].

79

3.3.2 Model Verification

3.3.2.1 The Heuristic Model Verification and Observations

Figure 3.13 shows the PE model and the heuristic model results at 100 Hz for the source and receiver, both at a height of 2 m, above rigid ground. This figure demonstrates the true nature of the heuristic model. The PE levels increase continuously and the heuristic model levels exhibits step changes. The locations of these step changes indicate that additional rays appear, as determined by Equation 3.5. However, it is observed that the heuristic model approximates the PE solution.

The case for soft ground for the same conditions as in the previous figure, is shown in Figure 3.14. Here, it is noted that the rays that appeared at about 220 m and 250 m do not contribute greatly to the sound field as they are absorbed due to multiple reflections on the soft ground.

Figure 3.15 shows the results at 1000 Hz for a source and receiver above soft ground. Once again, the source and receiver are 2 m above the ground. The results for both techniques agree well. Additional rays do not appear for the range considered. However, the results are different than the case for still air and this can be attributed to the curvature of the rays.

3.3.2.2 The Combined Model Verification

Figure 3.16 shows results with a barrier, at 100 Hz above soft ground for the same source and receiver heights as the previous figures. The barrier is 4 m high and 30 m away from the source. Additional rays appear at about 160 m and 260 m that result in the step changes at these locations. However, it is observed that the combined model results, once again, approximate the PE results. The spurious oscillations in the PE results originate from the numerical integration used in the calculational procedure [3.24].

Figure 3.17 shows the case at 1000 Hz for the same source-barrier-receiver geom-

etry as in Figure 3.16. Again, good agreement between the two models is observed.

3.3.3 Applications

Figure 3.18 shows insertion loss (IL) vs. receiver position for 2 gradients, namely the strong ($a = 0.01$) and moderate ($a = 0.0001$) gradients at 500 Hz. Also shown are results that for an averaged gradient field and the homogeneous case. The source is 0.5 m above the rigid ground and 10 m away from the 3 m high rigid barrier. The receiver positions are 1.5 m above ground and extend up to 300 m away from the barrier. It is observed that the results vary wildly when considering only a single gradient. However, due to turbulence and local deviations, the atmospheric sound speed gradient changes constantly, and as such, averaged results over a range of sound speed profiles better depict reality. The averaged results, hereby designated as the *turbulent condition*, for this and all of the subsequent figures, were conducted linearly over 10 sound speed profiles ranging from a strong gradient ($a = 0.01$) to a moderate gradient ($a = 0.0001$).

Figure 3.19 shows the same test case as the previous figure, except now the turbulent and homogeneous conditions are compared for both hard and soft ground at 500 Hz. First, it is observed that the insertion loss is lower for the soft ground case as the soft ground itself already contributes a great deal to the sound absorption. Secondly it is seen that for either case, the barrier insertion loss greatly deteriorates after about 75 m. After this distance, the rays that *walk over* the barrier, negate most of the barrier shielding. Figure 3.20 shows the same turbulent test cases, except now a frequency average is performed between 100 and 2000 Hz instead of just a single frequency. Similar responses are observed.

Figures 3.21 and 3.22 show the frequency response at 2 receiver locations for the same source - barrier geometry as in the previous figures. The receiver locations are 50 m (Figure 3.21) and 100 m (Figure 3.22) away from the barrier. Shown are the homogeneous and turbulent cases for both hard and soft ground. A relatively flat

response is observed for the turbulent conditions as compared to the homogeneous conditions.

The applications shown up to this point have considered a single barrier height of 3 m. Figure 3.23 demonstrates the effect of the varying the barrier height. Shown are the frequency averaged insertion losses, for both homogeneous and turbulent conditions, as a function of barrier height at three receiver locations; 50 m, 100 m and 150 m away from the barrier. The source is 0.5 m above the rigid ground and 10 m away from the barrier. The results are weighted frequency averages for both homogeneous and turbulent conditions. The first thing to note is that the top three curves are very nearly coincident. This implies that there is no significant distinction between the homogeneous solutions at the three receiver positions. However it is observed that when considering atmospheric effects the insertion losses decrease as the receiver moves away from the barrier. This is consistent with the response shown in Figure 3.20.

In 1971, Scholes *et al.* conducted some field measurements to study the effect of wind on barrier performance [3.20]. The experimental conditions were not well documented to permit valid comparisons with the combined model. As such, educated guesses were made for the parameters needed for computations with the combined model. The ground, which was grass covered, was assigned an EFR value of 150 cgs Rayls (based on the impedance dip characteristic provided with the experimental results) and the temperature near the ground was assumed to be room temperature (i.e. $c_g = 343$ m/s). Shown in Figure 3.24 is the data collected for downwind conditions on a 4.9 m high barrier and the results computed using the combined model. Good agreements are observed.

3.4 Summary and Conclusions

A major limitation of conventional wave based and diffraction based techniques is that both formulations assume homogeneous atmospheric conditions. As a result, the

acoustic performance of barriers is usually overpredicted. For this study, a heuristic model based on the geometrical ray theory, and Pierce's equations for diffraction, are combined to introduce the atmospheric element in barrier performance prediction with the benefit of quick calculation times associated with geometric and diffraction based models. The model accounts for the various rays that diffract off the top of the barrier and those rays that simply *walk over* the barrier in the presence of a linearly varying sound speed profile. Comparisons with the Parabolic Equation (PE) formulations have shown good agreements for receivers in the short to medium range of sound propagation in the shadow of a barrier.

Calculations made with just a single sound speed gradient, however, do not adequately model actual atmosphere conditions as the gradient at any location changes with time due to atmospheric turbulence. Thus the sound pressures for sound speed gradients ranging from moderate to strong were averaged to better depict reality.

From tests that were conducted in this work, it was observed that, past a certain distance, the shielding effect of the barrier was greatly reduced (or nearly eliminated), in downwind conditions, due to rays that walk over the barrier. It was also seen that the averaged gradient, or turbulent, results showed a relatively flat frequency response as compared to the homogeneous results. Finally, good agreements were observed in the preliminary comparisons with the experimental data collected by Scholes *et al.*

3.5   Future work

The good agreement observed in the preliminary comparisons with experimental data shows promise for the combined model in modeling the atmospheric conditions with barrier calculations. However, the modeling technique needs further validation with experimental measurements made under well documented conditions. This will help judge the usefulness of a linear sound speed profile in short and medium range barrier studies. To take into account longer range sound propagation studies, an improved sound speed profile model will need to be developed. This might include a more

83

realistic logarithmic profile and a profile that might change from source to receiver.

Other improvements include the modeling of upwind conditions (negative sound speed gradient) and the diffraction of the rays that pass over, but close, to the barrier. As well, the work to date has only considered the resulting pressure field in the shadow zone of the barrier; work should be carried out to consider the reflections off the barrier, for bright region considerations.

3.6 Acknowledgments
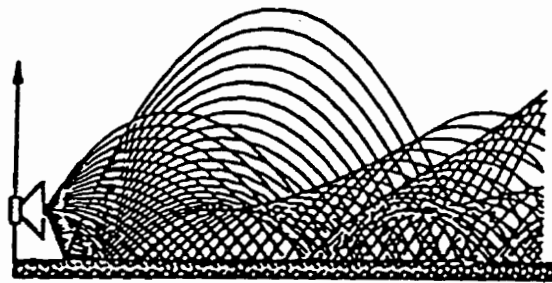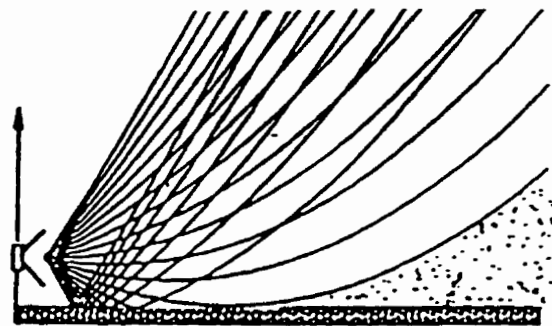
Figure 3.1: Sound rays present in typical atmospheric conditions [3.25].
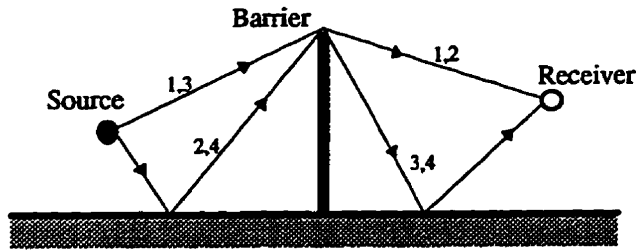
Figure 3.2: Diffraction paths for a 2D barrier geometry.
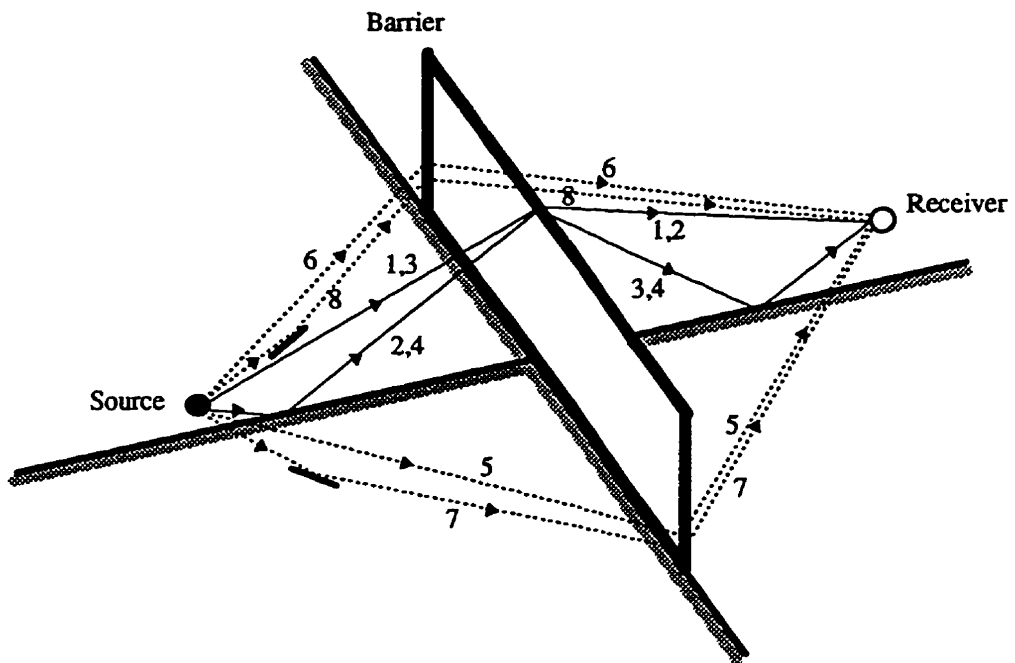
Figure 3.3: Diffraction paths for a 3D finite length barrier geometry.
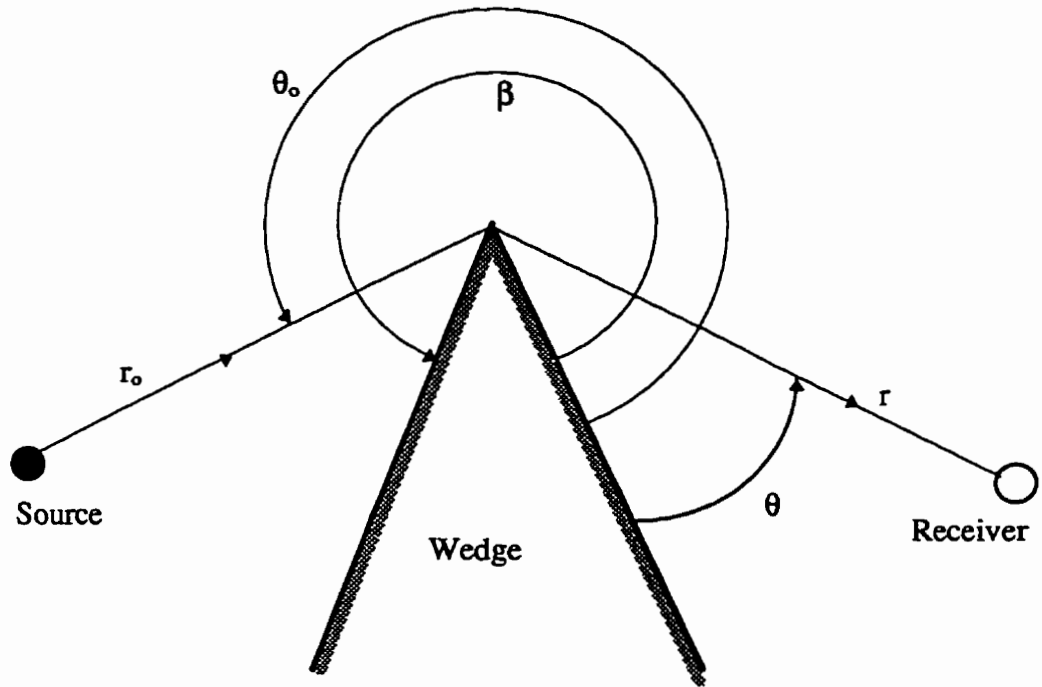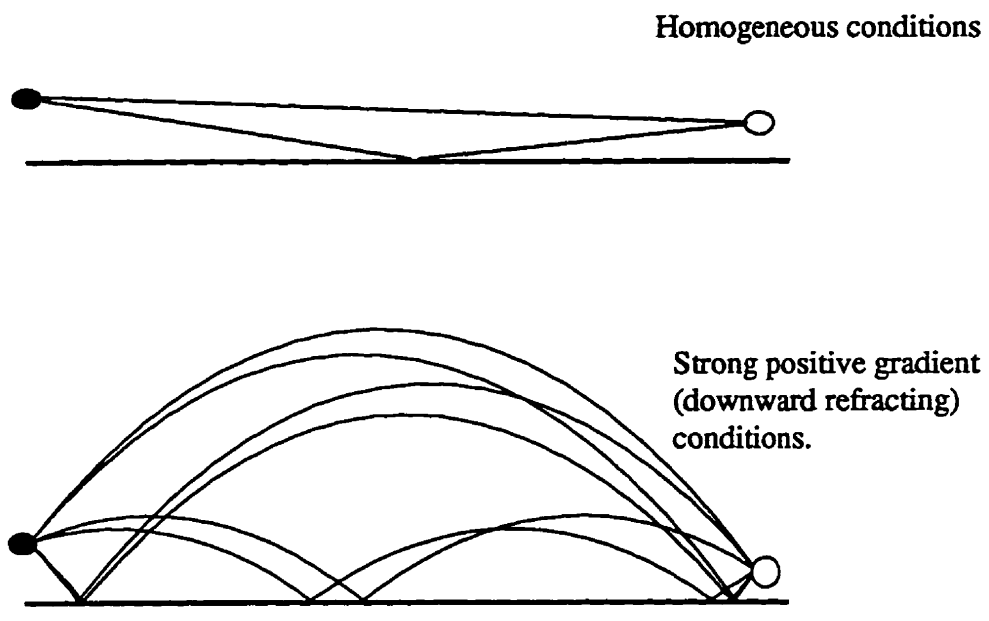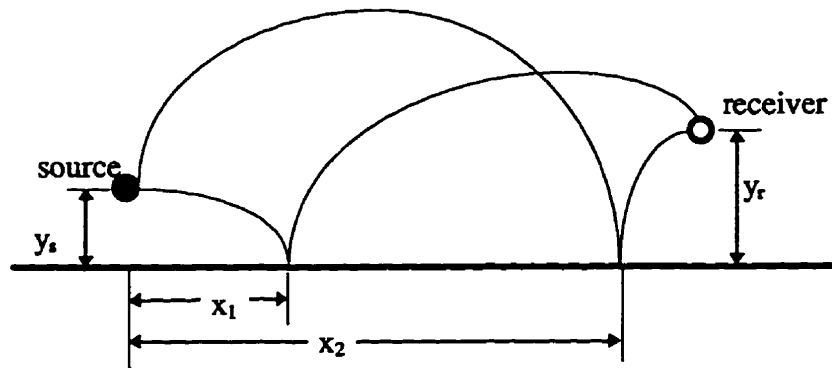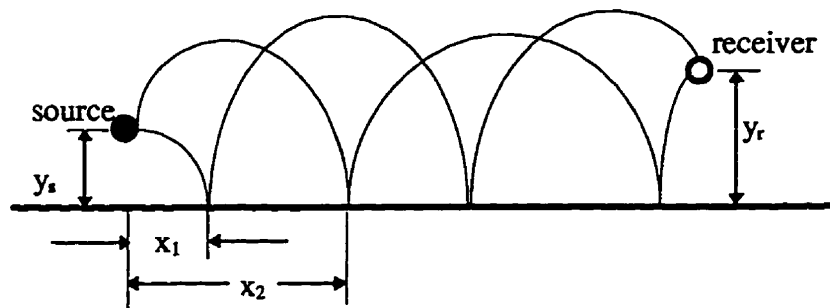
86

Figure 3.4: Semi-infinite wedge diffraction for Pierce's diffraction model.

Homogeneous conditions

Strong positive gradient
(downward refracting)
conditions.

Figure 3.5: Sound rays between a source and a receiver present in homogeneous and strong positive gradient conditions.

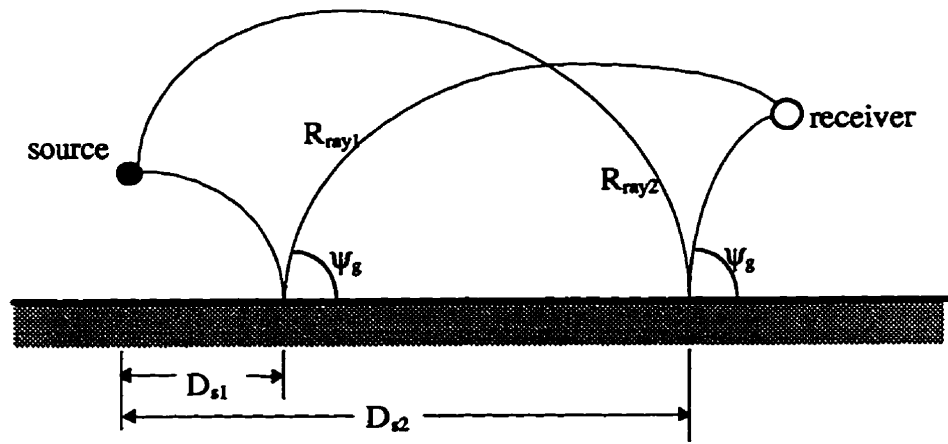**Figure 3.6:** Locations of first reflections for sound rays with single(a) and double(b) ground reflections.
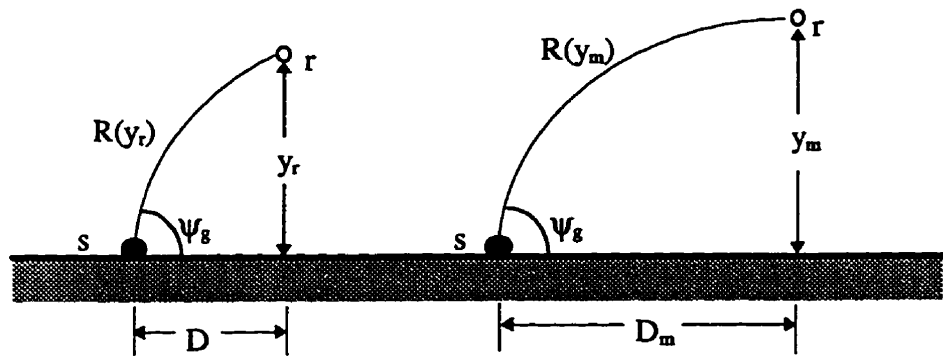
Figure 3.7: Geometrical parameters of curved sound rays.
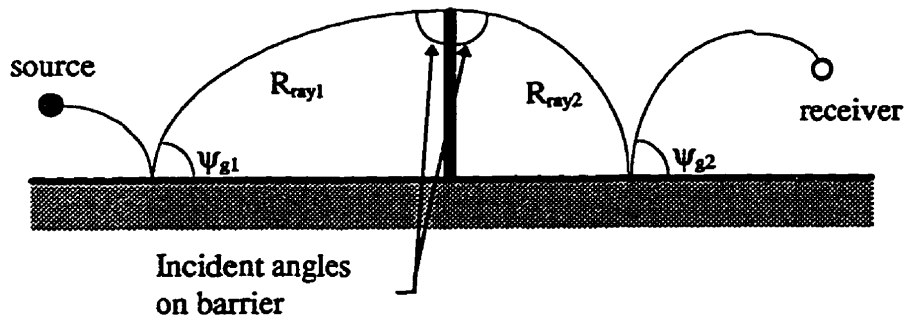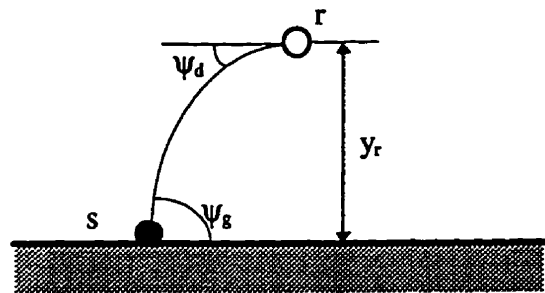

Figure 3.8: Figure pertaining to Equations 3.6 - 3.13.

90

Figure 3.9: Single ray going from source to receiver, via the barrier top.

Figure 3.10: The angle, ψ_d, needed for diffraction coefficient calculations.
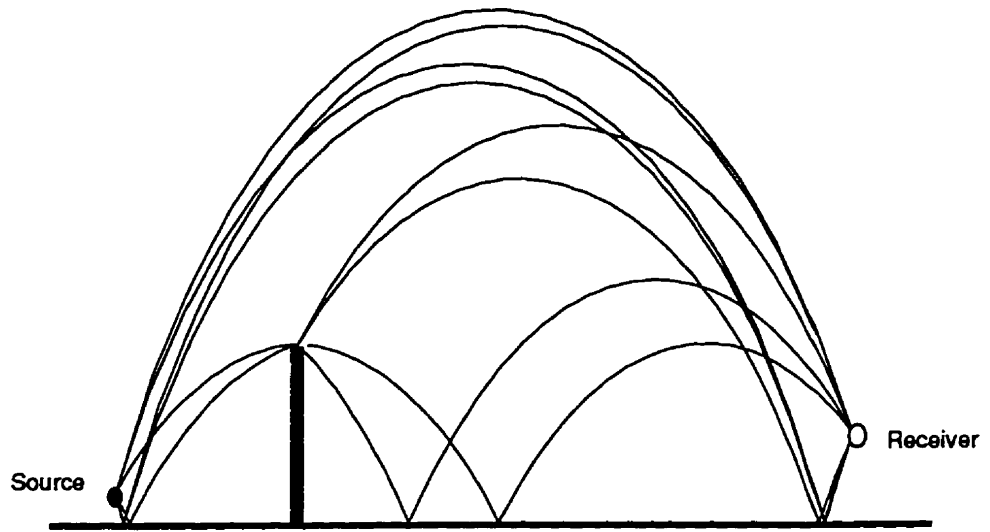
Figure 3.11: Example of sound rays in strong gradient conditions passing and diffracting over the barrier top.
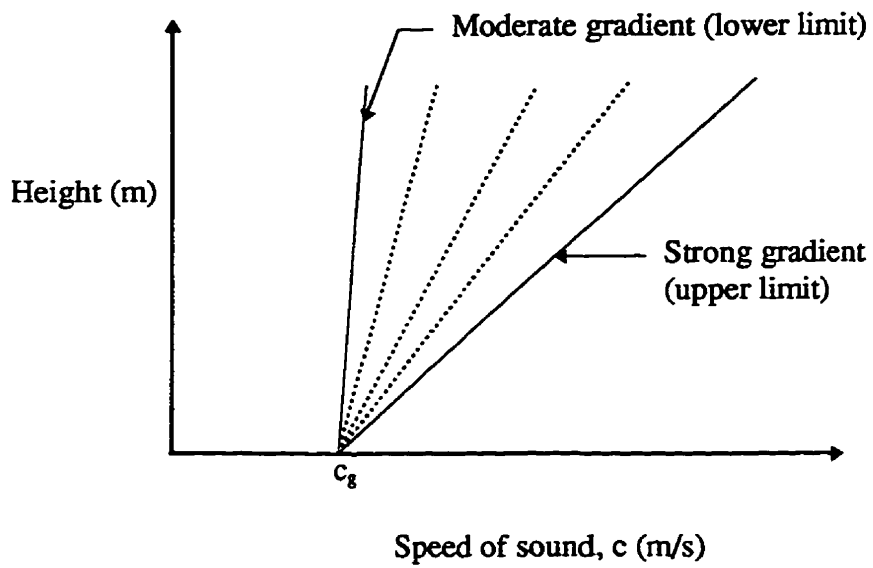
Figure 3.12: Individual profiles, and range, averaged for modeling the effects of turbulence.
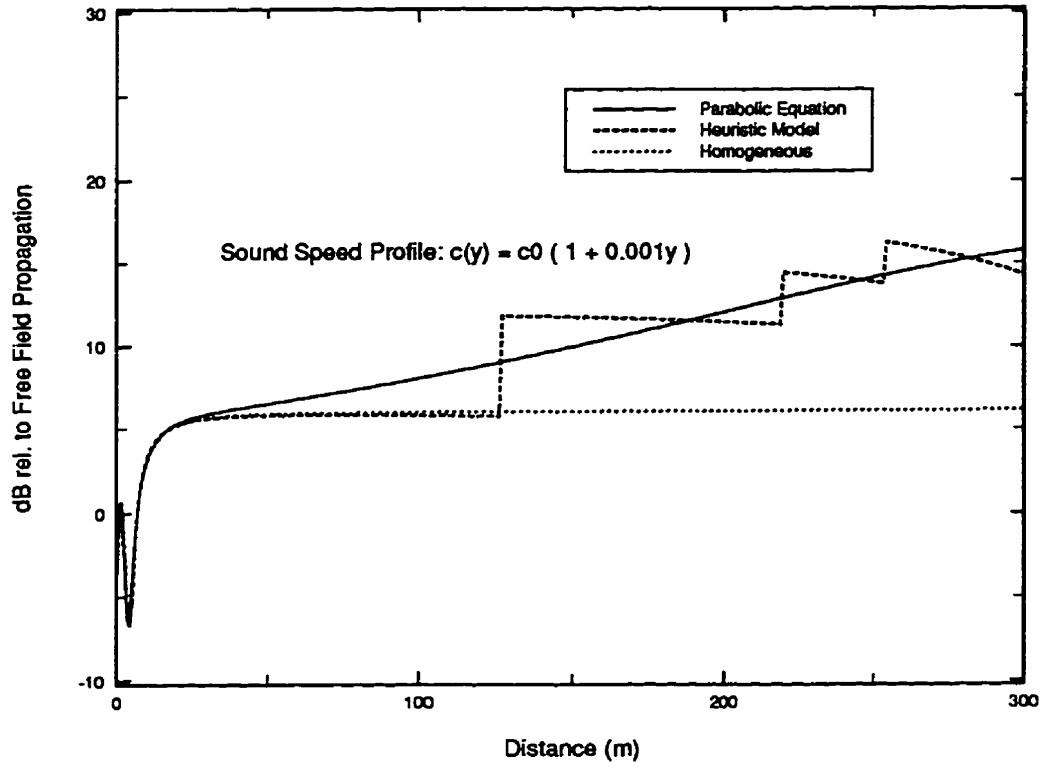
Figure 3.13: Comparisons with PE at 100 Hz; no barrier and over hard ground.
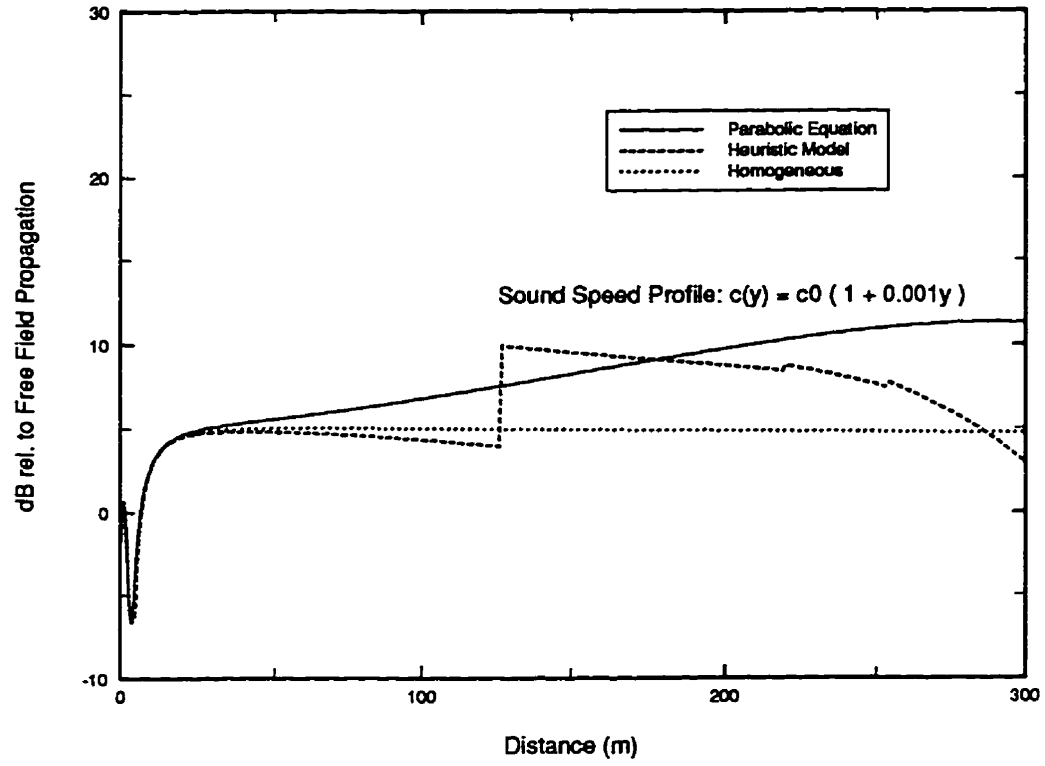
Figure 3.14: Comparisons with PE at 100 Hz; no barrier and over soft ground.
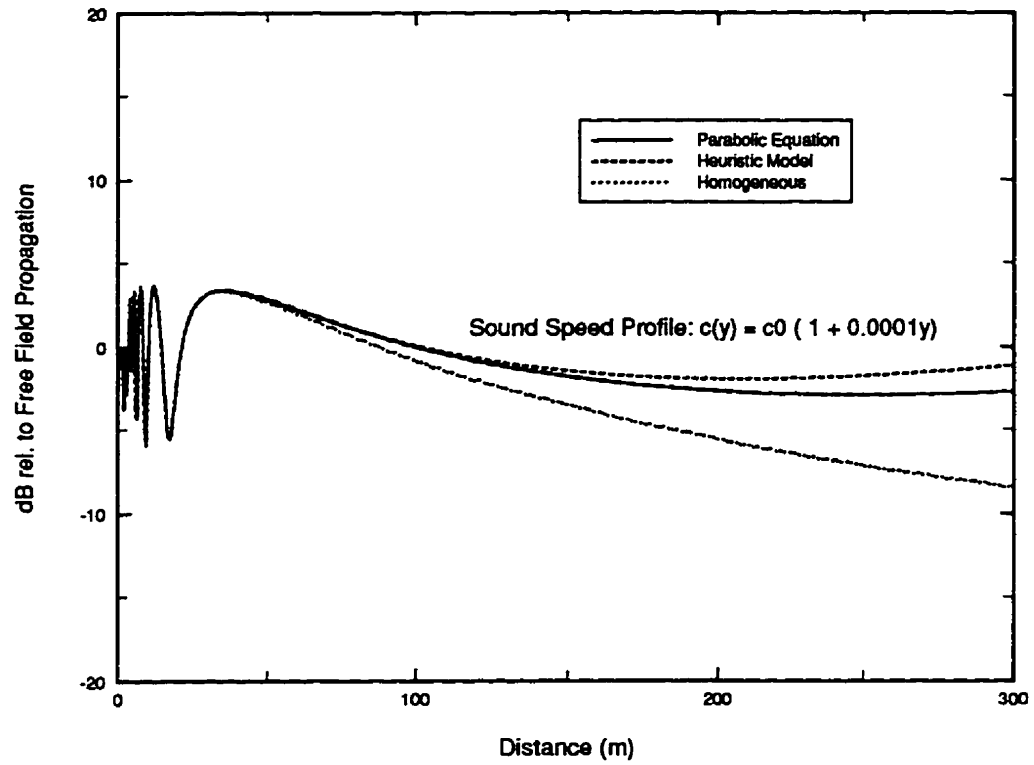
Figure 3.15: Comparisons with PE at 1000 Hz; no barrier and over soft ground.
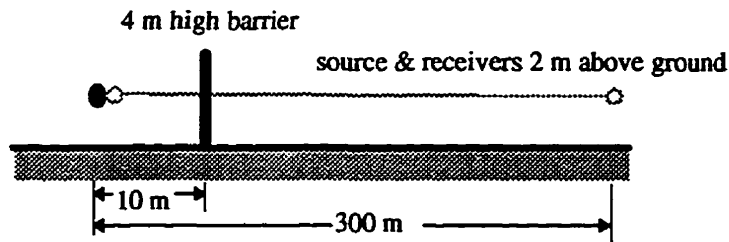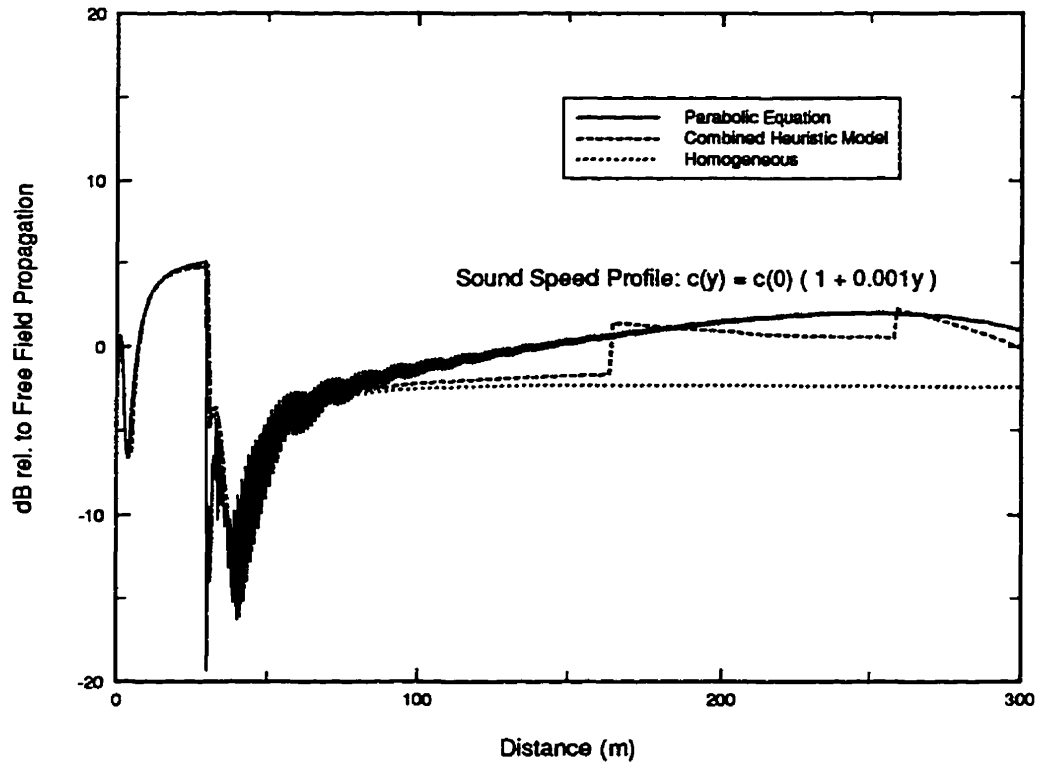
Figure 3.16: Comparisons with PE at 100 Hz; with barrier and over soft ground.
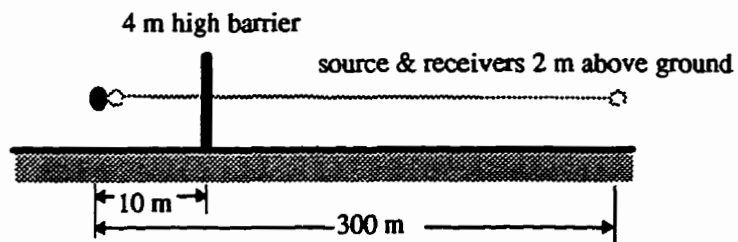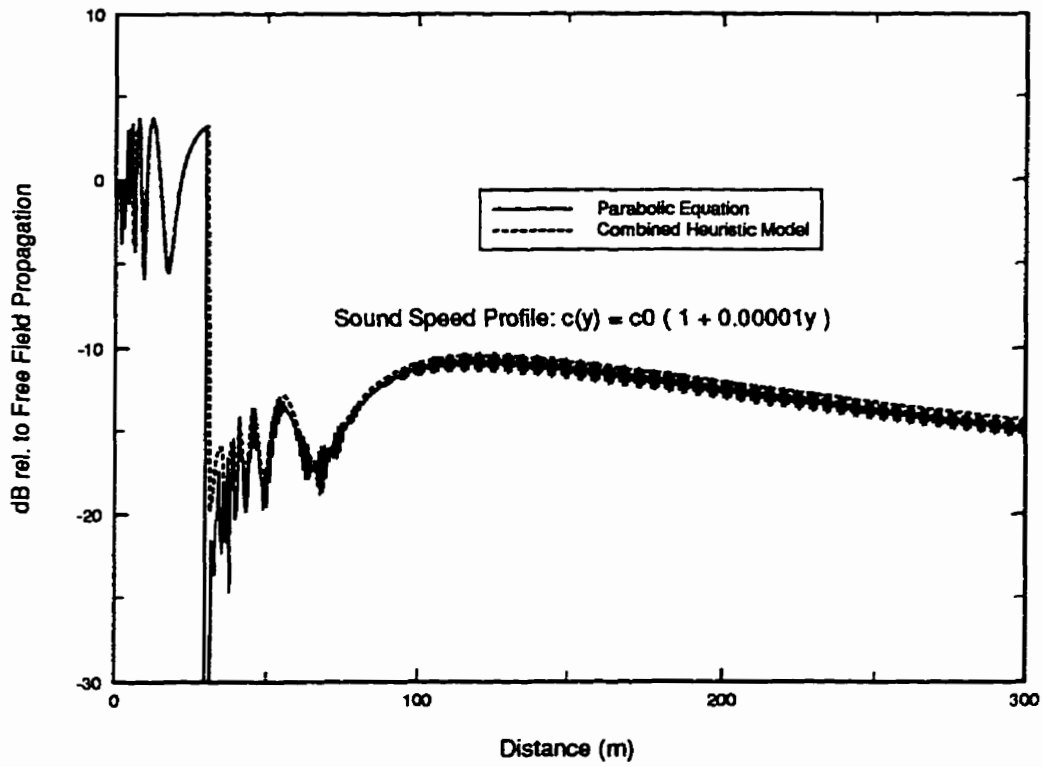
Figure 3.17: Comparisons with PE at 1000 Hz; with barrier and over soft ground.
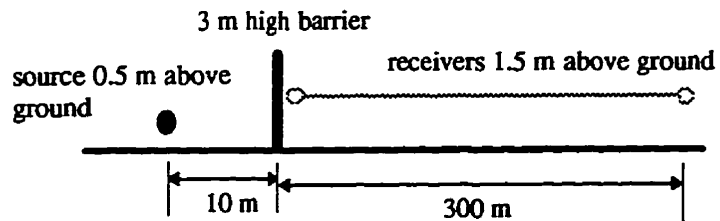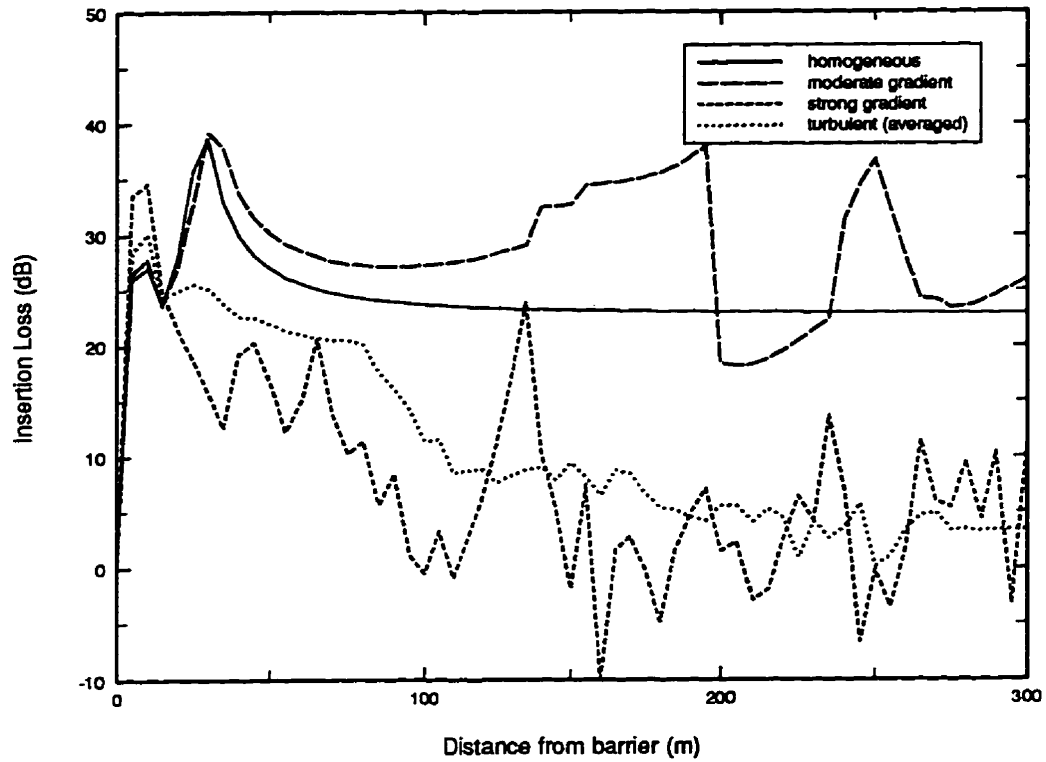
Figure 3.18: Insertion loss as a function of receiver position for single gradients and an averaged gradient field.
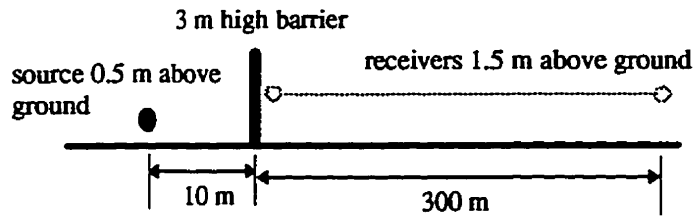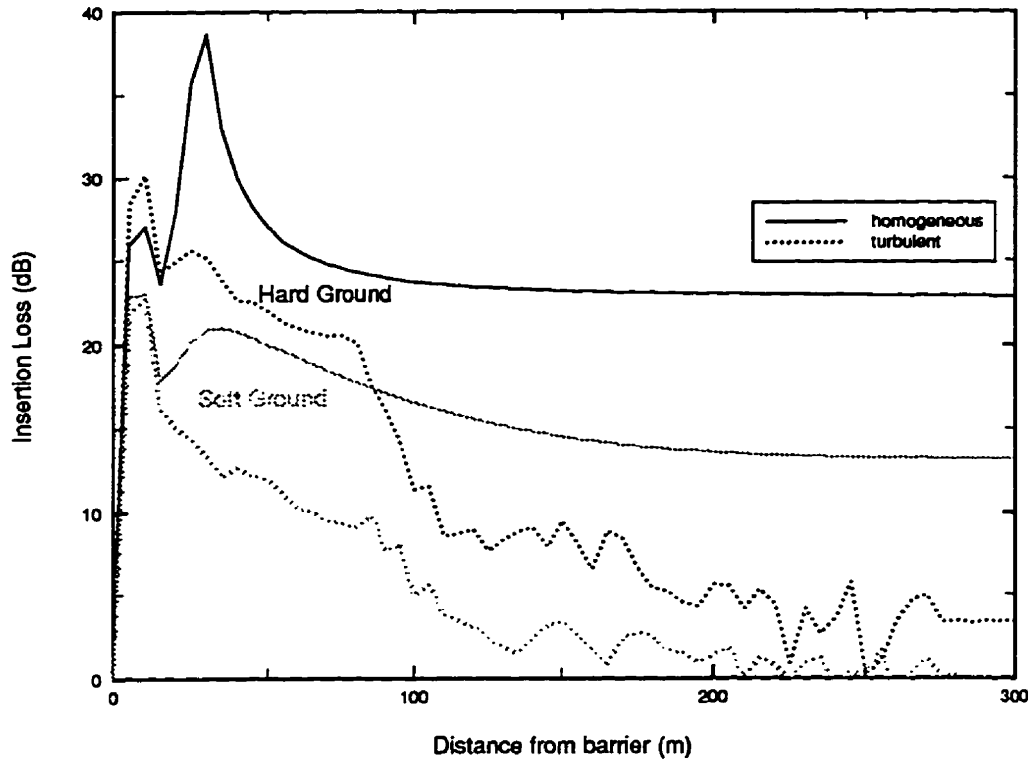
Figure 3.19: Insertion loss as a function of receiver position for hard and soft ground at 500 Hz.
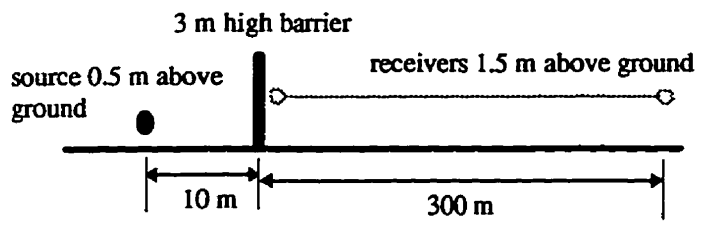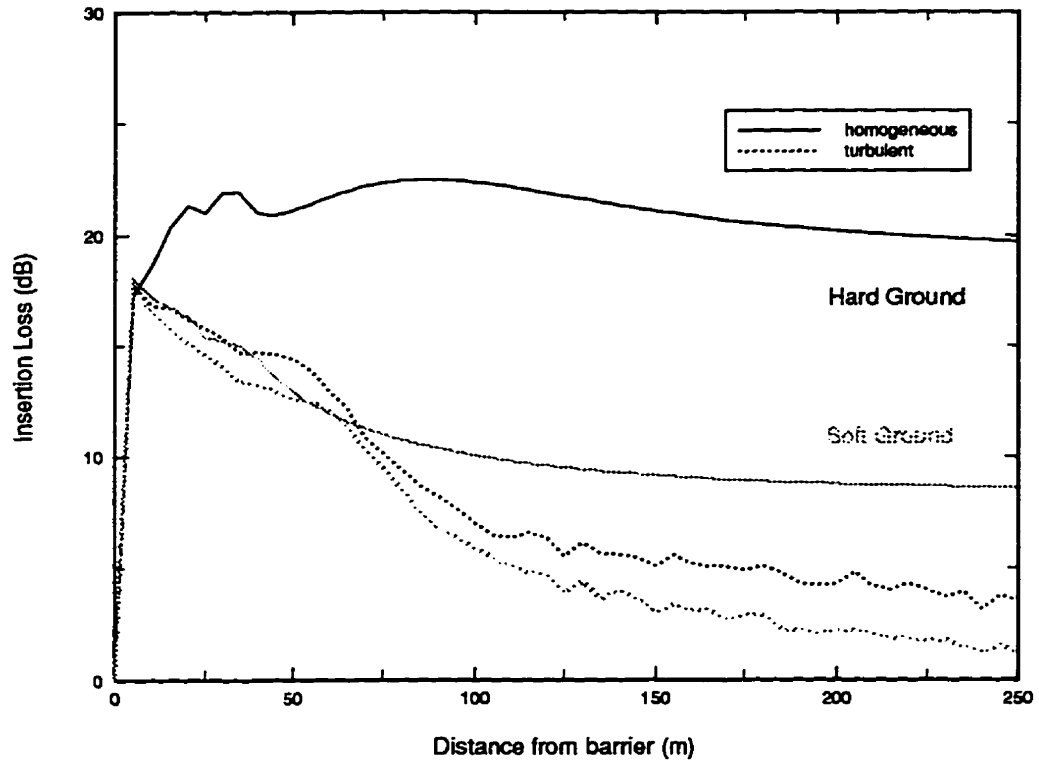
Figure 3.20: Averaged results between 100 - 2000 Hz.
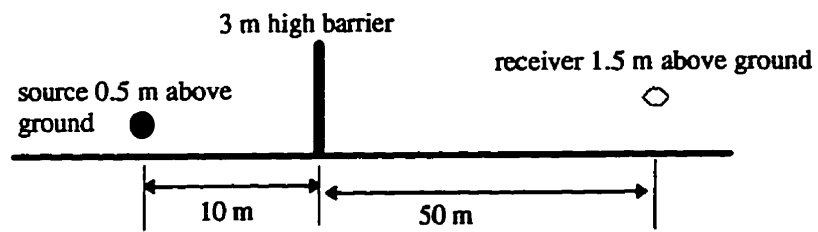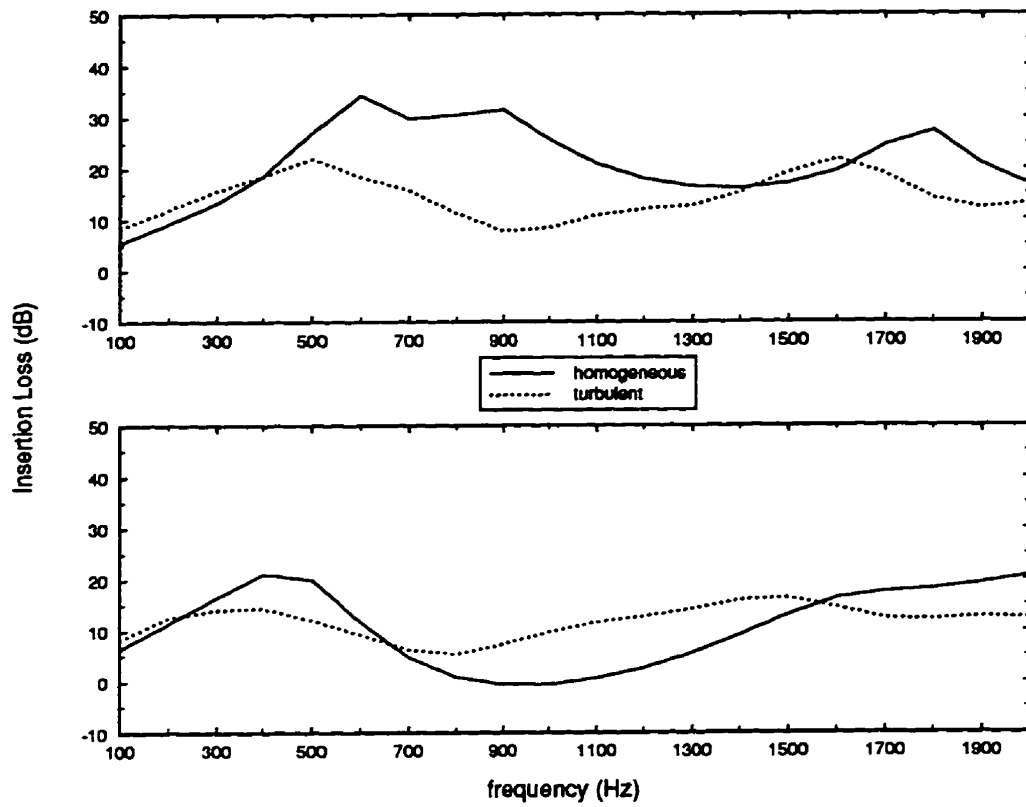
Figure 3.21: Frequency response at receiver 50 m away from barrier.
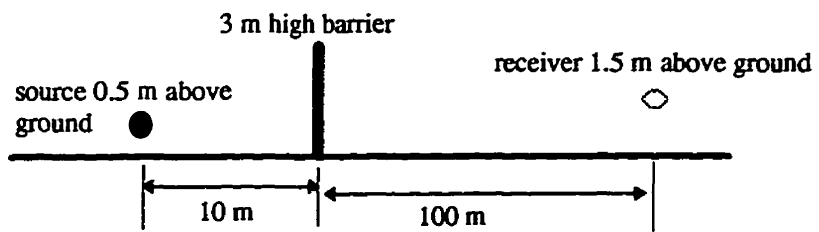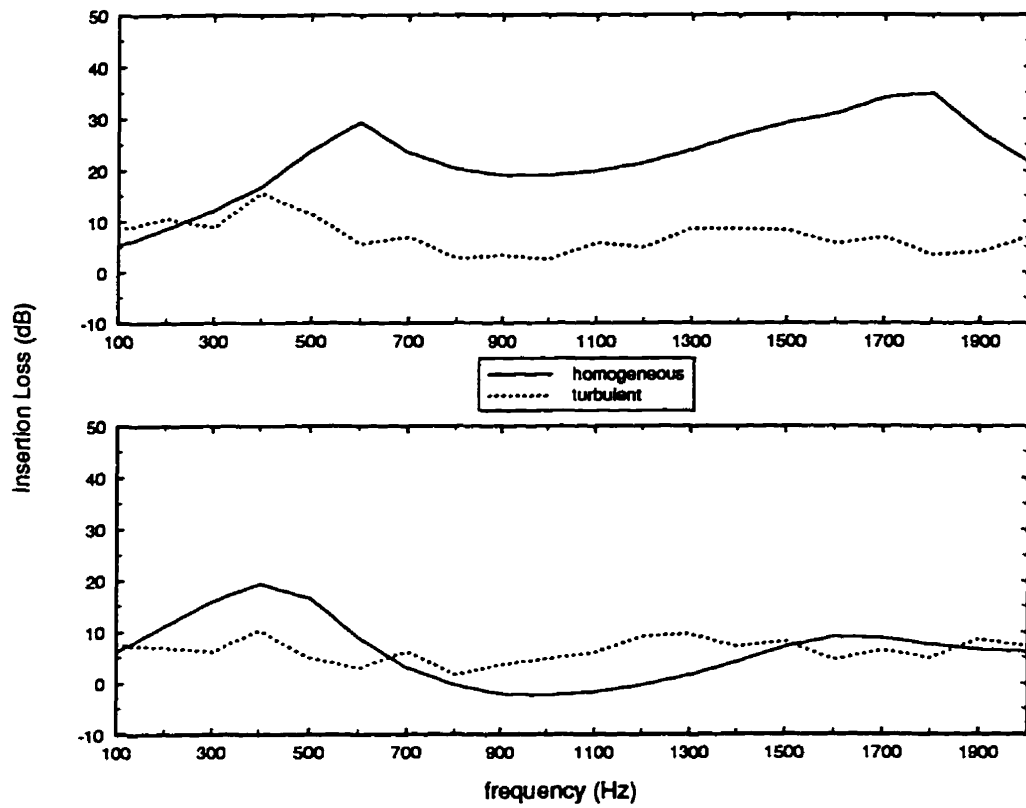
Figure 3.22: Frequency response at receiver 100 m away from barrier.
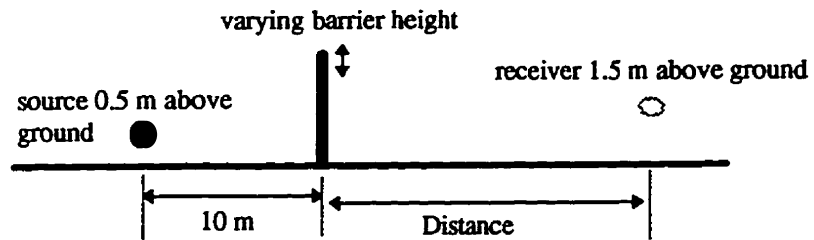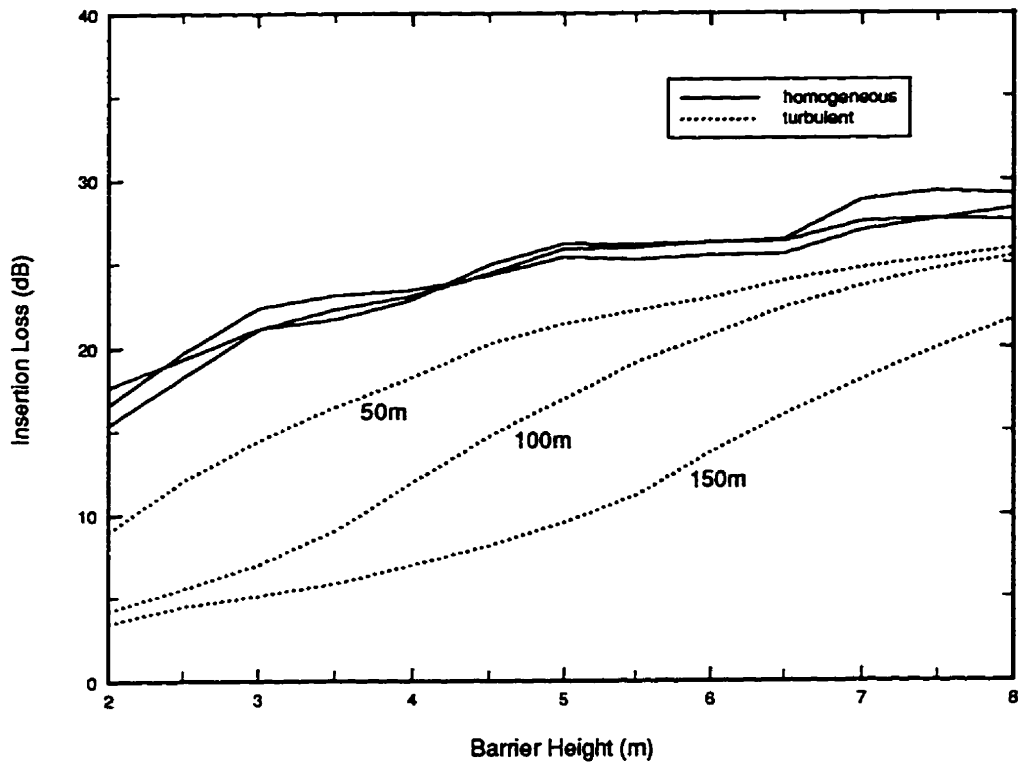
Figure 3.23: Insertion loss as a function of barrier height at 3 receiver locations over rigid ground.

4.9 m high barrier

source 0.7 m above
ground

receiver 1.5 m above ground
○

●

|← 10 m →|← 30 m →|
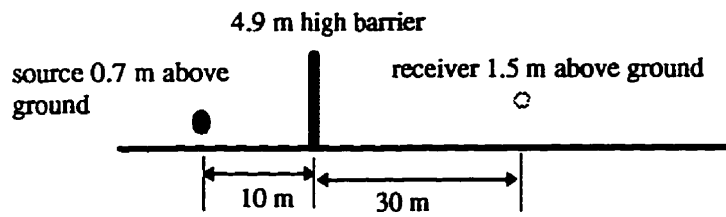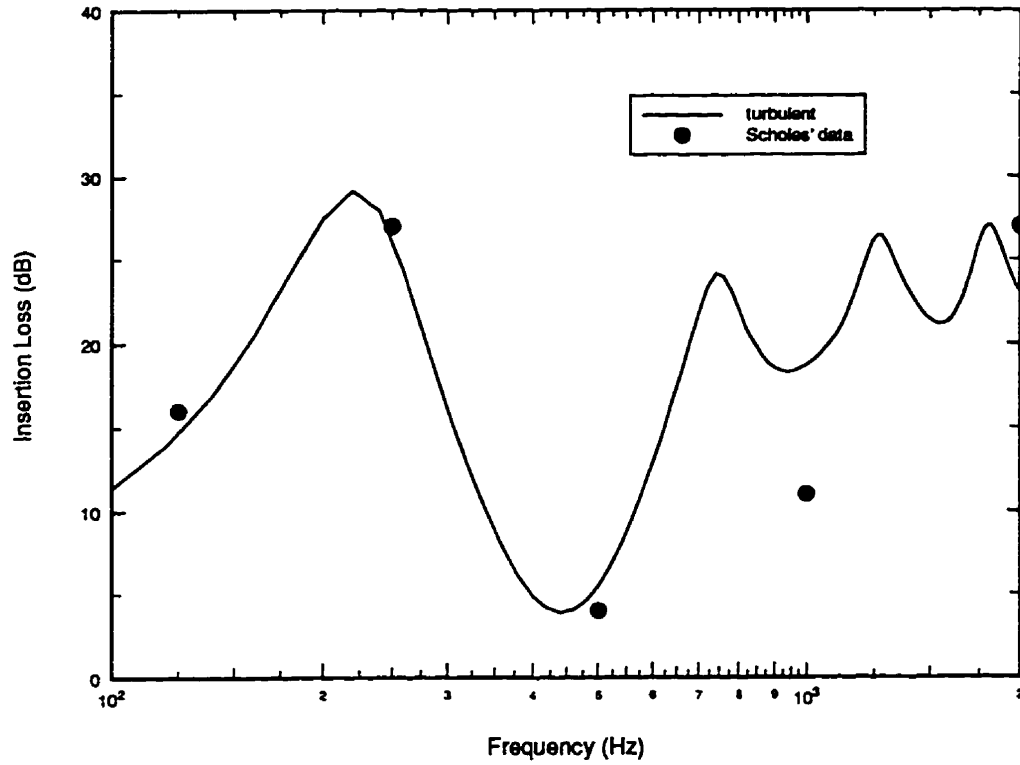
Figure 3.24: Comparisons with experimental data collected by Scholes*et al.*

105

References

3.1 Maekawa, Z., Noise reduction by screens, *Appl. Acoust.*, **1** (1968) 157-173.

3.2 Kurze, U. J. & Anderson, G. S., Sound attenuation by barriers, *Appl. Acoust.*, **4** (1971) 35-53.

3.3 L'Espérance, A., The insertion loss of finite length barriers on the ground. *J. Acoust. Soc. Am.*, **86** (1989) 179-183.

3.4 Kawai, Y. & Terai, T., The application of integral equation methods to the calculation of sound attenuation by barriers. *Appl. Acoust.*, **31** (1990) 101-117.

3.5 Pirinchieva. R., Model study of the sound propagation behind barriers of finite length, *J. Acoust. Soc. Am.*, **87** (1990) 2109-2013.

3.6 Lam, Y. W., Using Maekawa's chart to calculate finite length barrier insertion loss, *Appl. Acoust.*, **42** (1994) 29-40.

3.7 Hothersall, D.C. Chandler-Wilde, S.N. & Hajmirzae, M.N., Efficiency of single noise barriers, *J. Sound Vib.*, **146** (2) (1991) 303-322.

3.8 Fyfe, K.R. & Harrison, C.C., Modeling of road noise and optimal barrier design, *CMHC report #6585/F039* (1995).

3.9 Astley, R. J., Wave envelope and infinite element elements for acoustical radiation, *Int. J. Numerical Methods Fluids.*, **3** (1983) 507-526.

3.10 Cremers, L. & Fyfe, K.R., On the use of variable order infinite wave envelope elements for acoustic radiation and scattering, *J. Acoust. Soc. Am.*, **97** (4) (1995) 2028-2040.

3.11 Muradali, A. & Fyfe, K.R., A Study of 2D and 3D Barrier Insertion Loss Using Improved Diffraction Based Techniques, Accepted for publication in *Applied Acoustics*.

3.12 Lee, S. W., Bong, N., Richards, W. F. & Raspet, R., Impedance formulation of the fast-field program for acoustic wave propagation in the atmosphere, *J. Acoust. Soc. Am.*, **79** (1986) 628-634.

3.13 Raspet, R., Lee, S. W., Kuester, E., Chang, D. C., Richards, W. F., Gilbert, R., and Bong, N., A fast-field program for sound propagation in a layered atmosphere above an impedance ground, *J. Acoust. Soc. Am.*, **77** (1985) 345-352.

3.14 White, M. J. & Gilbert, K. E., Application of the parabolic equation to the outdoor propagation of sound, *Applied Acoustics*, **27** (1989) 227-238.

3.15 West, M., Gilbert, K. & Sack, R. A., A tutorial on the parabolic equation (PE) model used for long range sound propagation in the atmosphere, *Applied Acoustics*, **37** (1992) 31-49.

3.16 Gilbert, K. E. & Di, X., A fast Green's function method for one-way sound propagation in the atmosphere, *J. Acoust. Soc. Am.*, **94** (1993) 2343-2352.

3.17 Gilbert, K. E., Raspet, R., and Di, X., Calculation of turbulence effects in an upward-refracting atmosphere, *J. Acoust. Soc. Am.*, **87** (1990) 2428-2437.

3.18 L'Espérance, A., Herzog, P., Daigle, G. A. & Nicolas, J. R., Heuristic model for outdoor sound propagation based on an extension of the geometrical ray theory in the case of a linear sound speed profile, *Applied Acoustics*, **37** (1992) 111-139.

3.19 Embleton, T. F. W., Thiessen, G. J., & Piercy, J. E., Propagation in an inversion and reflections at the ground, *J. Acoust. Soc. Am.*, **59** (1976) 278-282.

3.20 Scholes, W. E., Salvidge, A. C. & Sargent, J. W., Field performance of a noise barrier, *J. Sound Vib.*, **16** (1971) 627-642.

3.21 DeJong, R. & Stusnick, E., Scale model studies of the effects of wind on acoustic barrier performance, *Noise Control Engng*, May-June (1976) 101-109.

3.22 Daigle, G. A., Diffraction of sound by a noise barrier in the presence of atmospheric turbulence, *J. Acoust. Soc. Am.*, **71** (1982) 847-854.

3.23 Salomons, Erik M., Noise barriers in a refracting atmosphere, *Applied Acoustics*, **47** (1996) 217-238.

3.24 Salomons, Erik M., Diffraction by a screen in down wind sound propagation: A parabolic-equation approach, *J. Acoust. Soc. Am.* **95** (1994) 3109-3117.

3.25 Daigle, G. A., Acoustics of noise control outdoors, *15th International Congress on Acoustics, Trondheim, Norway*, 26-30 June 1995, 49-56.

3.26 Pierce, A. D., Diffraction of Sound around corners and over wide barriers, *J. Acous. Soc. Am.* **55** (1974) 941-955.

3.27 L'Espérance, Gabillet, Y. & Daigle, G. A., Outdoor sound propagation in the presence of atmospheric turbulence: Experiments and theoretical analysis with the fast field program algorithm, *J. Acoust. Soc. Am.*, **98** (1995) 570-579.

3.28 Embleton, T. F. W., Piercy, J. E. & Daigle, G. A., Effective flow resistivity of ground surfaces determined by acoustical measurements, *J. Acoust. Soc. Am.*, **74** (4) 1983 1239-1244.

3.29 Acoustical Society of America, Method for the calculation of the absorption of sound by atmosphere, ANSI S1.26. Acoustical Society of America, New York, 1978.

3.30 Nobile, M. A. & Hayek, S. I., Acoustic propagation over an impedance plane, *J. Acoust. Soc. Am.*, **78** (1985) 1325-1336.

3.31 Stinson, M. R., A note on the use of an approximate formula to predict sound fields above an impedance plane due to a point source, *J. Acoust. Soc. Am.*, **98** (1995) 1810-1812.

CHAPTER 4

CONCLUSIONS AND FUTURE RESEARCH

4.1 Summary and Conclusions

Noise barriers are commonly used to shield residential areas from traffic noise. However, these barriers are costly in nature and, as such, it is critical to understand the underlying parameters that govern their performance.

4.1.1 Barrier Performance Models

There are several techniques in current literature for modeling the performance of noise barriers. These techniques fall into two main classes: (i) diffraction based methods and (ii) wave based methods. Diffraction based methods are based on the geometric theory of diffraction, and are widely used in the engineering community. The more recent wave-based methods such as Boundary Element Methods (BEM) and the Finite Element Methods (FEM), solve the governing wave equation, and thus, model exactly the reflection, diffraction and the phase interferences in the sound field around the barrier. However, the excessive computational requirements associated with these methods make them impractical design tools for modeling typical noise barrier geometries at typical road noise frequencies.

From the diffraction based class of methods, Maekawa's method is the simplest and thus widely used in the engineering community. However, Lam recently improved

on Maekawa's energy summation of the diffraction paths, by taking into account the phase interference between these paths. As a result, better agreements were observed with experimental and wave-based results.

In Chapter 2, Lam's preliminary work was extended to include the diffraction models of Pierce, and Kurze and Anderson, the modeling of two-dimensional geometries, finite ground impedance, and the consideration of parallel barrier geometries. Comparisons with the BEM results showed good agreements for both single and parallel barrier geometries. However, predictions using the diffraction model of Kurze and Anderson fell short in regions close to the diffraction boundary layer, and when parallel barrier geometries were considered in 2D. This was attributed to the fact that the diffraction model diverges as receivers get close to the diffraction boundary layer, and also to the fact that this model only predicts an amplitude change (i.e. phase is assumed to be unaffected) at the diffraction edge. Some other conclusions arrived at in this chapter are as follows:

- Comparisons with FEM showed good agreements for finite impedance considerations in 2D modeling schemes.

- In comparing 2D and 3D geometries, it was found that barriers longer than 300m could be well approximated by a simple 2D model with a line source.

- Large differences were observed between a 2D line source to a 3D incoherent line source.

The major conclusion for this chapter was the advantage of diffraction based techniques over the wave based methods in terms of calculation times. The diffraction based methods took only a fraction of the calculation times and provided wave-based accurate results. This then made it possible to conduct typical barrier tests such as frequency sweeps, octave averaging and varying barrier width tests in reasonable calculations times.

4.1.2 Atmospheric Consideration

A major limitation of the techniques discussed thus far is that a homogeneous atmosphere is assumed, and as such, the predicted barrier insertion losses are different from the actual barrier insertion losses. The atmosphere consists of several inhomogeneities such as wind and temperature gradients, and turbulence, which greatly affect the way sound energy is transmitted.

There are various prediction schemes for modeling the propagation of sound outdoors. Two wave-based formulations are the Fast Field Program (FFP) and the Parabolic Equation (PE). Recently, a heuristic atmospheric model based on geometric ray theory, was developed as an alternative to the wave-solutions due to their excessive calculational times. This model assumes a linearly varying sound speed profile, whereas the wave solutions can account for arbitrary profiles.

These prediction schemes, however, are generally restricted to flat ground propagation and cannot readily account for the screening effects of a barrier. Experimental studies have been done to investigate the effects of atmosphere on barriers, and it was concluded that the barrier effectiveness was reduced when they are downwind from the source. Also, turbulence over the top of barriers scattered sound energy from the source into the shadow regions thereby reducing the barrier's shielding effect.

In Chapter 3, a model was proposed for introducing the atmospheric element into barrier calculations. The heuristic atmospheric model, for the downward refracting profiles, was combined with the diffraction coefficient equations of Pierce. Comparisons with the PE model incorporating a thin screen showed good results.

It was found that calculations made with a single sound speed gradient resulted in wildly varying insertion loss values in the shadow region of the barrier. This does not adequately represent the atmospheric effect on barriers. In turn, an average over a number of sound speed gradient reduced the wild variation of results, and instead showed the expected degradation of noise barriers in the presence of atmospheric inhomogeneities. It was seen that past a certain distance behind a barrier, the insertion

loss decreased considerably. This is attributed to the rays *that walk* over the barrier.

Also preliminary comparisons with experimental data collected by Scholes *et al.* were conducted. However, the experimental conditions were not well documented and guesses had to be made on the ambient temperature and the effective flow resistivity of the ground. In despite of this, good agreements were observed between the proposed model and the experimental data.

4.2 Future Work

The preliminary comparisons with the experimental data shows promise for the combined model for predicting barrier performance in the presence of atmospheric conditions. However, further validations with experimental measurements made under well documented conditions is required. This will help judge the usefulness of the linear sound speed profile, and its averaging, in short and medium range barrier studies. For longer range barrier studies, a more general sound speed profile and a more representative averaging of sound speed profiles for modeling atmospheric conditions will need to be developed.

Other improvements include the modeling of upwind conditions (negative sound speed gradients) and the diffraction of the rays that pass over, but close to, the barrier edge. To make the model more complete, considerations for predictions in the bright zone by modeling sound reflections off the barrier will need to be made.

Appendix A

Geometrical Theory of Diffraction

A.1 Introduction

A principle branch in acoustical theory called *geometrical acoustics* or *ray acoustics*, describes the spreading of sound in terms of rays. The path of a ray is traced out when observing the time travel history of a single point on a wavefront. This theory is very similar to that of *geometrical optics*, the oldest and most widely used theory of light propagation. Geometrical theory explains the behaviour of rays as they reflect off of various surfaces or as they are transmitted through opaque surfaces. However, the behaviour of rays as they hit edges and corners remains unexplained by ordinary geometrical theory [1.35].

As rays come across these edges and corners, new rays called *diffracted rays* are generated [1.35]. Various theories on diffraction have been developed such as those by Fresnel, Kirchhoff and Keller, to name a few. These theories cover diffraction for various conditions such as diffraction through appertures and edges. However, edge diffraction is of more interest for noise barrier applications since most barriers are modelled as thin screens.

To explain the physics behind edge diffraction, the following discussion will focus on Huygens-Fresnel principle leading to Kirchhoff's diffraction theory [1.36]. Kirchhoff's theory explains diffraction in terms of waves. Keller's diffraction theory, on the other hand, describes edge diffraction in terms of rays and associates these dif-

fracted rays with a diffraction coefficient multiplied to the field incident to an edge [1.35]. The notion of a diffraction coefficient played a central role in the formulation of diffraction path equations in Chapters 2 and 3 (Equations 2.1 and 3.1).

A.2 Kirchhoff's Theory of Diffraction

A.2.1 Huygens-Fresnel Principle

According to Huygens' wave construction, every point on a wavefront can be considered the source of secondary spherical wavelets. The envelope of these secondary wavelets then describe a wavefront at a later instant. Fresnel postulated that these secondary wavelets mutually interfere. The combination of the two notions is thus known as *Huygens-Fresnel Principle* [1.36].

A depiction of a wavefront and the secondary wavelets is shown in Figure A.1. The amplitude of the secondary wavelets cannot be uniform in all directions simply because this would produce an equally strong wavefront travelling backwards. The contribution to the light disturbance at some point P from a point Q on a wavefront S, shown in Figure A.2, can be expressed as follows:

$$dU(P) = K(\chi)\frac{Ae^{jkr_o}}{r_o}\frac{e^{jks}}{s}dS \tag{A.1}$$

where $s = QP$ and $K(\chi)$ is referred to as the *inclination factor* describing the variation of secondary wavelet amplitude with the angle χ, often referred to as *the angle of diffraction*.

An expression for the inclination factor was not given by Fresnel, however he assumed that the amplitude of the secondary wavelet was at its maximum in the direction of propagation (i.e. $\chi = 0$) rapidly decreasing to zero in the direction tangential to propagation (i.e. $\chi = \pi/2$). Kirchhoff later proved that this was not true.

A.2.2 Kirchhoff's Diffraction Theory

Upon applying Green's theorem to the Helmholtz equation, Kirchhoff formulated the *integral theorem of Helmholtz and Kirchhoff*. One form of this theorem is

$$U(P) = \frac{1}{4\pi} \int\int_S \left\{ U \frac{\partial}{\partial n} \left(\frac{e^{jks}}{s} \right) - \frac{e^{jks}}{s} \frac{\partial U}{\partial n} \right\} dS \qquad (A.2)$$

where S represents the boundary of the region of integration, and s is the distance between the source and a point (x, y, z) [1.36].

Kirchhoff applied this theorem to the diffraction of light through a small opening in a plane opaque screen, and with some approximations he derived an expression for the inclination factor to be

$$K(\chi) = -\frac{j}{2\lambda}(1 + \cos\chi) \qquad (A.3)$$

This confirms that the amplitude is a maximum in the direction of propagation (i.e. $\chi = 0$). This also shows that Fresnel's assumption that the amplitude is the weakest in the direction tangential to propagation (i.e. $\chi = \pi/2$) is not true, and that the amplitude is the weakest in the opposite direction of propagation (i.e. $\chi = \pi$). Kirchhoff also showed that the interference of wavelets around the envelope was mutually destructive, thus leaving a wave travelling away from the source.

In the event of a wave encountering an edge, the spherical wavelets close to the edge, shown in Figure A.3, spread some of the light into the shadow region. The inclination factor for the amplitude of the spherical wavelet suggests the amount of light that is diffracted into this region. In the region immediately next to the screen, the least amount of light is observed. The brightness gradually increases upon reaching the *line-of-sight* (this corresponds to $\chi = 0$) where the amplitude of the spherical wavelet at the tip of the edge is a maximum.

115

A.3 Keller's Diffraction Theory

Although Kirchhoff's diffraction theory explains the physical aspects behind edge diffraction, Keller's theory explains the behaviour of rays that come into contact with the edge of a semi-infinite screen [1.35]. For a plane wave that is normally incident on a straight edge, the diffracted wave spreads in a cylindrical fashion with the straight edge as its axis. In terms of rays, this suggests that an incident ray normal to a straight edge gives rise to diffracted rays that leave the edge in all directions. Figure A.4 depicts both the wave and ray representations of diffraction.

In geometrical optics, rays that are incident upon a surface and are reflected or transmitted, are multiplied with a reflection or transmission coefficient, respectively. Keller followed this analogy and presumed that diffracted rays are associated with a diffraction coefficient that is multiplied to the incident ray. For a ray normally incident upon an edge shown in Figure A.5, the field for a diffracted ray can be represented by

$$u_e = Du_i r^{-\frac{1}{2}} e^{jkr} \qquad (A.4)$$

where D is the diffraction coefficient, u_i is the incident field at the edge and r is the distance from the edge. In comparing this expression with Sommerfeld's exact solution for diffraction of a planar wave for large values of kr, the diffraction coefficient tends to

$$D = -\frac{e^{j\pi/4}}{2(2\pi k)^{\frac{1}{2}} \sin\beta} \left[\sec\frac{1}{2}(\theta - \alpha) \pm \csc\frac{1}{2}(\theta + \alpha) \right] \qquad (A.5)$$

Here β is the angle between the incident ray and the edge, which for this case is $\pi/2$ since the ray is normally incident to the edge.

A.4 Diffraction Modeling in 2D and 3D

The notion of a diffraction coefficient by Keller played a central role in formulating the diffraction equations in Chapters 2 and 3. For this thesis, diffraction coefficients were determined using the semi-empirical models of Maekawa [1.4], and Kurtz and

116

Anderson [1.5], and the approximate solution to the wave equation for wedge diffraction proposed by Pierce [1.10]. These models are proposed for both 2 and 3 dimensional considerations, with the exception of Maekawa which was only applied to 3D geometries.

For 2D applications, the incident field is that produced by a cylindrical source and the diffracted field spreads in a cylindrical fashion with the edge as its axis. This is an extension to the case for a plane wave incident upon a straight edge in Keller's theory, and can easily be explained with Huygens' wave construction. The sound from a source S on one side of a semi-infinite screen, detected by a receiver R on the other side, travels along the path shown in Figure A.6. In Chapter 2, this path is referred to as the *diffraction path*. The sound pressure at receiver R is then

$$p_R = D H_0^{(1)}(kr_1) H_0^{(1)}(kr_2) \tag{A.6}$$

where $H_0^{(1)}(kr)$ is the Hankel function of the first kind of order zero and D is the diffraction coefficient as determined by the diffraction models. This diffraction coefficient is a change in both the amplitude and the phase of the incident ray as it is diffracted towards the receiver R. Thus, Equation A.6 is modified to

$$p_R = A e^{j\zeta} H_0^{(1)}(kd) \tag{A.7}$$

where A is the amplitude change, ζ is the phase shift at diffraction and

$$H_0^{(1)}(kd) = H_0^{(1)}(kr_1) H_0^{(1)}(kr_2)$$
$$d = r_1 + r_2$$

Figure A.7 shows a semi-infinite screen between a spherical point source S and a receiver R. For such 3D applications, the incident field is spherical, however the diffracted field is not obvious. According to Huygens' wave construction, the secondary point sources would exist along the edge. These secondary sources, however do not lie on the same wavefront. In accordance with Huygens-Fresnel principle, contributions from these secondary sources to the receiver R, other than the one at S_E,

are negligible as secondary wavelets interfere destructively in directions other than that of propagation. This is reiterated by Keller's law of edge diffraction (based on Fermat's principle for minimum path travel times), which states that the diffraction path between S and R is the shortest distance that goes from the source to the edge, and then to the receiver [1.35]. Also, the incident and diffracted rays make the same angle γ with the diffracting edge. Similar to Equation A.7, the sound pressure at the receiver R for 3D geometries can be represented by
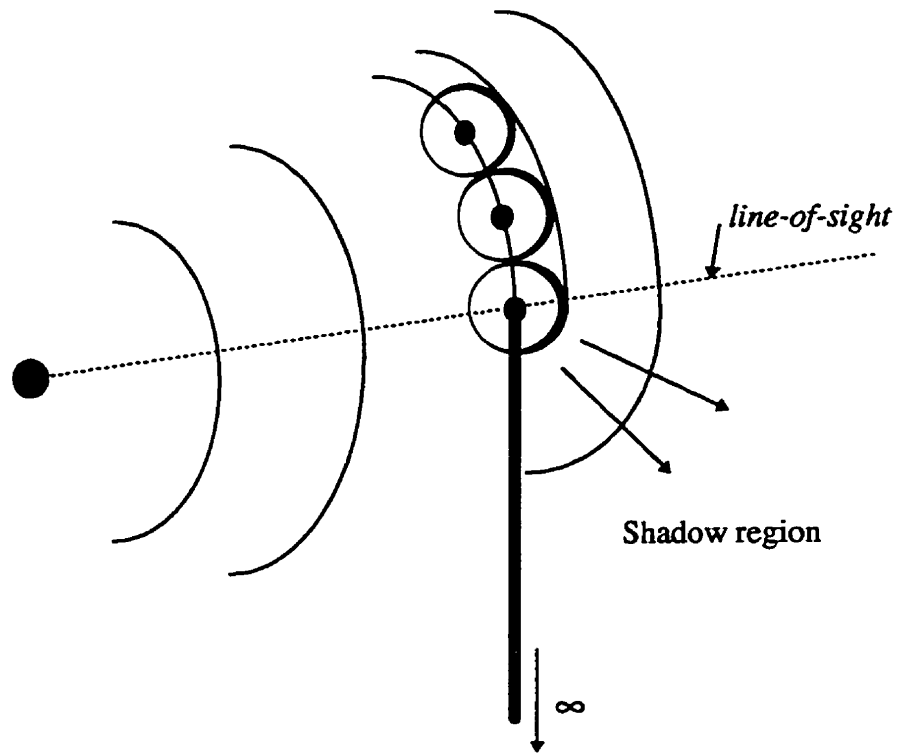
$$p_R = Ae^{j\varsigma}\frac{e^{-jkd}}{d} \tag{A.8}$$
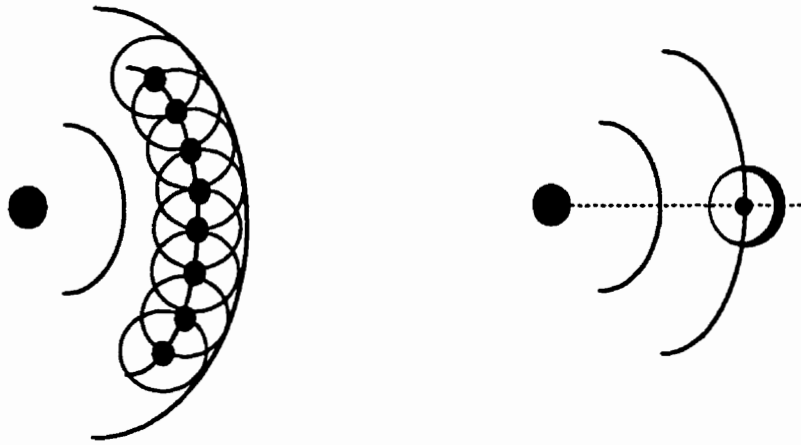
Figure A.1: Sources of secondary disturbances on a wavefront by Huygens' wave construction. The amplitude of the spherical wavelets however cannot be uniform in all directions or an equally strong wave will travel backwards.
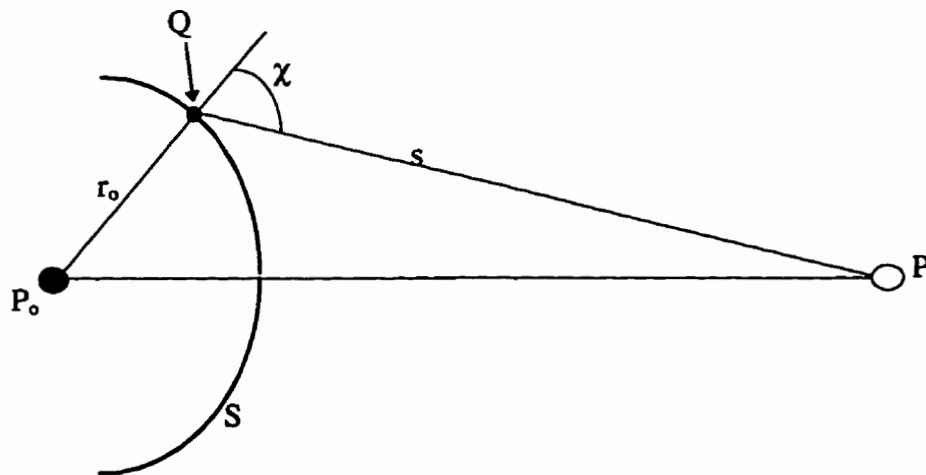
Figure A.2: Derivation of directional variation for a secondary spherical wavelet.

Figure A.3: Light diffracts into the shadow region with the aid of the spherical sources close to the tip of the edge.
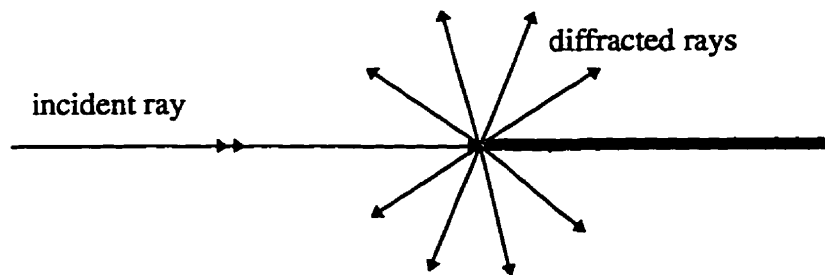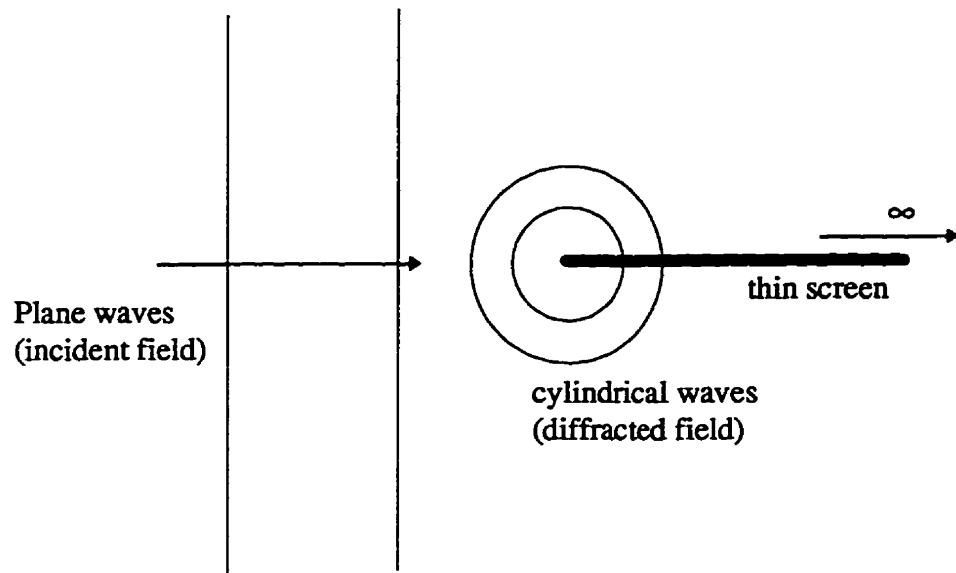
Figure A.4: 2D projection of plane wave diffraction by a thin screen and the associated ray representation.
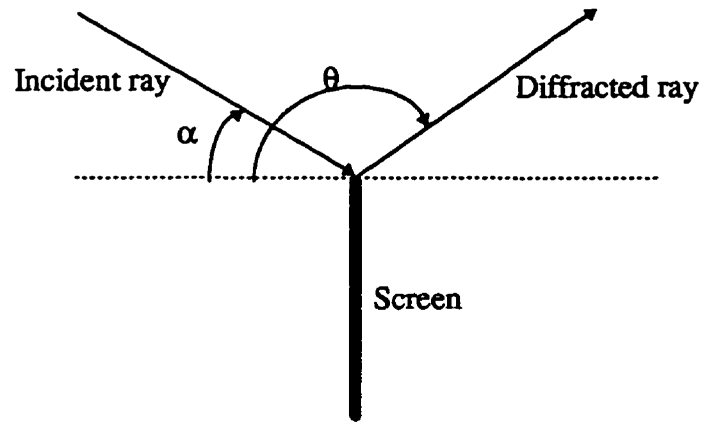
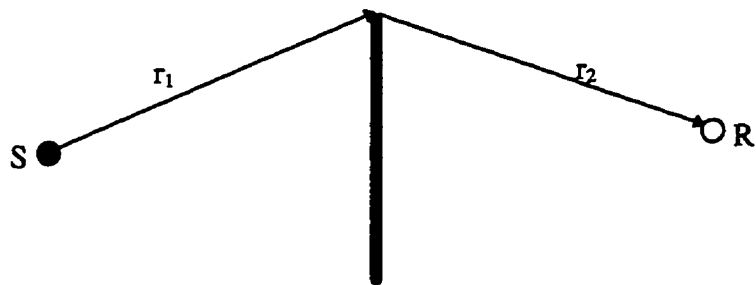Figure A.5: Incident and diffracted rays with the associated angles.

Figure A.6: Diffraction path in 2D.

Arial View

Top View
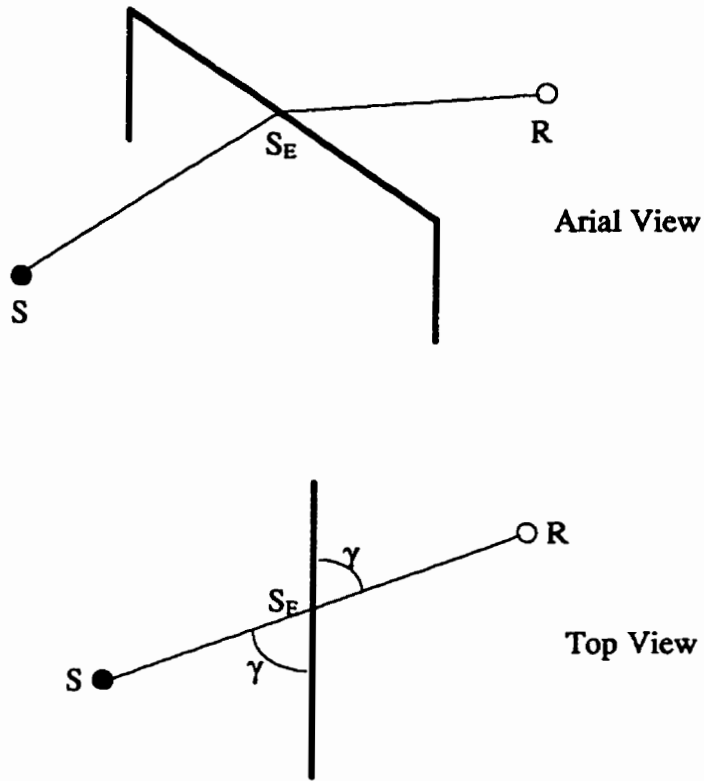
Figure A.7: Diffraction path in 3D.

Appendix B

Atmospheric Absorption

As sound waves pass through the atmosphere, some of the energy is lost to the air due to viscosity effects and thermal diffusion. This is most apparent at large distances, and for high frequencies. The atmospheric absorption coefficient, $A(R)$, from Equation 3.20 is determined as follows:

$$A(R) = 10^{R*AT(f)/2000} \tag{B.1}$$

where R is the distance of propagation, and $AT(f)$ is the atmospheric absorption coefficient, in dB/100m, for frequency f determined using the Standard ANSI S1.26 [3.28].

Appendix C

Spherical Reflection Coefficient

Under homogeneous conditions, there are 2 sound rays between a source and a receiver above ground as depicted in Figure C.1. One ray travels directly from the source to the receiver and the other reflects off of the ground with an angle of incidence ψ_g. The acoustic pressure at the receiver is then the summation of the contributions of both the rays. For 3D geometries we obtain,

$$p_r = \frac{\exp(jkR_1)}{R_1} + Q\frac{\exp(jkR_2)}{R_2} \tag{C.1}$$

where k, R_1 and R_2 are the wave number and the path lengths of the direct and the reflected sound rays.

The spherical reflection coefficient Q for the ground of finite impedance Z_g is determined as follows [3.30,3.31]:

$$Q = R_p + (1 - R_p)F(w) \tag{C.2}$$

$$R_p = \frac{\sin\psi_g - 1/Z_g}{\sin\psi_g + 1/Z_g} \tag{C.3}$$

$$F(w) = 1 + j\pi^{1/2}w\exp\left(-w^2\right)\mathrm{erfc}(-jw) \tag{C.4}$$

$$w = \frac{1+j}{2}(kR_2)^{1/2}(\sin\psi_g + 1/Z_g) \tag{C.5}$$

$$Z_g = \left[1 + 9.08\left(\frac{f}{\sigma}\right)^{-0.75} + j11.9\left(\frac{f}{\sigma}\right)^{0.73}\right] \tag{C.6}$$

where σ is the effective flow resistivity.

Under a strong positive gradient, any single ray between the source and receiver may undergo multiple reflections on the ground as shown in Figure C.2. The effective spherical reflection coefficient is then

$$Q_{eff} = Q^n \qquad \text{(C.7)}$$

where Q is the spherical reflection for the angle of incidence ψ_g, and n is the number of reflections on the ground for the respective ray.
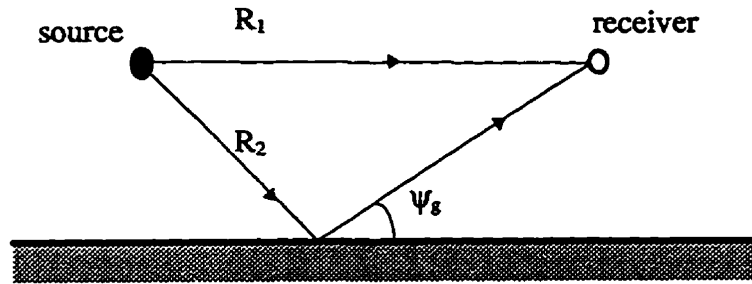
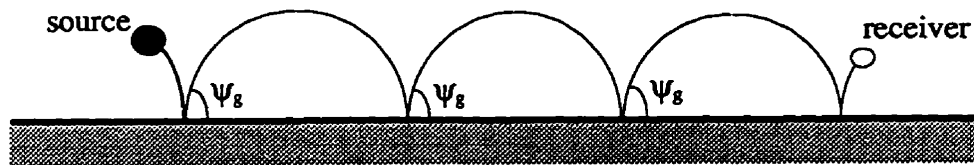**Figure C.1:** Sound rays between a source and receiver above ground under homogeneous conditions.

Figure C.2: Multiple ground reflections for any sound ray under strong positive gradients.

APPENDIX D

THE FAST FIELD PROGRAM (FFP) AND THE PARABOLIC EQUATION (PE)

D.1 Introduction

The FFP and the PE models begin with the classical wave equation for the acoustic pressure:

$$\left(\nabla^2 - \frac{1}{c^2(z)}\frac{\partial^2}{\partial t^2}\right)p(r,z,t) = -4\pi\delta(x,y,z-z_s,t) \tag{D.1}$$

where $c(z)$ is the sound speed as a function of height z, δ represents a delta function source of unit strength located at height z_s.

Assuming simple harmonic time dependance $\exp(-i\omega t)$, the above equation becomes the Helmholtz equation,

$$\left(\nabla^2 + k(z)^2\right)p(r,z) = -4\pi\delta(r,z-z_s) \tag{D.2}$$

where $k = \omega/c(z)$ is the wave number. Writing this equation in cylindrical coordinates and assuming no variation with θ, the Helmholtz equation becomes

$$\frac{\partial^2 p}{\partial r^2} + \frac{1}{r}\frac{\partial p}{\partial r} + \frac{\partial^2 p}{\partial z^2} + k^2 p = -\frac{2}{r}\delta(r)\delta(z-z_s) \tag{D.3}$$

where the source is assumed to be at $r = 0$.

Reflection from a porous ground can be described by the boundary condition

$$\left[\frac{\partial^2 p}{\partial z^2} + ik\beta p\right]_{z=0} = 0 \tag{D.4}$$

where β is the normalized surface admittance.

From this point, both the FFP and PE models differ. The following sections describe each in more detail.

D.2 FFP models

FFP models were originally developed for underwater sound propagation predictions and have since been adapted to model sound propagation through the atmosphere.

D.2.1 Basic formulation

By taking the Hankel transform of Equation D.3, the r dependance can be dropped. The zero order Hankel transform of p is

$$p(r, z) = \int_0^\infty P(K, z) J_0(Kr) K dK \qquad (D.5)$$

where K is the horizontal component of the wave number, J_0 is the Bessel function and $P(K, z)$ satisfies

$$\frac{d^2 P(K, z)}{dz^2} + [k^2(z) - K^2] P(K, z) = -\delta(z - z_s) \qquad (D.6)$$

FFP models perform a direct numerical integration on Equation D.5.

D.2.2 Implementations

With the notion of axial symmetry about the source, FFP models assume the atmosphere is a layered medium in the xz plane with source and receiver bounded by impedance surfaces. This is depicted in Figure D.1. Each layer is associated with a single value for the sound speed and the sound speed value can vary from layer to layer.

FFP models are restricted to flat ground propagation and cannot readily account for the scattering effects of a barrier. Therefore they were not used in the preparation of this thesis. For further details on FFP models, refer to [3.12, 3.13].

D.3 PE models

PE models have been used for various wave propagation problems. Some areas include optics, electromagnetics, underwater acoustics, and more recently, atmospheric sound propagion. The models assume that sound is always directed away from the source and very little backscattering occurs. The main advantange from making this assumption is that a boundary value problem is reduced to an *initial* boundary value problem, permitting much simpler solutions of the resulting differential equation.

D.3.1 Basic formulation

By making a change of variables $U = pr^{1/2}$ and a far-field assumption ($kr >> 1$), Equation D.3 becomes

$$\frac{\partial^2 U}{\partial r^2} + \frac{\partial^2 U}{\partial z^2} + k^2 U = 0 \tag{D.7}$$

By denoting Q as the operator such that

$$Q = \frac{\partial^2}{\partial z^2} + k^2 \tag{D.8}$$

then Equation D.6 can be written as

$$\left(\frac{\partial}{\partial r} + i\sqrt{Q}\right)\left(\frac{\partial}{\partial r} - i\sqrt{Q}\right) U = 0 \tag{D.9}$$

This represents the incoming waves and the outgoing waves. If only the outgoing waves are considered, Equation D.8 reduces down to

$$\frac{\partial U}{\partial r} = i\sqrt{Q}U \tag{D.10}$$

This equation is solved numerically by implicit stepping on a 2D grid in the xz plane. The resulting equation is as follows:

$$M_2\phi(x + \Delta x) = M_1\phi(x) \tag{D.11}$$

where M_1 and M_2 are tridiagonal matrices. The vectors $\phi(x)$ and $\phi(x+\Delta x)$ represent neighboring grid arrays. These vectors are proportional to the sound pressure p as

follows:

$$\phi(x, z) = p(x, z) \exp(-ik_0 x) \sqrt{x} \qquad (D.12)$$

where k_0 is the wave number at $z = 0$. Note that $k(z) = 2\pi f / c(z)$. A more detailed description of the variables is provided in [3.15, 3.23].

D.3.2 Implementation

The 2D acoustic field through which the PE steps is shown in Figure D.2. The medium is bound by surfaces of finite impedance as in FFP implementations. Ground impedance is enforced on the bottom surface, whereas ρc boundary condition is enforced on the top surface to minimize the reflection of sound energy back into the field. However, this boundary condition absorbs completely only plane waves with normal incidence to the surface. Therefore, an absorbing layer is added directly below the top surface to dampen sound waves. This layer, shown in Figure D.2, is added by introducing an imaginary term $iA[(z - z_m)/(z_M - z_m)]^2$ to the wave number. A is a constant, and z_m is the height of the bottom of the absorbing layer as shown in Figure D.2. The boundary conditions, and the absorbing layer are all accounted for in the formulation of matrices M_1 and M_2.

A tutorial on use of the PE model provides guidelines for variables pertaining to the absorbing layer and hieght of the acoustic medium [3.15]. However, these parameters vary for the frequency of analysis. It was found to be time consuming to obtain these parameters for the consideration of a positive linear sound speed profile and large propagation ranges (up to 500 m) for various frequencies as this involved a trial and error proceedure. Therefore, the same parameters were used for analysis frequencies of 100 an 1000 Hz as those determined by Salomons [3.24]. The only difference was the specification of a linear sound speed profile instead of a logarithmic sound speed profile. Convergence tests were conducted to confirm the validity of these parameters.

The parameters used for analysis frequency of 1000 Hz were: $\Delta x = \Delta z = 0.05$ m,

$M = 8000$, $m = 7700$, and $A = 1$. Similarly, for the analysis frequency of 100 Hz the following parameters were used: $\Delta x = \Delta z = 0.04$ m, $M = 2000$, $m = 1600$, and $A = 0.3$.
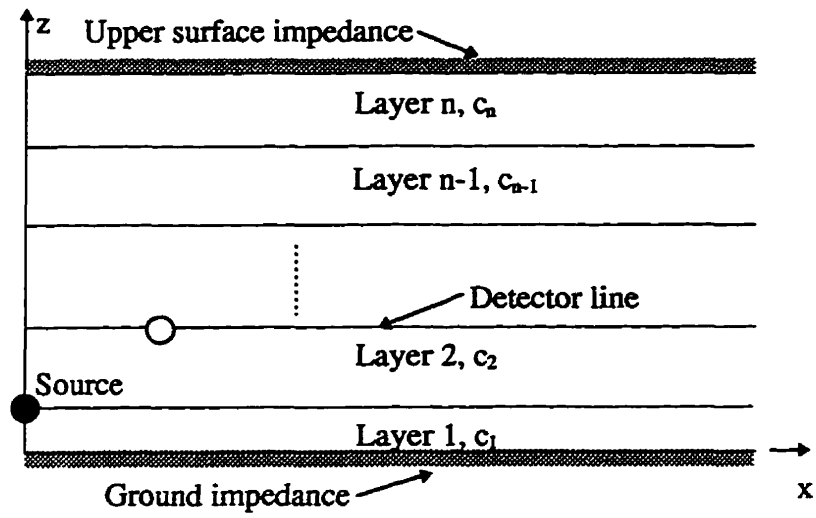
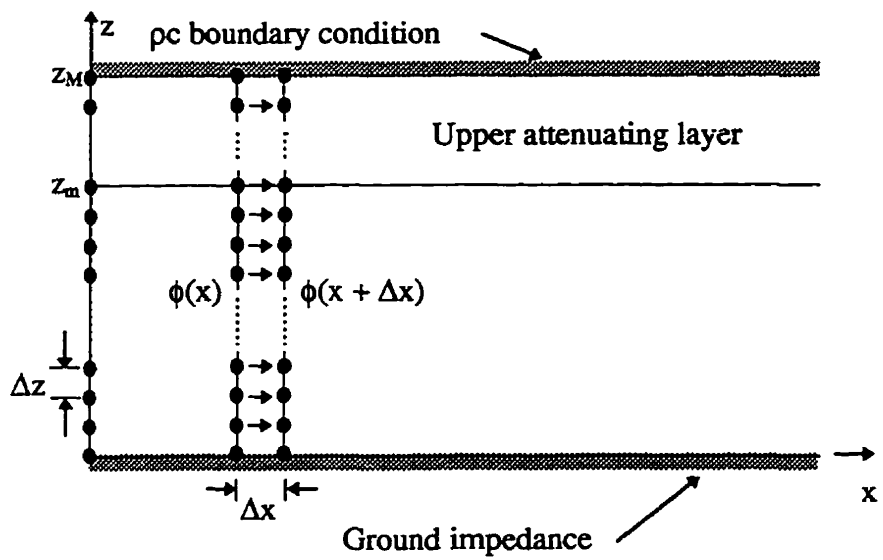**Figure D.1:** Layered atmosphere for FFP implementations.

Figure D.2: Field for PE implementations.